

UNIVERSIDAD AUTÓNOMA DE NUEVO LEÓN
FACULTAD DE INGENIERÍA MECÁNICA Y ELÉCTRICA
SUBDIRECCIÓN DE ESTUDIOS DE POSGRADO



**NUMERICAL SIMULATION OF SELECTIVE LASER MELTING
PROCESS OF METALLIC MATERIALS**

POR:

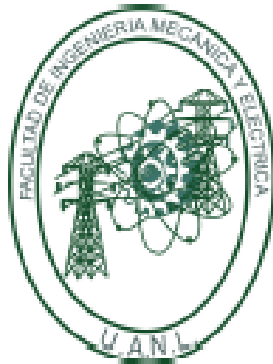
RIGOBERTO GUZMÁN NOGALES

COMO REQUISITO PARCIAL PARA OBTENER EL GRADO DE

DOCTORADO EN CIENCIAS DE LA INGENIERÍA AERONÁUTICA

MARZO 2022

UNIVERSIDAD AUTÓNOMA DE NUEVO LEÓN
FACULTAD DE INGENIERÍA MECÁNICA Y ELÉCTRICA
SUBDIRECCIÓN DE ESTUDIOS DE POSGRADO



**NUMERICAL SIMULATION OF SELECTIVE LASER MELTING
PROCESS OF METALLIC MATERIALS**

POR:

RIGOBERTO GUZMÁN NOGALES

COMO REQUISITO PARCIAL PARA OBTENER EL GRADO DE

DOCTORADO EN CIENCIAS DE LA INGENIERÍA AERONÁUTICA

MARZO 2022

UNIVERSIDAD AUTÓNOMA DE NUEVO LEÓN
Facultad de Ingeniería Mecánica y Eléctrica
Posgrado

Los miembros del Comité de Evaluación de Tesis recomendamos que la Tesis “Numerical simulation of selective laser melting process of metallic materials”, realizada por el estudiante Rigoberto Guzmán Nogales, con número de matrícula 1887266, sea aceptada para su defensa como requisito parcial para obtener el grado de Doctor en Ciencias de la Ingeniería Aeronáutica.

El Comité de Evaluación de Tesis

Dra. Patricia del Carmen Zambrano Robledo
Director

Dr. Luis Arturo Reyes Osorio
Revisor

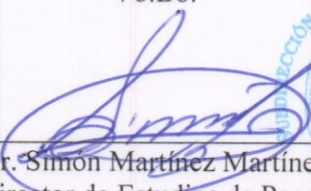
Dra. Guadalupe Maribel Hernández Muñoz
Revisor

Dr. Alex Elías Zúñiga
Revisor

Dr. Omar Eduardo López Botello
Revisor

Dr. Carlos Garza Rodríguez
Revisor

Vo.Bo.


Dr. Simón Martínez Martínez
Subdirector de Estudios de Posgrado



Institución 190001

Programa 557603

Acta Núm. 305

Ciudad Universitaria, a 17 de marzo de 2022.

Abstract

Selective laser melting (SLM) is an important additive manufacturing (AM) process that has the ability of producing high geometric complexity parts (e.g. aerospace components, such as gas turbine blades, brackets, fuel nozzle, to name a few) directly from 3D virtual models. This technology is attracting great attention in the aerospace, automotive, and energy industries since it opens the door to completely new possibilities for design. However, SLM is complex due to heat and mass transfer inside of it where its melt pool geometry represents a significant effect on the precision and cost-effectiveness of the SLM process. Therefore, one of the best techniques to investigate on SLM process is simulation as well as the measurement of final properties of SLM products.

The present research focuses on developing a numerical model that predicts the temperature evolution of metallic materials subjected to SLM. This model is based on the lattice Boltzmann method (LBM) which solves the transport equations (heat) in only two steps; collision and streaming. The SLM processing parameters, such as laser power, spot irradiation time, and laser absorptivity are considered within the model, as well as constant material properties of the medium. The results obtained by LBM are compared with conventional methods. In order to get an idea about the real melt pool dimensions produced by the laser, experimental data were also considered. For future investigations, a module of this nature can be expanded to predict the optimal processing parameters for a component manufactured via SLM. In addition, the model is expected to work like a processing parameters optimization tool capable to reduce energy consumption, production cost, and processing time, as well as potentialize the SLM material properties (melt pool geometry). On the other hand, knowing that it is of great importance to understand the relationship between the surface features and electrochemical properties of SLMed parts, it was carried out the measurement of corrosion resistance of the SLM 316L SS using linear polarization resistance (LPR) and electrochemical noise (EN) techniques, considering the horizontal (XY) and vertical (XZ) planes of the SLM samples. The corrosion products developed in three different environments were studied using optical (OM) and scanning electron microscopy (SEM).

To emphasize the numerical and experimental results of this investigation, the LBM simulation of SLM AlSi10Mg computes a melt pool width and depth of 8.4×10^{-5} m and 1.8×10^{-5} m, respectively, while for the experimental data, these ones are in 19.21×10^{-5} m and $6.89 \times$

10^{-5} m, respectively. As for the LBM simulation of SLM 316L SS, this one calculates a width and depth of 1.1×10^{-4} m and 4.8×10^{-5} m, respectively, while the experimental values are 1.25×10^{-4} m and 8.51×10^{-5} m, respectively. The LBM simulation results are in good agreement with those obtained by continuum methods.

The corrosion results indicated that the highest corrosion rate was identified in the 20% H_2SO_4 solution in the XZ plane with 2.4×10^{-2} mm/year and the XY plane with 1.31×10^{-3} mm/year. As for the corrosion type, localized corrosion was observed in the 3.5 wt. % NaCl electrolyte, for the XY and XZ planes (-1.65 and -0.012 skewness, respectively), attacking mainly the subgrains of the microstructure and, in some cases, the pores, caused by Cl ions. Uniform corrosion mechanism was presented in the H_2O and H_2SO_4 solutions, for the two observed orientations. The morphology identified by SEM was correlated with the results obtained from the electrochemical techniques.

A mi familia

Acknowledgements

To the Universidad Autónoma de Nuevo León (UANL), Facultad de Ingeniería Mecánica y Eléctrica (FIME), Centro de Investigación e Innovación en Ingeniería Aeronáutica (CIIA), for giving me the opportunity to be part of a great academic community together with its renowned professors.

To the Fondo Institucional de Fomento Regional para al Desarrollo Científico, Tecnológico y de Innovación (FORDECyT) de CONACYT with the titled project Fortalecimiento de la Aeronáutica en el Noreste de México for the offered funding during the development of this research work.

To the Laboratorio Nacional de Manufactura Aditiva y Digital (MADIT), for its great supporting of infrastructure, materials, and technical instructions. A high-technology laboratory for this kind of project.

My greatest thanks to my thesis director, Dra. Patricia del Carmen Zambrano Robledo, who opened me the opportunity to work with an incredible research group. Thanks to her great knowledge, patient, and leadership, Dra. Paty always thrusts us to grow up professionally.

Thanks also to Dr. Omar López, Dr. Luis Reyes, Dra. Guadalupe Maribel, Dr. Francisco Estupiñán, Dra. Citlalli Gaona, and Dra. Barbara Bermúdez for giving me a little of their great knowledge and advices during the obstacles of this project.

Also, I want to extend my gratitude to Dr. Alex Elías Zúñiga, Dr. Luis Palacios, Dr. Daniel Olvera, Dr. Oscar, who believed on me when sometimes I did not believe on myself. They always wish that their students achieve the success; professional and personal.

To the best friends I met during the time of this research work, Luz Aguilar, Claudia Ramon, Viridiana Lince, Catalina Jaramillo, Marilu Orozco, Saul Rubio, Santiago Puma and Xavier Sánchez, who gave me company and support for the stress moments.

Symbols and abbreviations

SLM	Selective laser melting
AM	Additive manufacturing
LBM	Lattice Boltzmann method
LPR	Linear polarization resistance
EN	Electrochemical noise
OM	Optical microscopy
SEM	Scanning electron microscopy
H ₂ SO ₄	Sulfuric acid
NaCl	Sodium chloride
H ₂ O	Water
D2Q9	Standard lattice structure of two dimensions and nine velocities
D2Q4	Standard lattice structure of two dimensions and four velocities
FDM	Finite difference method
FEM	Finite element method
FVM	Finite volume method
CAD	Computer aided design
STL	STereoLithography
FAA	Federal aviation administration
<i>E</i>	Laser energy density
<i>P</i>	Laser power
<i>v</i>	Scanning speed
<i>HS</i>	Hatch spacing
<i>t</i>	Powder layer thickness
<i>t</i>	Time
IN738LC	Inconel alloy 738 LC
IN625	Inconel alloy 625
DOE	Design of experiments
Al	Aluminum
Si	Silicon
Mg	Magnesium
AlSi10Mg	Aluminum Silicon 10 Magnesium Alloy

AA-2024	Aluminum Alloy 2024
AA-357	Aluminum Alloy 357
AA-6061	Aluminum Alloy 6061
Ti	Titanium
V	Vanadium
CA	Cellular automata
FE	Finite element
CA-FE	Cellular automata – Finite element
CET	Columnar to equiaxed transition
LB	Lattice Boltzmann
CA-LB	Cellular Automata – Lattice Boltzmann
IN718	Inconel alloy 718
HF-LBM	Height function lattice Boltzmann method
ρ	Density
C_p	Specific heat capacity
ΔT	Temperature
k	Thermal conductivity
E_L	Line energy input
316L SS	316L stainless steel alloy
EDS	Energy dispersive spectroscopy
XRF	x-ray fluorescence spectroscopy
Cu	Copper
Fe	Iron
Mn	Manganese
N	Nitrogen
Ni	Nickel
O	Oxygen
Pb	Lead
Zn	Zinc
T_a	Ambient temperature
D	Laser diameter
HNO ₃	Nitric acid
HCl	Hydrochloric acid
HF	Hydrofluoric acid

HBF_4	Fluoboric acid
C	Carbon
Cr	Chromium
Mo	Molybdenum
P	Phosphorus
S	Sulfur
$k_{xx}, k_{yy},$ k_{zz}	Thermal conductivities
$x, y,$ and z	Spatial coordinates
$\ddot{\phi}$	Heat source
A	Absorptivity
r	Laser radius
T_0	Initial temperature
T_{wall}	Constant temperature
f_k	Particle distribution function in the direction k
f_k^{eq}	Equilibrium particle distribution function in the direction k
c_i	Microscopic velocity in the direction i
τ	Relaxation time
ω	Collision frequency
α	Thermal diffusivity in LBM
c_s	Sound speed in LBM space-time
F_o	Fourier number
α_P	Thermal diffusivity of the real medium
t_{LBM}	Time steps in LBM
N	Mesh size in LBM
L	Domain length
w_k	Weighting factor in the direction k
h	Convective heat transfer coefficient
V_0	Volume of the grid
q''	Input heat flux
A	Normal area to the corresponding distribution function
T_S	Solidus temperature
T_L	Liquidus temperature

H	Domain height
SIT	Spot irradiation time
MPW	Melt pool width
MPD	Melt pool depth

Table of Contents

Abstract	i
Acknowledgements	iv
Symbols and abbreviations.....	v
Table of Contents	ix
List of Figures	xiii
List of Tables.....	xvii
1 Introduction.....	1
1.1 Statement of the problem	1
1.2 Justification	1
1.3 Novelty statement.....	1
1.4 Hypothesis.....	2
1.5 Objectives of the research	2
1.6 Methodology	2
2 Literature review	4
2.1 Selective Laser Melting (SLM) process.....	4
2.2 Physics of SLM.....	6
2.3 Aeronautical alloys used for SLM process.....	8
2.4 Numerical models for SLM process.....	9
2.5 Dimensionless approaches for studying SLM.....	14
2.6 Summary	16
3 Experimental Methodology.....	17
3.1 Materials and Methods.....	17
3.2 AlSi10Mg samples fabricated by SLM.....	18
3.3 Experimental melt pool morphology of SLM AlSi10Mg alloy	20

3.4	316L SS samples fabricated by SLM.....	22
3.5	Experimental melt pool morphology of SLM 316L SS alloy	24
3.6	Summary	25
4	Numerical Model Development	26
4.1	Thermal history modelling for SLM	26
4.2	Lattice Boltzmann method for SLM process	28
4.3	The D2Q9 lattice structure	29
4.4	Solution procedure	31
4.5	Boundary Conditions in the LBM for the SLM process	33
4.5.1	Dirichlet boundary condition.....	33
4.5.2	Convective boundary condition.....	35
4.5.3	Heat flux boundary condition.....	37
4.6	Material properties and LBM parameters for the simulations.....	38
4.7	Comparison between LBM and FEM	41
4.8	Summary	42
5	Corrosion resistance measurement of 316L stainless steel manufactured by selective laser melting.....	43
5.1	Corrosion studies on SLM 316L SS.....	43
5.2	Material and experimental methods	45
5.2.1	Material preparation	45
5.2.2	Microscopic observation of the XY and XZ testing surfaces.....	46
5.2.3	Corrosion testing	47
5.3	Summary	48
6	Results and discussion.....	49
6.1	Experimental results of melt pool dimensions for the SLM AISi10Mg alloy.....	49
6.2	Experimental results of melt pool dimensions for the SLM 316L SS alloy.....	50

6.3	Simulation results of the SLM AlSi10Mg alloy.....	50
6.4	Simulation results of the SLM 316L SS alloy.....	53
6.5	Comparison among LBM and conventional methods for the SLM AlSi10Mg	56
6.6	Comparison among LBM and conventional methods for the SLM 316L SS	57
6.7	Advantages of using LBM against continuum methods for the simulation of SLM process 57	
6.8	Chemical microanalysis	58
6.9	Characterization of the microstructure.....	60
6.10	Corrosion results	61
6.10.1	Linear polarization resistance (LPR).....	61
6.10.2	Electrochemical noise (EN).....	63
6.11	Corroded surfaces of the SLMed samples.....	67
6.12	Summary	71
7	Conclusions and future work.....	72
7.1	Conclusion.....	72
7.2	Scientific contribution of this research work	75
7.3	Future work	75
8	References	77
	APPENDIX 1	91
	SLM AlSi10Mg simulation by FDM	91
	SLM AlSi10Mg simulation by LBM	95
	SLM 316L SS simulation by FDM	100
	SLM 316L SS simulation by LBM	104
	APPENDIX 2	110
	SLM simulation by FDM and LBM considering laser movement (based on point distance), layer deposition, recoating time ($5 \times 10 - 3$ s) (convection), and number of spots.	110

APPENDIX 3	115
SLM AlSi10Mg simulation with laser movement and layer deposition by FDM	115
SLM AlSi10Mg simulation with laser movement and layer deposition by LBM	121
APPENDIX 4	132
APPENDIX 5	133
Elapsed time for the SLM AlSi10Mg simulation by FEM	133
Elapsed time for the SLM 316L SS simulation by FEM	135

List of Figures

Fig. 1.1 Methodological scheme of the present investigation.	3
Fig. 2.1 It is shown the general principle of the SLM process, a) the laser scans the cross-sectioned of the CAD model, b) SLM component inside the powder bed after scanning all the layers, and c) SLM component obtained after removing the no melted powder.	5
Fig. 2.2 Success cases of AM components, a) CFM International’s 3D-printed fuel nozzle, b) housing for the sensor T25 (one of the first 3D-printed engine components approved by FAA ready to fly inside commercial jet engines such as GE9X and Boeing 777s), c) Titanium Aluminide Low-Pressure Turbine blade, and d) Airbus’s A350 bracket [8].	5
Fig. 2.3 2D schematic representation to show the macrostructure and main processing parameters such as laser power, scanning speed, hatch spacing, and layer thickness of the SLM process.	7
Fig. 2.4 2D Pore morphologies obtained by LOM after SLM processing with different energy densities [16].	7
Fig. 2.5 Inconel superalloy application in gas turbine applications [19].	8
Fig. 2.6 Melt pool measurement undertaken to a) experimental sample 1, b) FEM model for sample number 1 [2].	10
Fig. 2.7 The cross-section morphology of 3# sample molten pool experimental model (a) and numerical model (b) [13].	11
Fig. 2.8 Temperature distribution during SLM process at $P = 250\text{ W}$ and $v = 250\text{ mms}$: (a) on the top surface of the molten pool and (b) on the cross-section of the molten pool as the laser beam reached the center of the first layer; (c) on the top surface of the molten pool and (d) on the cross-section of the molten pool as the laser beam reached the center of the second layer [35].	11
Fig. 2.9 CALB model initial set-up with an equiaxed base plate, powder bed and an electron beam heat source. The color bar maps the grain misorientation with respect to the build direction (y-axis) [32].	12
Fig. 2.10 Beam absorption. Left: absorption of the beam into the powder layer and melt pool that develops. Right: absorption of the beam within a powder particle. The numerical grid is schematically shown [5].	13
Fig. 2.11 Molten pool morphology under the influence of gravity (a) and surface tension (b) [36].	13

Fig. 3.1 SLM 280 HL machine to build metallic sample (AlSi10Mg and 316L SS) for this investigation.	17
Fig. 3.2 SEM image of the AlSi10Mg metal powder taken by the present investigation showing the size of some particles (left side) and an EDS analysis in one of those particles (right side).	18
Fig. 3.3 SLM AlSi10Mg parts.....	20
Fig. 3.4 Cutting plane showing how the SLM AlSi10Mg samples were cut.	20
Fig. 3.5 Optical micrograph showing the SLM AlSi10Mg microstructure, parallel to the build direction. The growth direction is designated with the white arrow while the fusion line is shown with the open arrow.....	21
Fig. 3.6 SEM image of the 316L SS metal powder obtained by this research work showing the size of some powder particles (left side) and an EDS analysis in one of those particles (right side).....	22
Fig. 3.7 SLM 316L SS parts and b) cutting plane used as reference to obtain the cross-section of the sample.	24
Fig. 3.8 Optical micrograph showing the SLM 316L SS microstructure, parallel to the build direction. The growth direction is designated with the white arrow while the fusion line is shown with the open arrow.....	25
Fig. 4.1 Representation of the SLM domain to research on SLM process.....	27
Fig. 4.2 D2Q9 lattice structure used to discretize the solution domain.....	30
Fig. 4.3 D2Q9 lattice structure with the numbering of links for the simulation process [48].....	32
Fig. 4.4 BC for the left side of constant temperature.	34
Fig. 4.5 BC within the convective contact zone.....	36
Fig. 4.6 BC within the laser contact zone.....	38
Fig. 5.1 Metallographic images of the SLMed 316L SS horizontal and vertical surfaces showing a little level of porosity. Image, 3a (50x) and 3b (500x) XY plane and 3c (50x) and 3d (500x) XZ plane.	47
Fig. 5.2 Experimental setup used to perform the corrosion tests; left side, horizontal and vertical cross-section (Z axis is parallel to the build direction) of the work electrodes.....	47
Fig. 6.1 Melt pool dimensions of the SLM AlSi10Mg alloy.	49
Fig. 6.2 Melt pool dimensions of the SLM 316L SS alloy.	50

Fig. 6.3 Simulation results by a) FDM, b) LBM D2Q4, and c) LBM D2Q9 methods of the SLM AlSi10Mg alloy at 100 W laser power and 1×10^{-4} s spot irradiation time..... 51

Fig. 6.4 Melt pool with its corresponding dimensions (width and depth) simulated by FDM, a) and b), LBM D2Q4, c) and d), and LBM D2Q9, e) and d), of the SLM AlSi10Mg alloy. 52

Fig. 6.5 Simulation results by a) FDM, b) LBM D2Q4, and c) LBM D2Q9 of the SLM 316L SS alloy at a 400 W laser power and 8×10^{-5} s spot irradiation time..... 54

Fig. 6.6 Melt pool with its corresponding dimensions (width and depth) simulated by FDM, a) and b), LBM D2Q4, c) and d), and LBM D2Q9, e) and d) of the SLM 316L SS alloy. 55

Fig. 6.7 Temperature values at the position $x_L = 0.5$ in the simulation domain for the SLM AlSi10Mg alloy simulated by LBM and conventional methods. 56

Fig. 6.8 Temperature values at the position $x_L = 0.5$ in the simulation domain for the SLM 316L SS alloy simulated by LBM and conventional methods. 57

Fig. 6.9 SEM images of the polished surfaces of the samples displaying some SLM defects in the material (left-hand side) and chemical composition obtained by EDS of those irregularities (right-hand side). 59

Fig. 6.10 a) SLM inclusion found on the polished surface and b) its EDS chemical composition showing high contents of O, Al, Si, and Mn. 60

Fig. 6.11 Representative optical micrograph showing the SLMed 316L SS microstructure of the horizontal a) and vertical b) surfaces. Growth direction is indicated with a white arrow while the fusion line is shown with an open arrow. 61

Fig. 6.12 Time series in potential and current of the SLMed 316L SS in 3.5 wt. % NaCl, a) potential versus time and b) current versus time. 64

Fig. 6.13 Time series in potential and current for the SLMed 316L SS in 20% H₂SO₄, a) potential versus time and b) current versus time. 65

Fig. 6.14 Times series in potential and current for the SLMed 316L SS in H₂O, a) potential versus time and b) current versus time. 65

Fig. 6.15 Comparison of the corrosion rate between the samples into the three electrolytes. The number of points for each corrosion test was 1024 points at a rate of 1 point per second. It is shown the average corrosion rate for each performed testing. 67

Fig. 6.16 Morphologies of the specimens after the electrochemical tests. Optical Microscope at 100X. XY plane: H ₂ O (a), NaCl (b), and H ₂ SO ₄ (c); XZ plane: H ₂ O (d), NaCl (e), and H ₂ SO ₄ (f).	68
Fig. 6.17 Morphologies of the specimens after the electrochemical tests in 3.5 wt. % NaCl at 500x and 1000x. XY plane (a), (b), and (c); XZ plane (d), (e), and (f). ZEISS EVO Scanning Electron Microscope (SEM).	69
Fig. 6.18 Morphologies of the specimens after the electrochemical tests in H ₂ SO ₄ at 500x and 1000x. XY plane (a), (b), and (c); XZ plane (d), (e), and (f). ZEISS EVO Scanning Electron Microscope (SEM).	70
Fig. A2.1 Temperature vs time at the center of each spot during the deposition of SLM AlSi10Mg alloy with a recoating time of 5×10^{-3} s, a) FDM and b) LBM111	
Fig. A2.2 Temperature vs XY position during the laser scanning and layer deposition of SLM AlSi10Mg. Simulation via FDM.	111
Fig. A2.3 Temperature vs XY position during the laser scanning and layer deposition of SLM AlSi10Mg. Simulation via LBM.	112
Fig. A2.4 Comparison of temperature values for the three simulated spots in the first layer via FDM and LBM.	112
Fig. A2.5 Comparison of temperature values for the three simulated spots in the second layer via FDM and LBM.	113
Fig. A2.6 Temperature vs time at the center of each spot during the deposition of SLM AlSi10Mg alloy with a recoating time of 5×10^{-2} s, a) FDM and b) LB	114

List of Tables

Table 3.1 Elemental composition (wt. %) of the AlSi10Mg metallic powder and SLM sample.....	19
Table 3.2 SLM processing parameters for the AlSi10Mg alloy.....	19
Table 3.3 Melt pool width and depth in the XZ and YZ plane of the SLM AlSi10Mg alloy.	21
Table 3.4 Elemental composition (wt. %) of the 316L SS metallic powder and SLM sample.....	23
Table 3.5 SLM processing parameters for the 316L SS alloy.....	23
Table 4.1 Physical properties in solid phase for the AlSi10Mg alloy.....	39
Table 4.2 Simulation parameters for AlSi10Mg.	40
Table 4.3 Physical properties in solid phase for the 316L SS alloy.....	41
Table 4.4 Simulation parameters for 316L SS.	41
Table 6.1 Estimated execution time for the LBM and FDM/FEM simulations.	58
Table 6.2 Electrochemical parameters of the SLMed 316L SS tested in horizontal (XY plane).....	62
Table 6.3 Electrochemical parameters of the SLMed 316L SS tested in vertical (XZ plane).	63
Table 6.4 Electrochemical noise (EN) characteristics of the SLMed 316L SS tested in the three electrolytes (3.5 wt. % NaCl, 20% H2SO4, and H2O)	66
Table A2.1 Simulation parameters for AlSi10Mg with laser movement, layer deposition, recoating time 5×10^{-3} s, and number of spots.	110
Table A2.2 Number of time steps for the FDM and LBM simulations considering a recoating time of 5×10^{-3} s.....	113

1 Introduction

1.1 Statement of the problem

Selective Laser Melting (SLM) is a multifaceted process that can generate several problems if it does not have adequate control. The most common issues found in SLM products are porosity, micro-cracks, distortion, and bad performance, which are generated due to the high thermal gradients produced during the process. The final properties, such as strength, work hardening, and corrosion resistance, of an SLM material depend mainly on thermal evolution, which is a function of a set of processing parameters. Therefore, numerical models for the simulation and control of temperature distribution to have an optimal SLM process are desired.

1.2 Justification

In the last years, advanced metallic alloys for complex aeronautical components have resulted more and more difficult to process by conventional methods. Additionally, there is a need of optimizing the materials to obtain lighter and stronger parts. In this case, a new method to manufacture aerospace metallic components known as SLM of Additive Manufacturing (AM) processes is attracting great attention in the aerospace industries. Nevertheless, it is very difficult to understand the physical phenomena of SLM due to its governed nonlinear partial differential equations, which play a significant effect on the final thermo-mechanical properties of the material. Therefore, advanced mathematical approaches need to be considered for the prediction of temperature evolution inside the SLM process.

1.3 Novelty statement

In this research work, the lattice Boltzmann method (LBM) based on the standard D2Q9 lattice structure is used to generate a model of SLM process for metallic materials. The most common methods to investigate the SLM process are the continuum methods like Finite Difference Method (FDM), Finite Element Method (FEM), Finite Volume Method (FVM), etc., although there are also certain investigations that have considered the LBM. In fact, the numerical models of SLM via LBM take into account metallic materials such as nickel and titanium-based superalloys rather than aluminum or steel alloys. According to this, the development of a numerical simulation for the laser melting process of aluminum or steel alloys represents a great opportunity to expand this research field. In addition, the measurement of corrosion resistance of an SLM material using linear

polarization resistance (LPR) and electrochemical noise (EN) technique also represents a great alternative to know the corrosion behavior and corrosion type that can be developed on the material.

1.4 Hypothesis

The development of a 2D LBM for studying the SLM problem in the present research allows to observe the interaction between the laser and material. A numerical simulation of SLM using LBM can predict the melt pool dimensions (width and depth), which are important parameters to investigate the final properties of the metal parts. The numerical model uses the SLM processing parameters as input variables, which can be optimized for obtaining optimum final properties of an SLM material.

1.5 Objectives of the research

Generate a numerical model for simulating the thermal effect, the impact of the laser on the material, and melt pool geometry during the SLM process of metallic materials.

- Obtain a 2D numerical model based on the LBM to predict the temperature field and melt pool dimensions of an SLM Al alloy.
- Develop a 2D numerical simulation based on the LBM to predict the thermal effect and melt pool dimensions of an SLM steel alloy.
- Produce metallic specimens via SLM using the AlSi10Mg and 316L Stainless Steel (316L SS) alloys to characterize and obtain their microstructure and melt pool dimensions.
- Study the relationship between surface features and corrosion resistance of the 316L SS alloy processed by SLM.

1.6 Methodology

In order to develop the numerical model of SLM process, three stages are defined and described as follow:

The first part consists of obtaining knowledge about the SLM process. Particularly, to understand the physics of the phenomenon. In this part, a previous 2D simulation is developed by FEM and FDM. In addition, an initial 2D LBM simulation is developed using the D2Q4 lattice structure. The

purpose is to understand how the SLM process works. The numerical results of the performed simulations are presented in the section of results and the solution procedure is only highlighted for the LBM D2Q9.

In the second part, two numerical simulations of SLM using the standard D2Q9 lattice structure are developed. For the first numerical model, an AlSi10Mg Al alloy is considered while for the second model the 316L SS alloy is selected. Both simulations can predict the thermal evolution during the process, generating the melt pool produced by the simulated laser beam. The model considers some of the most important SLM processing parameters, such as laser power, spot irradiation time, ambient temperature, and the preheating temperature of the medium.

Then, the final part focuses on experimental observation, as well as the validation and presentation of results. In this stage, metallic samples were fabricated via SLM using the two metallic alloys considered in the simulations. The SLM samples were characterized according to the corresponding methods (OM, SEM, etc.) in order to obtain the morphology and melt pool characterization (width and depth of the melt pool) of each selected material. Experimental results are used to qualitatively validate the simulation results. Further, the dimensional values in width and depth of the melt pool are very important because they are the main factors to predict and control the solidification behavior (future work) of a metallic material produced by SLM. Additionally, the corrosion resistance of the SLM 316L SS was measured in order to relate the surface features and the electrochemical properties. Fig. 1.1 depicts schematically the methodology used in this research work.

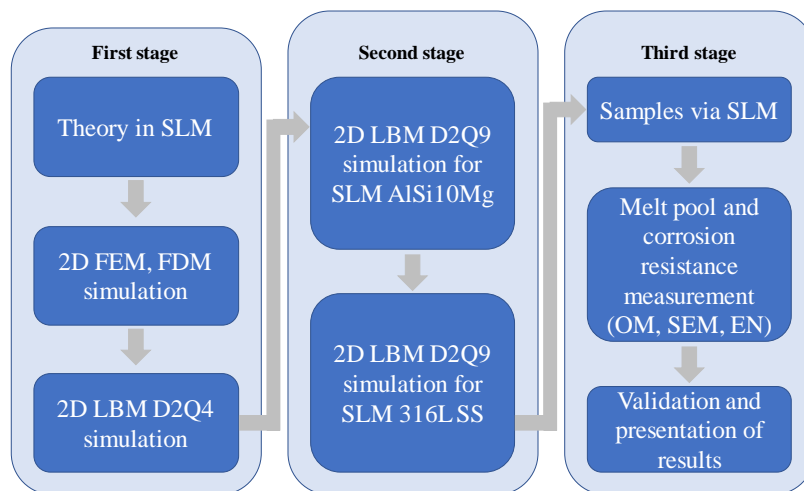


Fig. 1.1 Methodological scheme of the present investigation.

2 Literature review

2.1 Selective Laser Melting (SLM) process

SLM, categorized as an AM process, is a disruptive technology [1] that has the ability to fabricate three-dimensional components with high levels of complexity from powder metallic alloys, such as nickel, titanium, aluminum, steel-based, etc. [2, 3]. This technique uses a laser of high-power to selectively melt and fuse metallic powder beds considering a successive layer deposition of the material. In the SLM process, hundreds or thousands of powder layers according to the part height are programmed with a well-known thickness that generally ranges between 20 and 110 μm [4], also depending on the particle size of the material [5], to be deposited on a preheated build substrate. In this case, the laser scans the deposited layer following the cross-section of the CAD model. The process finishes up to the part is completely built.

During the process, a set of steps are involved which go out from modeling the desired part up to removing the part attached to the building platform. As the first step, the CAD model is converted to a file format widely used by AM processes known as STereoLithography (STL) file, which is then divided into multiples slices by a specialized software (Magics) in order to get the SLM file. Each slice represents a powder layer spread by a wiper on the substrate of the building platform, which is also preheated to marginally bring together the powder particles. The preheating process is necessary since it helps to prevent powder scattering [6]. In the next step, the laser impacts on the powder bed to melt and fuse the material, creating the 2D cross-section of the desired part. Then, the platform is moved one layer thickness below in order to deposit a new powder layer. Herein, the laser is newly activated to continue scanning the part and this is realized several times up to the last layer is deposited and scanned. To get an idea about the general principle of the SLM process, Fig. 2.1 shows a representative scheme of this technology.

Finally, when the laser finishes scanning all the powder layers, the platform goes back to its initial position to remove the loose powder no scanned during the process. Then, the SLM component attached to the substrate is taken out from the build compartment and both parts are manually separated or using an additional cutting process. It is worthy to mention that the building chamber is filled with nitrogen or argon gas to generate a noble atmosphere in order to protect the SLM component from oxidation. The gaseous environment composition of the process has a high influence on the material's tensile properties. The AlSi10Mg alloy processed by SLM under a

nitrogen environment presents the maximum strength (385 ± 5 MPa) compared to the lowest strength (338 ± 2 MPa) under an argon environment [7].

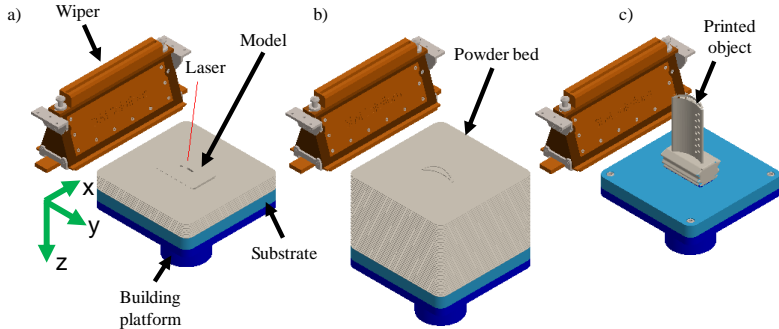


Fig. 2.1 It is shown the general principle of the SLM process, a) the laser scans the cross-sectioned of the CAD model, b) SLM component inside the powder bed after scanning all the layers, and c) SLM component obtained after removing the no melted powder.

A great variety of metallic alloys can be processed by SLM, e.g., nickel, titanium, aluminum, steel, stainless steel, etc. Furthermore, the SLM technology has the potential to manufacture special components, which could be very difficult to produce using traditional methods. Thanks to this, several industrial sectors like the biomedical, automotive, energy, and aerospace, have begun to use this technology to produce complex parts. For example, in the aerospace field, parts such as gas turbine blades, fuel nozzle, housing for the sensors, and other components can be produced without any issue. Fig. 2.2 shows some aerospace metallic components that have been manufactured by AM processes.

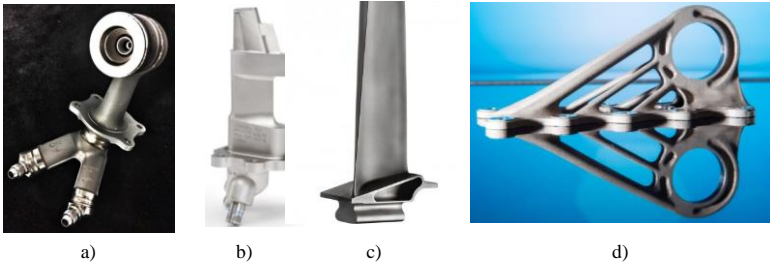


Fig. 2.2 Success cases of AM components, a) CFM International’s 3D-printed fuel nozzle, b) housing for the sensor T25 (one of the first 3D-printed engine components approved by FAA ready to fly inside commercial jet engines such as GE9X and Boeing 777s), c) Titanium Aluminide Low-Pressure Turbine blade, and d) Airbus’s A350 bracket [8].

Fig. 2.2a illustrates a GE's 3D printed fuel nozzle fabricated in one single part after the same component was integrated by an assembly of more than twenty parts in the traditional form. The fuel nozzle weight was reduced up to 25% using the AM technique. In Fig. 2.2b, it is shown a 3D-printed housing for the sensor T25, which was the first component approved by the Federal Aviation Administration (FAA) for flying into commercial jet engines such as GE9X and Boeing 777s. The housing was processed by a cobalt chrome alloy. From Fig. 2.2c, a gas turbine blade has been fabricated by AM considering an alloy of Titanium Aluminides, which could be the next generation of gas turbine blades used for the low-pressure turbines. Titanium aluminide (TiAl)-based alloy is lighter than the nickel-based superalloys. In Fig. 2.2d, the Airbus's A350 bracket is also an AM-part, which was changed from conventional manufacturing to a 3D printing process to speed up the production.

2.2 Physics of SLM

SLM is a complex process that involves heating and melting metallic powder alloys in order to form three-dimensional components. The process uses the power of a laser as energy source to impact the powder bed, generating a small molten material volume known as melt pool, which is characterized by a semicircular shape with a depth and width (melt pool dimensions), as shown in Fig. 2.3. The macrostructure of SLM materials comes when several melt pools, small circular or cylindrical parts [9], form a relatively tidy trajectory of segments that is melted several times during the melting process [10]. The SLM processing parameters that influence strongly the melt pool dimensions are laser power (P in J/s), scanning speed (v in mm/s), hatch spacing (HS in mm) between two consecutive tracks, melting strategy, layer thickness (t in mm), and return time (t in s) of the laser beam [11]. So, the laser energy density (E in J/mm³) to melt the material is given by Eq. 2.1 [10–12] as

$$E = \frac{P}{HS \cdot v \cdot t} \quad (2.1)$$

During the SLM process, a combination of several heat transfer mechanisms, such as convection, radiation, absorption, conduction, etc., takes place, being thermal conduction the most important factor in the melt pool [13]. Additionally, other complex phenomena such as chaotic effects of instability in the melt pool due to a high surface tension produced by a high laser energy density combined with the low viscosity of liquid metals [5], the laser energy absorptivity of powder

materials and scattering to laser radiation [9], Marangoni convection [14], material evaporation [15], capillarity forces, gravity, etc., are also derived. Unfortunately, such physical phenomena influence strongly the mechanical properties (hardness, strength, ductility, specific wear rate, etc.) and the microstructural features (grain size, morphology, and texture) of the SLM materials. Therefore, mathematical approaches need to be considered for obtaining optimum processing parameters without having to do expensive experiments with numerous measurements.

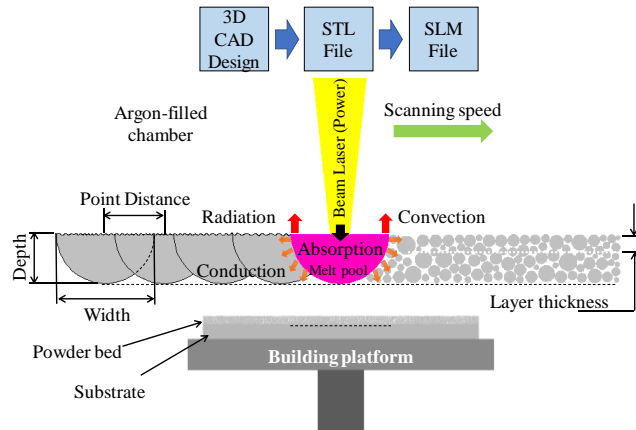


Fig. 2.3 2D schematic representation to show the macrostructure and main processing parameters such as laser power, scanning speed, hatch spacing, and layer thickness of the SLM process.

In consequence, several defects such as porosity, microcracks, and not well-consolidated layers are derived from the SLM process. For instance, porosity is one of the main viewpoints of scientific communities, which has been studied by a correlation between the SLM processing parameters (laser energy density Eq. 2.1) and porosity levels in the microstructure of the material [16], as shown in Fig. 2.4.

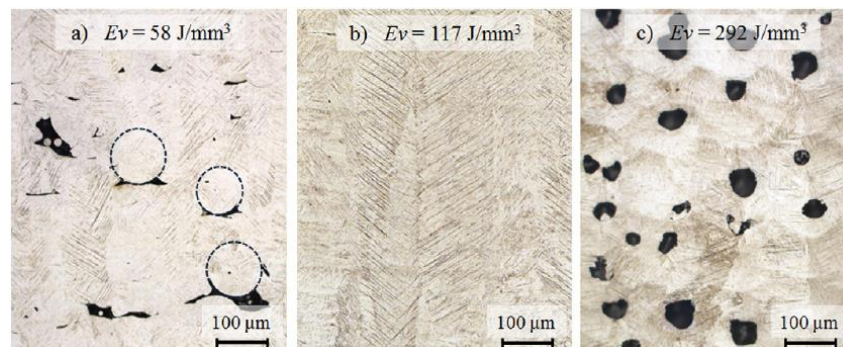


Fig. 2.4 2D Pore morphologies obtained by LOM after SLM processing with different energy densities [16].

2.3 Aeronautical alloys used for SLM process

There exists a wide range of aeronautical alloys that can be used to fabricate a new generation of structural components for aircraft engines via SLM. These alloys can be nickel, titanium, aluminum, steel-based, etc. For example, nickel-based superalloys are potential candidates for gas turbine components, as shown in Fig. 2.5. These superalloys are widely used to fabricate gas turbine blades due to their high resistance at elevated temperatures. Nickel-based superalloys are also characterized by their excellent corrosion resistance and good fatigue life. Some studies have evaluated their anisotropic behavior (microstructure and mechanical properties different at different orientations inside the metallic structure [17]) when the parts are processed by SLM in different orientations with respect to the build direction. Also, at the same time nickel-based superalloys have been treated by SLM in order to compare their physical properties against the counterparts. For example, it has been proved that the Inconel 738 LC (IN738LC) alloy processed by SLM increases its Young's modulus up to 19% higher than the cast material [18].

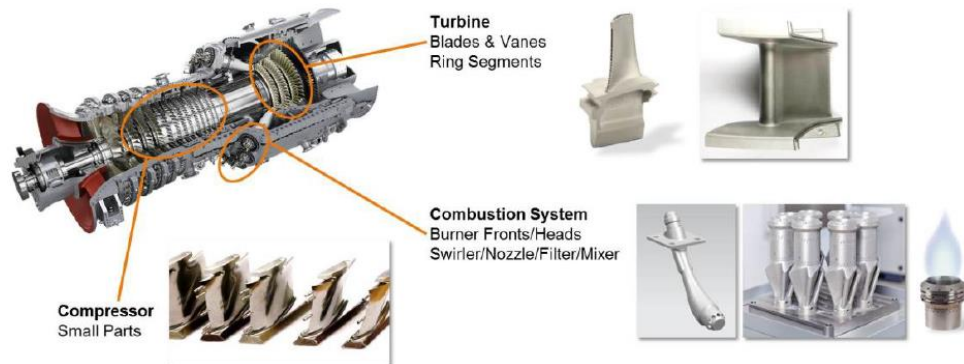


Fig. 2.5 Inconel superalloy application in gas turbine applications [19].

IN625 nickel-based Inconel superalloy is also familiar with AM processes. This alloy is mostly used in the aerospace field to fabricate components for jet engines and gas turbines [20]. Nevertheless, SLM of IN625 has not resulted very well due to the dislocations, precipitates, and residual stresses generated during the process [21]. Therefore, some investigations on SLM with IN625 have conducted to find optimum processing parameters, which focused on improving surface roughness and porosity in the material [22]. Likewise, IN625 lattice structures have been processed by SLM to identify their mechanical response based on the Design of Experiments (DOE) [19]. The SLM IN625 lattice structures were studied to find manufacturability limits associated with the porosity distribution.

Aluminum-based alloys are also potential candidates to be processed by SLM. These alloys, thanks to their lightweight, are widely used to fabricate structures for the aerospace and automotive industry. An extensive list of aluminum alloys processed by SLM can be found in the literature [23–26]. For example, AlSi10Mg alloy treated by SLM has a tremendous potential to develop a fine microstructure and offers great castability, good weldability, and high corrosion resistance. Although there are some issues (dimensional accuracy, surface finish, and mechanical properties) not still solved during the laser melting processes, this alloy is friendly with SLM. The study of the AlSi10Mg alloy has conducted to compare its mechanical properties between the casting and SLM. It has been found that the SLM AlSi10Mg exhibits higher tensile strength than the casting material [27], as a result of an extremely fine microstructure. Though it is known that the SLM process of aluminum alloys is more difficult than that of steel and Ti alloys, there are several aluminum alloys processed by SLM such as AA-2024 [2], AA-357 [17], and AA-6061 [28]. One of the main issues to process Al alloys by SLM is their elevated reflectivity and low absorption coefficient to the laser radiation.

Ti-based alloys, also considered for aerospace and automotive applications [15], have also been coming to be manufactured by SLM. The most common additively manufactured Ti alloy is Ti6Al4V. Although this alloy is considered an easy material to be processed by SLM [29], there are some issues or structural defects (pores, cracks, residual stresses, microstructure, etc.) that must be still solved. For instance, the SLM Ti alloys develops a martensitic microstructure with low ductility [29] due to the rapid melt pool solidification of the process, although it can be improved by post-processing heat treatments. Knowing that there are several problems of SLM like with other metallic alloys, these ones can be solved by optimizing the processing parameters, making a great number of expensive experiments. In a similar way, Intermetallic γ -TiAl based alloys are potential candidates for the fabrication of gas turbine components. These alloys can be processed by SLM and are studied to understand the cracking behavior and methods of cracks [30].

2.4 Numerical models for SLM process

Nowadays, new manufacturing methodologies such as SLM have come to make a reality in the production of metal components with geometric complexities. Nevertheless, to better understand these approaches it is necessary the development of numerical powerful methods. Therefore, scientific and engineering communities are taking into account numerical models to describe the SLM process like in [2, 5, 13, 31–34]. The SLM numerical models have been commonly used to

predict molten pool dimensions, thermal effect, residual stresses, etc., of metallic materials processed by SLM.

Lopez-Botello et al. [2] developed a 2D coupled model based on the Cellular Automata (CA) and Finite Element (FE) (CA-FE) methods for the prediction of melt pool dimensions and thermal and microstructure evolution during the SLM process of an AA-2024 Al alloy. The CA-FE model takes into account the phase changes, including the powder, liquid, and solid phase, of the processed material as well as melt pool formation in several tracks and layers. Fig. 2.6 shows an evaluation of the melt pool size between the numerical and experimental results of the SLM AA-2024 Al alloy. The experimental results indicated that the melt pool width varies between 240 μm and 304.95 μm and the melt pool depth between 72.42 μm and 94.63 μm . Then, according to the numerical simulation, it was calculated that the width and depth of the melt pool are 320 μm and 115 μm , respectively, having a 14% error with the experimental results.

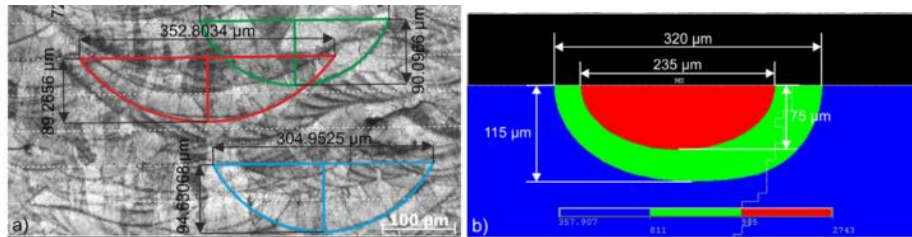


Fig. 2.6 Melt pool measurement undertaken to a) experimental sample 1, b) FEM model for sample number 1 [2].

Liu et al. [13] used a 3D finite element model for predicting the melt pool dimensions using the AlSi10Mg alloy processed by SLM. The model considers anisotropic thermal conductivities to improve the melt pool dimensions. Additionally, it was performed a prediction of microstructure considering the columnar to equiaxed transition (CET) criterion, which was used to connect the experimental results with the simulated thermal variables (temperature gradient, cooling rate, and solidification rate) of the melt pool. The experimental and simulation results give a maximum error in the melt pool dimensions of 8.6%. Fig. 2.7 shows the comparison between the numerical and experimental observation. According to the authors, they emphasize that the melt pool dimensions, the surface properties of the melt track, and the temperature field are important factors to understand solidification behavior and predict the microstructure during the SLM process.

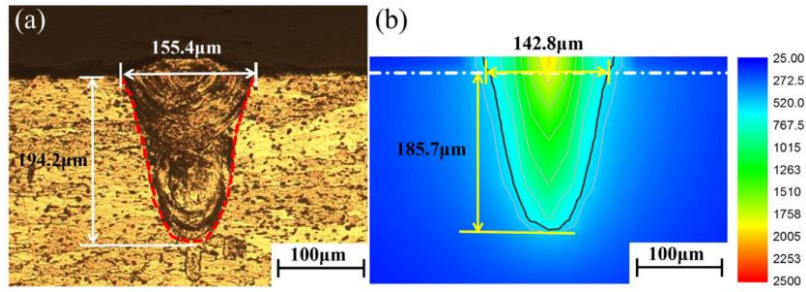


Fig. 2.7 The cross-section morphology of 3# sample molten pool experimental model (a) and numerical model (b) [13].

Li et al. [35] also developed a numerical model of SLM based on the FEM to study the melt pool dimensions and temperature field of the AlSi10Mg alloy. Their study shows that the melt pool characterization is calculated for different values of laser power and scan speed. It was found that there exists an optimum value for width (114.4 μm) and depth (67.5 μm) that belong to a successful SLM process, which uses a 250 W laser power and a 200 mm/s scan speed. Fig. 2.8 shows the temperature distribution viewed from the top surface and cross-section of the most acceptable melt pool.

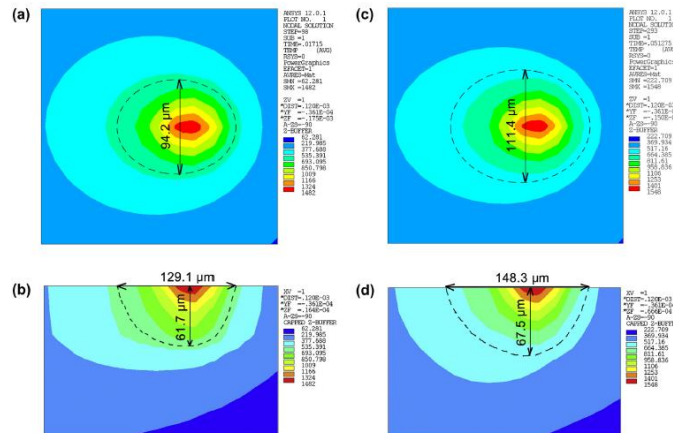


Fig. 2.8 Temperature distribution during SLM process at $P = 250 \text{ W}$ and $v = 250 \text{ mm/s}$: (a) on the top surface of the molten pool and (b) on the cross-section of the molten pool as the laser beam reached the center of the first layer; (c) on the top surface of the molten pool and (d) on the cross-section of the molten pool as the laser beam reached the center of the second layer [35].

On the other hand, in Rai et al.'s [32] study, a new coupled model between the cellular automaton (CA) and lattice Boltzmann (LB) (CA-LB) was introduced to study the SLM IN718 alloy. This

important numerical model was used to highlight a more correct description of the SLM process than those of the FEM. The CA-LB method has the potential to incorporate several physical phenomena such as stochastic effects, energy absorption, evaporation, melt pool movement, and grain growth. The numerical prediction of SLM was performed in 2D and used to investigate the influence of processing parameters and scanning strategy on the final grain structure of the selected part. Fig. 2.9 shows the CA-LB initial numerical set-up which depicts the substrate, powder bed, and the electron laser beam.

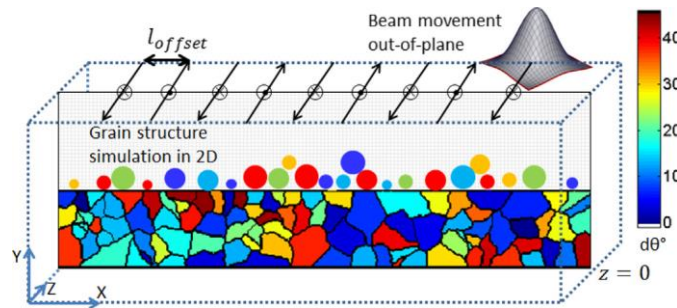


Fig. 2.9 CALB model initial set-up with an equiaxed base plate, powder bed and an electron beam heat source. The color bar maps the grain misorientation with respect to the build direction (y-axis) [32].

In fact, the LBM used to form the CA-LB model was developed by Körner et al. [5] who employ a randomly packed powder bed subjected to Gaussian beam irradiation during the selective electron beam melting (SEBM) process. Although the LBM considers one single layer, that approach calculates the results by considering individual powder particles and is able to make a proper description of several complex physical phenomena such as powder density, stochastic effects inside the powder bed, capillary forces, etc., which can result in difficulty to observe by standard continuum mediums. The results obtained by the CA-LB model show a process map that demonstrates the effect of the laser power and scan speed on the obtained grain structure. Fig. 2.10 shows the laser beam irradiation on the powder particles and how the laser energy is absorbed by the material, forming the melt pool. On the right side, it is schematically illustrated the numerical domain, showing how the laser energy is absorbed by the numerical cells. This model is so powerful due to it uses a multi-distribution function method which allows solving the macroscopic equations of heat and mass transfer involved during complex processes such as SLM.

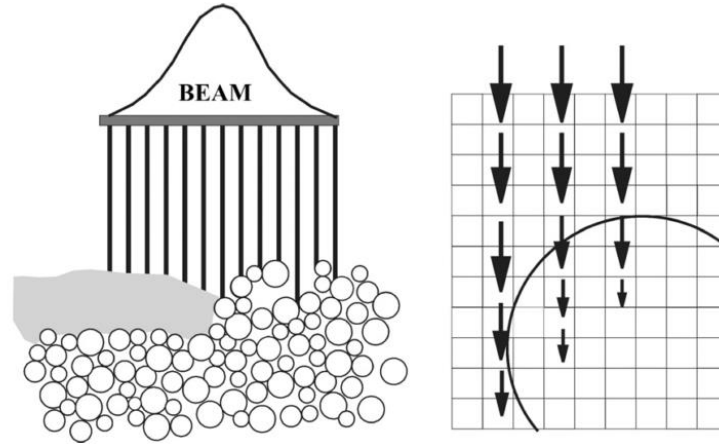


Fig. 2.10 Beam absorption. Left: absorption of the beam into the powder layer and melt pool that develops. Right: absorption of the beam within a powder particle. The numerical grid is schematically shown [5].

Recently, Zheng et al. [36] also developed a numerical model of SLM for studying the melt pool movement and porosity. The interesting of that approach is that it uses a height function-lattice Boltzmann method (HF-LBM) coupled model which considers interfacial forces via surface tension, Marangoni convection, and recoil pressure. The model predicts porosity formation mechanisms for different laser energy and powder packing densities. According to the results, it was found that the melt track formed at a 120 W laser power and 1200 mm/s scanning speed exhibits porosity formation as a result of lack of fusion while at high laser energy densities the melt track displays porosity in the form of trapped gases. Fig. 2.11 shows the numerical results obtained by HF-LBM, which represent the melt track morphology.

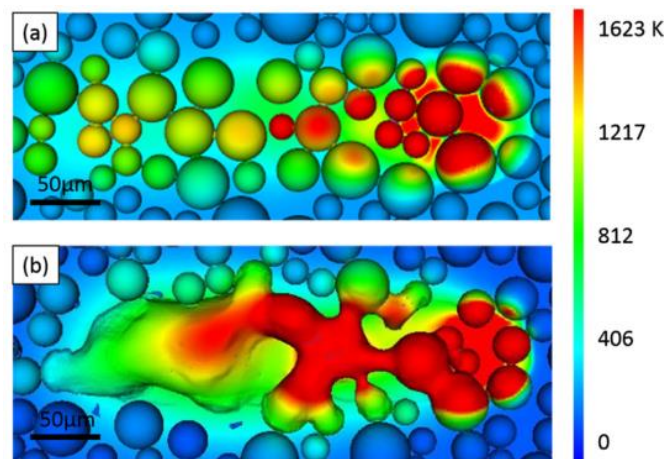


Fig. 2.11 Molten pool morphology under the influence of gravity (a) and surface tension (b) [36].

With some of the strongest previous investigations, it is important to see how the LBM is used for studying selective laser beam melting processes issues. In comparison with the continuum approaches, there exists a great difference since the LBM has the potential to incorporate several complex physical phenomena. In addition to that, the governing equations for heat and mass transfer can be easily solved by only two steps known as streaming and collision, which are discussed in the next chapters. As shown previously, few SLM investigations have incorporated the LBM, but there will be always different opportunities to extend the knowledge about the SLM process using this powerful tool like the LBM.

Therefore, this investigation uses the LBM for simulating the melt pool formation defined by the temperature field of metallic alloys processed by SLM. For the obtention of numerical results more accurate in future investigations, it is expected that the model works as a processing parameters optimization tool capable to reduce energy consumption, cost, and time of processing parts, as well as potentialize in SLM materials with high properties.

2.5 Dimensionless approaches for studying SLM

As far as we know the continuum and discrete methods have been up to now the most used tools to study additive manufacturing process. Nevertheless, there are other approaches based on dimensionless analyses with promising results in the simulation of the melt pool of the SLM process. In this context, Grossmann et al. [37] have developed a scaling law to predict the width of a single track as a function of the process and material parameters. Their study emphasizes that the melt pool width b can be obtained throughout a function of six independent input parameters (manufacturing and material parameters), which are the scanning speed v , the laser power P , the change in temperature ΔT (difference of the initial and liquid state of the powder), the volumetric heat capacity $\rho \cdot C_p$ and the heat conductivity k . Such SLM function was defined as:

$$b = F(v, P, \Delta T, \rho \cdot C_p, k) \quad (2.2)$$

In that study, it was used Buckingham Π -theorem for defining two important dimensionless numbers, which relate the melt pool geometry (width) with the corresponding governing parameters. Although the dimensionless model neglected the radiation and re-solidification transfer mechanisms as well as other important laser (beam diameter, hatch distance) and material (layer thickness, powder shape, absorptivity, etc.) parameters, it was established that the melt pool width

scales the square root of the line energy input $E_L = P/v$. This study showed an initial calculation to study the melt pool geometry based on dimensionless numbers.

Subsequently, Grossmann et al. [38], in a second study, incorporated the hatch distance HS of the laser where now equation 2.2 is given as a function of seven dimensional input parameters, considering the product of the specific heat capacity and density as one parameter. This new methodology also based on dimensionless analysis allowed to describe the geometry of a single or double track. The difference with their previous work is that it was developed a dimensionless scaling law for contour exposure, which can determine the width of two adjacent melt tracks as a function of the processing parameters.

Later, an enhanced dimensionless model was introduced by Yang et al. [39], using a new linear energy density formulation. This stronger methodology than the corresponding prior works allows to predict the melt pool geometry based on different powders and machine types. This is because the new dimensionless formulation can incorporate the powder size and the beam diameter during the simulation, mathematically as a dimensionless coefficient calculated by these two processing parameters. These models have been used to manufacture thin walled lattice structures, in the micrometer range, for engineering applications such as medical implants, crash absorbers, or heat exchangers. It is worthy to mention that this constitutive scaling law has the potential to monitor in real-time the melt pool geometry, defects and failure detection during the manufacture of a metallic component processed by LPBF, ensuring the component's quality.

On the other hand, the dimensional analyses based on Buckingham Π -theorem have also been used to study the densification of AM parts processed by SLM. In this case, Estrada-Díaz et al. [40] developed a dimensional expression to produce dense metallic parts via SLM. Using two dimensionless numbers derived from the powder material properties and processing parameters, it was developed a general expression to determine the scanning speed needed to produce SLM components with the desired bulk density as a function of the laser power. The predicted results using the bulk density equation have been compared with experimental data, specifically for the manufacture of IN718, AlSi10Mg, and Ti6Al4V alloys.

Due to there is always the need to enhance prior research works, Estrada-Díaz et al. [41] introduced a new bulk density expression adding the hatch distance, the thermal conductivity, and specific heat capacity as independent variables to produce SLM metallic parts. This new contribution can predict

the densification of a wide range of metallic alloys processed by selective laser melting. According to their previous work, it was obtained a constitutive expression to calculate the scanning speed as a function of the laser power, taking into account the desired porosity for applications where needed.

As stressed above, the dimensionless approaches also play an important role in the simulation of the SLM process. The beauty of these tools is the generation of scaling laws that can predict rapidly the final properties of AM parts. With such formulations, it can prevent the manufacture of several parts as well as numerous measurements for studying the final properties. This contributes to minimizing production cost, energy cost, and material characterization cost during the processing of AM parts. Additionally, the dimensionless tools can relate to continuum and discrete methodologies to obtain a complete formulation due to the dimensionless expressions in some cases have neglected the phenomena like the Marangoni effect, capillary forces, etc. involved in the SLM process. Besides, the connection can also be performed with other applications like Cellular Automata (for the study of the solidification process), lattice Boltzmann (for the study of the thermal variables and the comparison of the melt pool geometry), and machine learning.

2.6 Summary

SLM is an AM technique that can fabricate high complexity geometries. It is a complex process controlled by heat and mass transfer in the melt pool that needs to be studied by numerical techniques to better understand and control it since the experimental investigations would result in high costs with numerous measurements. Although there are successful studies that have been followed the FEM and FVM approaches, few have considered the mesoscopic approaches like the LBM. Therefore, here is a great opportunity to continue expanding the knowledge of the SLM process using mesoscopic models. A numerical model for the research of the SLM process is highly efficient due to AM processes such as SLM and numerical techniques for process optimization work increasingly hand-in-hand to produce advanced metallic materials with high properties.

3 Experimental Methodology

This chapter shows the manufacturing and characterization of metallic parts produced by the SLM process. The aim is to obtain SLM metallic samples for studying the influence of SLM processing parameters on the final characteristics (melt pool dimensions) of the material. The experimental results obtained through this methodology allow knowing the melt pool features produced by the laser beam, as well as the microstructure. Firstly, an Aluminum alloy (AlSi10Mg) was used to manufacture SLM samples, which were characterized to measure their melt pool width and depth. Secondly, a stainless-steel alloy (316L SS) was selected to be processed via SLM, obtaining metallic samples that then were analyzed to measure their molten pool dimensions. The experimental results of this work can be used to qualitatively validate the numerical results.

3.1 Materials and Methods

An SLM 280HL (SLM Solutions Inc., Lübeck Germany) equipped with one 400 W CW Ytterbium fiber laser was used to manufacture all the samples (AlSi10Mg and 316L SS). The laser is a water-cooled continuum mode, has a diameter of approximately 70 μm , and uses a wavelength of 1060 nm. The SLM machine employs an Argon-filled chamber to produce an inert atmosphere during the process and has a working space with dimensions of 280 mm \times 280 mm \times 350 mm used to build the desired SLM component. Fig. 3.1 shows the SLM 280 HL system where the metallic samples of this investigation were built.



Fig. 3.1 SLM 280 HL machine to build metallic sample (AlSi10Mg and 316L SS) for this investigation.

3.2 AlSi10Mg samples fabricated by SLM

AlSi10Mg alloy in its nearly spherical shape (20-63 μm) shown in Fig. 3.2 and supplied by LPW Technology with its elemental composition (wt. %) shown in Table 3.1 was selected to fabricate cubic parts of 10 mm \times 10 mm \times 10 mm using the SLM process. The AlSi10Mg features like particle size and chemical composition were taken by scanning electron microscopy (SEM) and energy dispersive spectroscopy (EDS) analyses, respectively. The EDS observation was carried out in one of the powder particles for showing its chemical structure with the major alloying elements. Besides the elemental composition of the material considering its spherical phase, Table 3.1 also shows the chemical composition of the solid phase, i.e., as SLM material after its construction, taken by x-ray fluorescence spectroscopy (XRF). Although the XRF analysis does not show a complete chemical composition like the manufacturer elemental composition, it shows the major alloying elements like the EDS results.

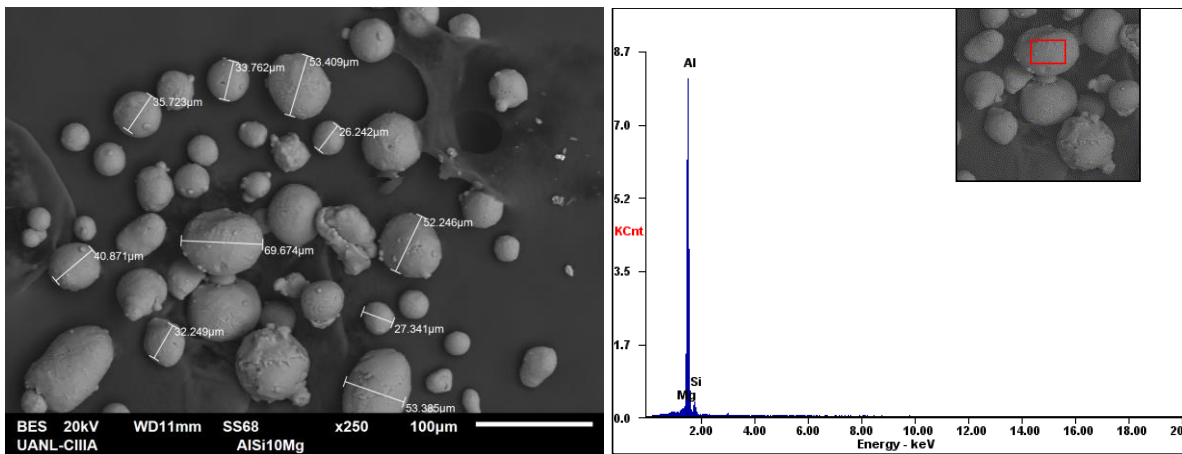


Fig. 3.2 SEM image of the AlSi10Mg metal powder taken by the present investigation showing the size of some particles (left side) and an EDS analysis in one of those particles (right side).

The manufacturing of the samples was performed with a 30 μm layer thickness, 100 W laser power, 100 mm/s scanning speed, and 100 μm hatch spacing under a controlled atmosphere with Argon gas. The generated inert ambient allows controlling the oxygen levels to less than 0.1% during the SLM process. The manufacturing process started with the preheating of the substrate in order to reduce internal forces and deformation, which are some of the main factors that affect the final properties of the material [27]. Therefore, the building platform was pre-heated at 200 $^{\circ}\text{C}$. In order to resume the SLM processing parameters of the AlSi10Mg alloy, Table 3.2 shows the corresponding values to produce the metallic samples of 10 mm \times 10 mm \times 10 mm.

Table 3.1 Elemental composition (wt. %) of the AlSi10Mg metallic powder and SLM sample.

Element	Cu	Fe	Mg	Mn	N	Ni	O	Pb	Si	Ti	Zn	Al
Powder	0.05	0.25	0.25-0.45	0.10	0.20	0.05	0.20	0.02	9.0 – 11.0	0.15	0.1	Bal.
SLM sample	-	0.17	1.09	-	-	0.006	-	-	10.82	-	0.00 67	Bal.

As Table 3.2 shows, ambient temperature T_a also accounts as an SLM processing parameter and corresponds to the environment temperature inside the building chamber that generally is at 25 °C. On the other hand, another important parameter also considered for the manufacturing of SLM products is the laser energy absorptivity [13]. This parameter, more own and different for each metallic material [42], defines the useful amount of laser energy absorbed by the material. The absorptivity factor, typically considered constant [43], depends on various processing and material parameters, of which the wavelength of the laser, the mean particle size, and the particle shape are the most important [44]. The laser energy absorptivity for the AlSi10Mg alloy has a value of 0.09 [45] and is taken into account for the simulation procedures in the next chapter.

Table 3.2 SLM processing parameters for the AlSi10Mg alloy.

Parameter	Value
Ambient temperature, T_a (K)	298
Powder layer thickness, t (μm)	30
Laser diameter, D (μm)	70
Hatch spacing, HS (μm)	100
Laser power, P (W)	100
Scanning speed, v (mm/s)	100

Fig. 3.3 shows the AlSi10Mg specimens fabricated by SLM. As previously discussed, the samples are a cubic form of 10 mm \times 10 mm \times 10 mm, in order to be sectioned and analyze their microstructure.

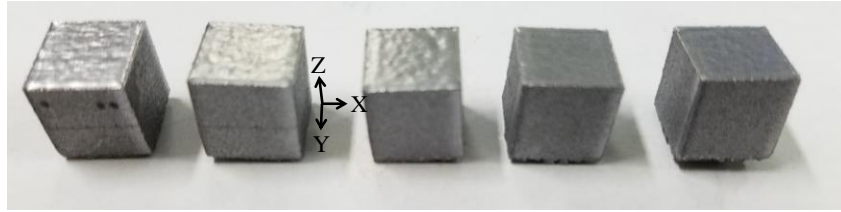


Fig. 3.3 SLM AlSi10Mg parts.

3.3 Experimental melt pool morphology of SLM AlSi10Mg alloy

Once the manufacturing of AlSi10Mg parts was performed, the next step was obtaining the cross-section of the sample to mount and polish it. Therefore, each sample was divided into two different vertical planes (XZ and YZ) and one horizontal plane (XY), getting eight samples per each built part, as shown schematically in Fig. 3.4. The first samples (1, 2, 3, and 4) correspond to the XZ plane above the XY plane, and the other (5, 6, 7, and 8) to the YZ plane below the XY plane. The Z-axis corresponds to the building direction and all the planes are placed at the half of the part.

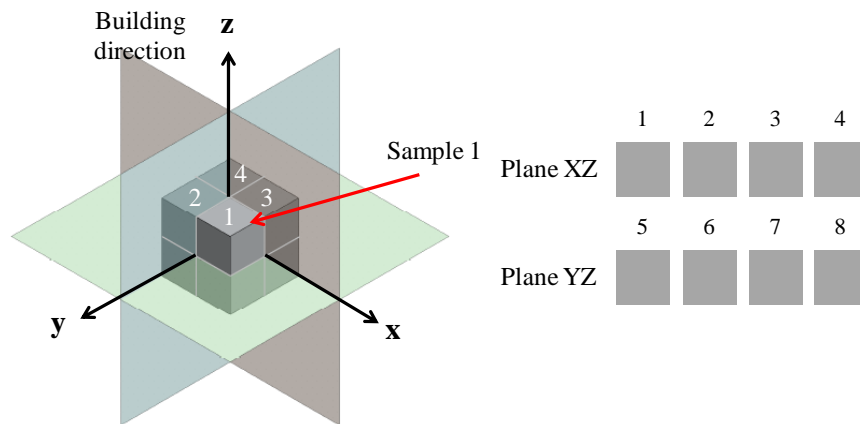


Fig. 3.4 Cutting plane showing how the SLM AlSi10Mg samples were cut.

For the observation of the melt pool morphology in the SLM AlSi10Mg alloy, the samples were etched with Keller's reagent (190 ml distilled water, 5 ml HNO₃, 3 ml HCl, 2 ml HF for 10 seconds). Then, a Zeiss axiobserver.Z1m optical microscope was used to observe the melt pool shape. Twenty melt pool measurements were performed per each micrograph at different positions. Table 3.3 shows the average width and depth of the melt pool for each plane (XZ and YZ). The dimensions of the melt pool were calculated like a total dimension averaged between the two planes, as shown in Table 3.3.

Table 3.3 Melt pool width and depth in the XZ and YZ plane of the SLM AlSi10Mg alloy.

	XZ plane		YZ plane		Total	
	Width (μm)	Depth (μm)	Width (μm)	Depth (μm)	Width (μm)	Depth (μm)
Standard deviation	27.75	18.80	24.78	14.39	27.21	16.92
Average	201.40	75.14	182.81	62.85	192.1	68.9

Additionally, the grain structure of the SLM AlSi10Mg material was obtained. For this case, the specimens were newly polished and etched with Keller's reagent. Then, a second attack using an electrolytic solution with Barker's reagent (2.5 ml HBF_4 , 200 ml distilled water during 5s at 2V) was used. In order to observe the microstructure, a polarized light in the optical microscope was needed. Although the grains are not so defined by the optical micrograph, Fig. 3.5 shows the microstructure obtained by the second attack. Following the white arrow shown in Fig. 3.5, it seems that the grains tend to grow up to the center of the melt pool, i.e., columnar grains are formed during the laser melting process of AlSi10Mg.

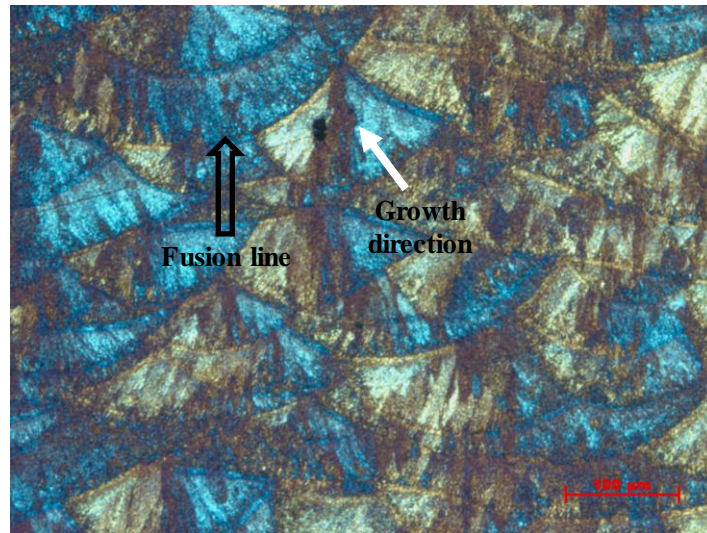


Fig. 3.5 Optical micrograph showing the SLM AlSi10Mg microstructure, parallel to the build direction. The growth direction is designated with the white arrow while the fusion line is shown with the open arrow.

As previously shown, the experimental methodology for measuring the melt pool dimensions of the SLM AlSi10Mg alloy was properly performed. This observation allows showing the influence of the laser on the material. It can be found in the literature that the knowledge of the melt pool dimensions in SLM materials is an important factor for the prediction of the final strength. Even, a large penetration depth of the melt pool may cause undesired effects like entrapped gasses or residual gas at the bottom. Such gases could represent serious problems due to in some cases cannot escape due to the rapid solidification of the process [15].

3.4 316L SS samples fabricated by SLM

The second fabrication of SLM samples using metal powder alloy was performed in this investigation. Thus, the 316L SS alloy characterized by its nearly spherical shape (10-45 μm) as shown in Fig. 3.6 and produced by LPW Technology with the chemical composition (wt. %) shown in Table 3.4 was chosen to produce cubic samples. The SLM process was carried out in the SLM 280HL machine, selecting as processing parameters a 30 μm layer thickness, 400 W laser power, 110 μm hatch spacing, and 230 mm/s scanning speed. The building chamber was filled with Argon gas up to have and maintain the oxygen concentrations below 0.1% to prevent the parts oxidation. After the construction of the samples, they were also analyzed by x-ray fluorescence spectroscopy (XRF) to verify their elemental composition, as shown in Table 3.4.

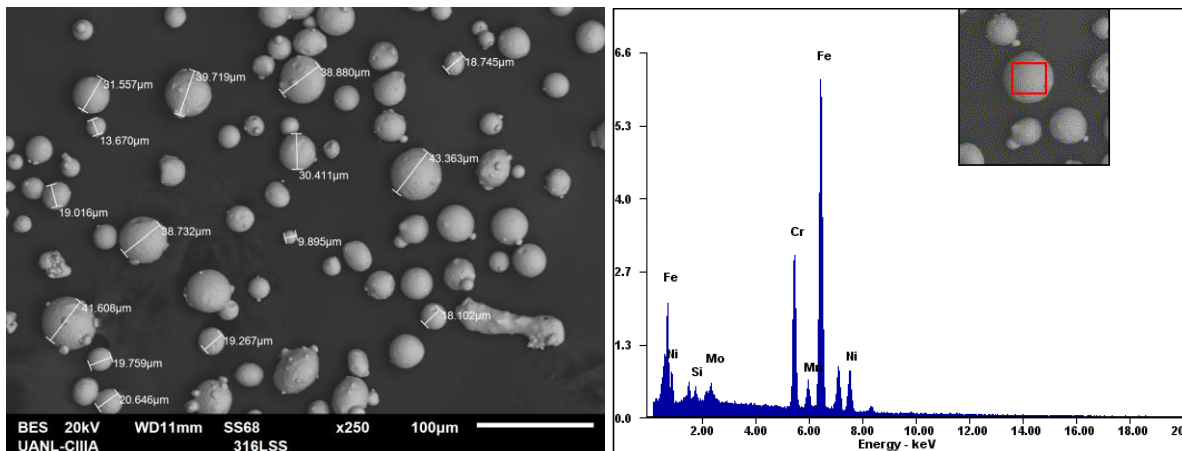


Fig. 3.6 SEM image of the 316L SS metal powder obtained by this research work showing the size of some powder particles (left side) and an EDS analysis in one of those particles (right side).

As Fig. 3.6 shows, measurements in some powder particles were performed in order to verify the particle size supplied by the manufacturer (LPW Technology) together with an EDS analysis on one

of those particles, showing its elemental composition with the major alloying elements and having a similar variation with respect to the chemical composition of the powder presented in Table 3.4, i.e., the Cr and Mo are also incremented in values of 18.20 and 2.85 wt. %, respectively. As for the particle size, measurements in some powder particles were performed as shown in Fig. 3.6, taking an average of 10 particles in three different zones of the SEM image.

Table 3.4 Elemental composition (wt. %) of the 316L SS metallic powder and SLM sample.

Element	C	Cr	Cu	Mn	Mo	Ni	P	S	Si	Fe
Powder	0.03	17.5-18.0	0.50	2.0	2.25-2.50	12.5-13	0.025	0.01	0.75	Bal.
SLM sample	-	18.67	0.04	1.13	2.55	11.84	-	-	-	Bal.

Note in Table 3.4 that the values of the chemical composition of the powder and the SLM-prepared sample do not agree very well. This could be because it could have generated certain agent contaminants inside the Ar atmosphere, that consequently are able to demote the chemical structure of the SLM material. It was observed that the SLM process studied in this research kept working with the oxygen levels up to 1% for certain periods of time, which means that a small loss of Ar gas existed during the laser process. Although the most logical is that the amount of Cr and Mo would have been in lower values, this does not occur in that way. Thus, important attention must be taken into account when the 316L SS alloy is processed by SLM and it is recommended that the oxygen levels inside the Ar atmosphere be completely less to 0.01% in order to not generate certain contamination issues in the material.

In order to summarize the processing parameters used to produce the 316L SS samples, Table 3.5 shows the corresponding values. The description of ambient temperature and laser energy absorptivity is similar to the AISi10Mg alloy, where the 316L SS alloy has an absorptivity coefficient of 0.35.

Table 3.5 SLM processing parameters for the 316L SS alloy.

Parameter	Value
Ambient temperature, T_a (K)	298
Powder layer thickness, t (μm)	30

Laser diameter, D (μm)	70
Hatch spacing, HS (μm)	110
Laser power, P (W)	400
Scanning speed, v (mm/s)	230

3.5 Experimental melt pool morphology of SLM 316L SS alloy

For the observation of the melt pool morphology of SLM 316L SS, it was conducted to the metallographic procedure of the samples. Firstly, the samples were cross sectioned for mounting and polishing. In this case, the samples were cross sectioned into two parts, selecting a cutting plane parallel to the build direction and at the half of the part, as shown in Fig. 3.7. The experimental observation was performed in the XZ plane since the melt pool cross-section is found in this plane or the YZ. Secondly, the mounted and polished samples were prepared to be etched with Glyceregia (15 ml HCL, 10 ml Glycerol, and 5 ml HNO₃). Thirdly, a Zeiss axiobserver.Z1m optical microscope was used to observe the melt pool shape. An average of 65 melt pool measurements were obtained in each micrograph at different positions and a general average of melt pool size is determined between all the samples.

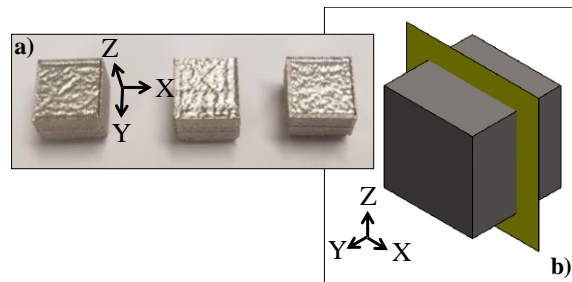


Fig. 3.7 SLM 316L SS parts and b) cutting plane used as reference to obtain the cross-section of the sample.

At the same time, the grain morphology of the 316L SS alloy is also obtained. Fig. 3.8 displays the resulting grain structure of SLM 316L SS, which shows how irregular grains tend to grow up from the fusion line to the center of the melt pool, i.e., across hundreds or thousands of layers [31]. This is because of the thermal gradients produced by the laser melting process, which are higher at the melt pool center than along the fusion line. The grain structure is characterized by martensite with a dark brown tone, pointed out with the yellow arrow, whereas austenite is shown with a clearer brown tone and pointed out with the blue arrow. Nevertheless, a gas-induced spherical defect seems to be present in the microstructure. According to Xiong et al. [46], the circular shape of that defect

allows deducing that it could be formed by a gas-induced from the liquid metal during the rapid solidification process.

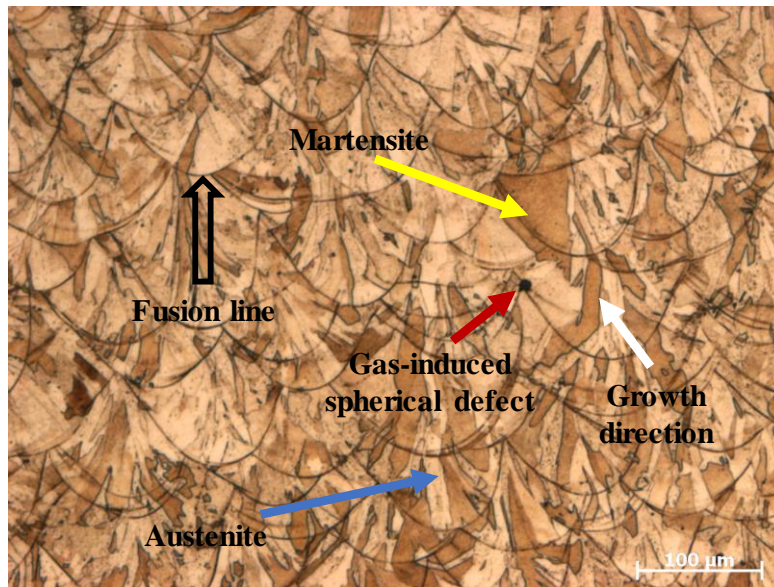


Fig. 3.8 Optical micrograph showing the SLM 316L SS microstructure, parallel to the build direction. The growth direction is designated with the white arrow while the fusion line is shown with the open arrow.

3.6 Summary

Two experimental methodologies for the manufacturing of SLM materials are presented in this section. The characterization of the melt pool dimensions is performed based on the microstructure of each material. It has been obtained experimental data of melt pool width and depth for two SLM metallic alloys. Thanks to the experimental data, numerical models for the prediction of the melt pool can be validated.

4 Numerical Model Development

In this section, it is presented the development of a numerical model of the SLM process based on the lattice Boltzmann method (LBM). The model, still in 2D, simulates the interaction of the laser with the medium, melt pool generation, and predicts thermal dynamic behavior during the heat conduction of the process. For now, physical phenomena such as the Marangoni effect, capillary forces, wetting, and heat losses caused by radiation are not considered within the model. It is important to mention that the present model uses the standard D2Q9 lattice structure to treat the SLM problem like a collection of cells with energy density. This method is so powerful since it can solve the heat conduction equation of SLM into two simple steps; streaming and collision.

4.1 Thermal history modelling for SLM

Complex processes are governed by a great number of partial differential equations that describe the transfer equations for heat, mass, and momentum. In the SLM process, the equation that governs the spatial and temporal temperature evolution is given by [2, 12]

$$k_{xx} \frac{\partial^2 T}{\partial x^2} + k_{yy} \frac{\partial^2 T}{\partial y^2} + k_{zz} \frac{\partial^2 T}{\partial z^2} + \ddot{\phi} = \rho C_p \frac{\partial T}{\partial t} \quad (4.1)$$

In that equation, ρ and C_p represent the density and specific heat capacity of the material, respectively. T is the temperature, t is the time, x , y , and z are the spatial coordinates, k_{xx} , k_{yy} , and k_{zz} are the thermal conductivities, and $\ddot{\phi}$ is the term used to represent the heat source (laser), which can be expressed as one of those Gaussian approximations found in the literature as below [2]

$$\ddot{\phi} = 0.864A \frac{P}{\pi r^2} \quad (4.2)$$

According to the Gaussian equation, the variable P represents one of the most important processing parameters, in this case, the laser power. At the same time, r is the laser radius and A is a property of the material known as laser energy absorptivity, which has been described in the previous chapter as the useful laser energy amount absorbed by the powder, being different for various metallic materials [42]. In fact, the absorptivity coefficient for the AlSi10Mg and 316L SS alloy has been calculated in 0.09 [45] and 0.35, respectively.

For the computation of the temperature field, it must be established an initial condition in the simulation domain. Such condition represents the preheated temperature of the real system, i.e., the initial temperature in the powder bed at time $t = 0$ (before starting the SLM process), which is represented by

$$T(x, y, z, t)|_{t=0} = T_0 \quad (4.3)$$

Thus, in order to solve Eq. 4.1, a computational domain needs to be formulated. Fig. 4.1 depicts a simulation domain to research on SLM process. In this model, the laser beam is considered as an input energy density that interacts with the properties of the medium (powder bed). The right and left side, as well as the bottom side, is maintained at constant temperature T_{wall} , being also the preheated temperature of the substrate in the real system.

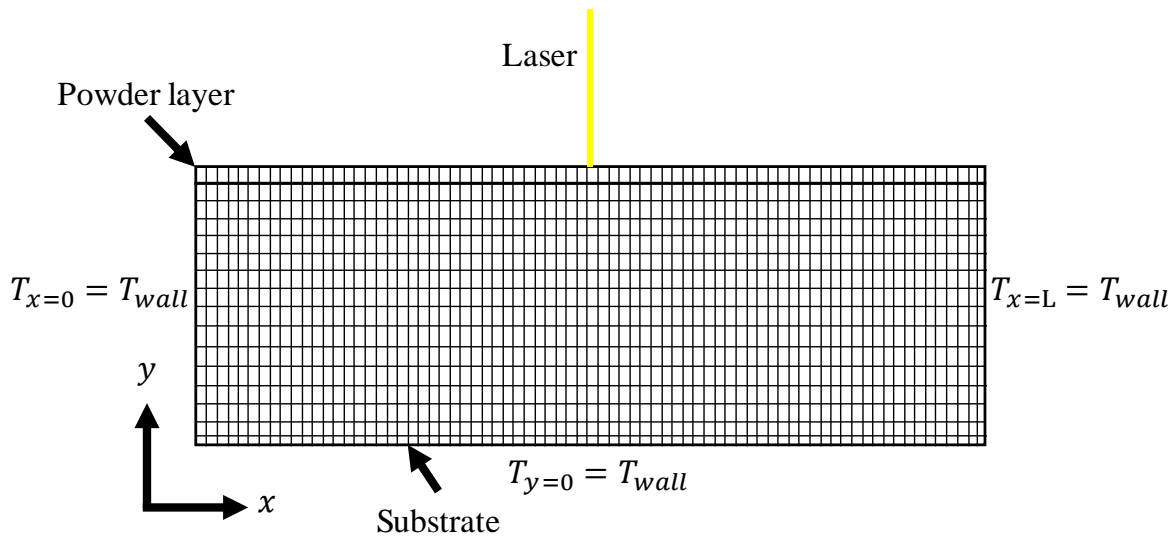


Fig. 4.1 Representation of the SLM domain to research on SLM process.

In this way, the knowledge of the temperature distribution is calculated by a computational domain divided into a certain number of discrete nodes, elements, or volumes. This approach is called continuum medium since the partial differential equations applied in each node, element, or volume are solved via energy, mass, and momentum conservation equations. The most important approaches that have been used to investigate and optimize the SLM process are FDM, FVM, and

FEM [2, 13]. It is worthy to mention that these methods consume a considerable simulation time, depending of the size mesh selected for the solution.

On the other extreme, there exist other approaches known as explicit methods used to simulate the SLM process. In this case, the LBM is an attractive method, which considers the medium as a tidy set of small particles with energy density, in the case of thermal diffusion, to stream and collide in their neighborhoods. In the following sections, it is shown how LBM has been implemented to simulate the SLM process.

4.2 Lattice Boltzmann method for SLM process

A few years ago, the LBM, considered as a powerful tool, has gained a lot of attention by scientific and engineering communities since it is able to solve real engineering problems. Using the LBM, several heat transfer problems have been successfully solved [47].

The discretized lattice Boltzmann equation (particle distribution functions f_k) for the description of the temperature evolution of a given system subjected to thermal diffusion is defined by Eq. 4.4 [48–50]. That equation is characterized by a process known as advection (streaming) represented by the right-hand side of the equation and a collision process or source term defined by the left-hand side term.

$$f_k(r + c_i \Delta t, t + \Delta t) = f_k(r, t) + \frac{\Delta t}{\tau} [f_k^{eq}(r, t) - f_k(r, t)] \quad (4.4)$$

$$k = 1, 2, \dots, d$$

Eq. 4.4 is the equivalent form of the energy equation of SLM (Eq. 4.1 without heat generation) in the LBM formulation, where f_k is the particle distribution function, c_i is the microscopic velocity, τ is the relaxation time, and f_k^{eq} is the equilibrium distribution function known as Maxwell-Boltzmann distribution function. In order to solve this equation, a standard D2Q9 lattice structure [51–54] is implemented. The relaxation time τ in the equation is assumed as a known parameter, which is used to calculate an important lattice Boltzmann parameter known as collision frequency ω [48] or vice versa, it can be defined the collision frequency as a known parameter and subsequently calculate the corresponding relaxation time.

$$\omega = \frac{\Delta t}{\tau} \quad (4.5)$$

According to the literature [55], the factor ω has to range strictly between 0 and 2. For LBM, this condition ensures stability during the solution of the problem. Therefore, the relaxation time must be chosen properly. On the other hand, in order to know about the diffusion coefficient in LBM for the solution of the problem, there is a relationship between ω and the LBM diffusivity α , which is defined as [55]

$$\alpha = c_s^2 \left(\frac{1}{\omega} - \frac{1}{2} \right) \quad (4.6)$$

where c_s is a parameter called sound speed in the LBM formulation and has generally a value of $1/\sqrt{3}$ [50]. Once the LBM diffusivity is calculated, this one is related to a number known as Fourier number in order to calculate the number of time steps for the simulation. Fourier number considers the real physical properties of the medium, i.e., the thermophysical properties of the powder bed of the SLM process. This relation is defined by a given number of time steps t_{LBM} , mesh size N , real time t , and the real dimension of the medium L (domain length). Thus, the Fourier number is given by [55–58]

$$F_o = \frac{\alpha t_{LBM}}{N^2} = \frac{\alpha_P t}{L^2} \quad (4.7)$$

In the above equation, α_P is the thermal diffusivity of the real medium, i.e., the thermal diffusivity of the material in its powder or solid phase.

4.3 The D2Q9 lattice structure

The solution of Eq. 4.4 is performed by two steps known as collision and streaming, which take place within a D2Q9 lattice structure [51–54]. Using several lattice structures of D2Q9, it is possible to form a tidy simulation model in which the information (temperature) streams (move) along given directions to their neighborhoods. Fig. 4.2 represents a set of D2Q9 lattice structures showing how the LBM domain is integrated.

The D2Q9 lattice structure assumes that the problem is treated in two dimensions where the information (mass, momentum, temperature, etc.) is propagated along 9 given velocities vectors where the velocity of f_1 at the cell center is zero. Therefore, such as velocities are defined as $c(0,0)$, $c(1,0)$, $c(0,1)$, $c(-1,0)$, $c(0,-1)$, $c(1,1)$, $c(-1,1)$, $c(-1,-1)$ and $c(1,-1)$ for f_1 , f_2 , f_3 , f_4 , f_5 , f_6 , f_7 , f_8 and f_9 , respectively. The weighting factors applied for each distribution function are $4/9$, $1/9$, $1/9$, $1/9$, $1/9$, $1/36$, $1/36$, $1/36$, and $1/36$, respectively [59, 60].

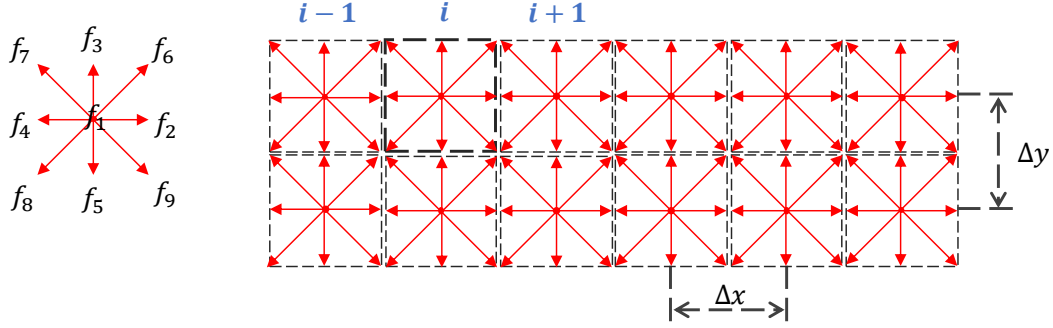


Fig. 4.2 D2Q9 lattice structure used to discretize the solution domain.

In order to compute the dependent variable, this one is related to the distribution functions f_k as [52, 58, 61–63]

$$T(x, y, t) = \sum_{k=1}^9 f_k(x, y, t) \quad (4.8)$$

Additionally, the equilibrium distribution function f_k^{eq} in Eq. 4.4 is calculated as [52, 58, 61, 64, 65]

$$f_k^{eq} = w_k T(x, y, t) \quad (4.9)$$

Here, w_k stands for the weighting factors in the direction k and must satisfy the following criterion

$$\sum_{k=1}^9 w_k = 1 \quad (4.10)$$

The equilibrium distribution function $f_k^{eq}(x, y, t)$ defined in Eq. 4.9 is also used to calculate the temperature distribution and can be expressed as follows

$$\sum_{k=1}^9 f_k^{eq}(x, y, t) = \sum_{k=1}^9 w_k T(x, y, t) = T(x, y, t) \quad (4.11)$$

4.4 Solution procedure

As mentioned previously, the solution of the distribution function is performed by two steps, collision and streaming. Thus, in order to implement a programming code with a certain grade of simplicity, a standard numbering of links like in several investigations [48–50] must be properly defined, as shown in Fig. 4.3.

For the simulation process using LBM, the collision step is given by

$$\begin{aligned} f_k(x, y, t + \Delta t) &= f_k(x, y, t)[1 - \omega] + \omega f_k^{eq}(x, y, t) \\ k &= 1, \dots, 9 \end{aligned} \quad (4.12)$$

while the streaming step as

$$\begin{aligned} f_k(x + \Delta x, y + \Delta y, t + \Delta t) &= f_k(x, y, t + \Delta t) \\ k &= 1, \dots, 9 \end{aligned} \quad (4.13)$$

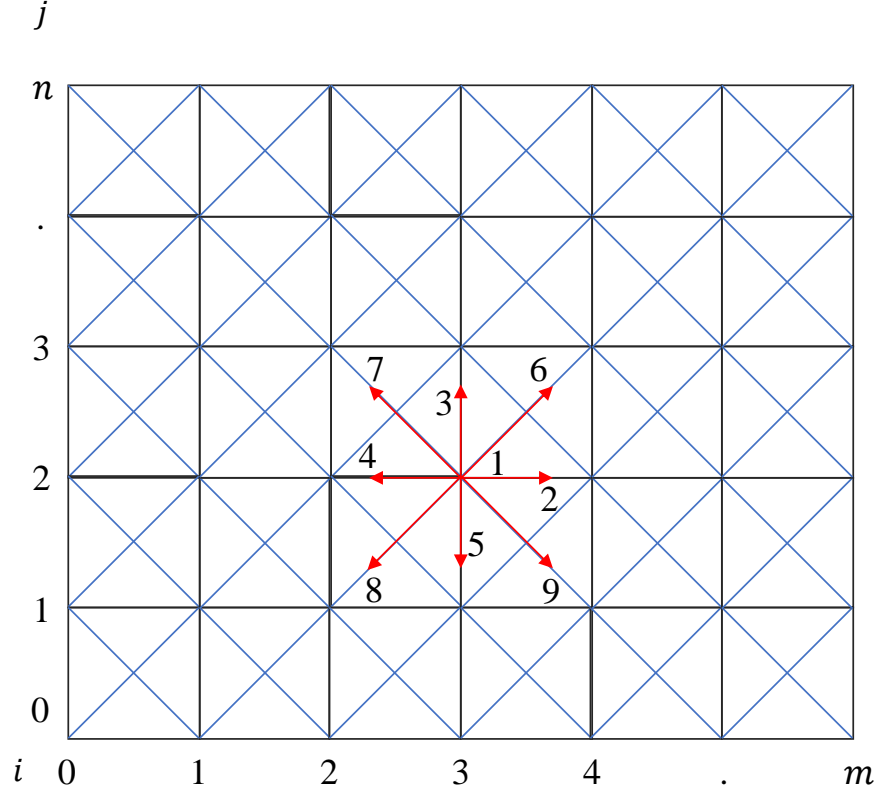


Fig. 4.3 D2Q9 lattice structure with the numbering of links for the simulation process [48].

The propagation of information takes place when the distribution functions move to their corresponding neighborhoods. In this case, $f_2(i, j)$ moves to $f_2(i + 1, j)$, $f_3(i, j)$ moves to $f_3(i, j + 1)$, $f_4(i, j)$ moves to $f_4(i - 1, j)$, $f_5(i, j)$ moves to $f_5(i, j - 1)$, $f_6(i, j)$ moves to $f_6(i + 1, j + 1)$, $f_7(i, j)$ moves to $f_7(i - 1, j + 1)$, $f_8(i, j)$ moves to $f_8(i - 1, j - 1)$, and $f_9(i, j)$ moves to $f_9(i + 1, j - 1)$. For the case of $f_1(i, j)$, this one is the particle distribution function at the center of each cell, which does not move to its neighboring node. In order to not accumulate a great amount of simulated data during the simulation process, the streaming process must be performed in a manner that only the new values cannot be overridden.

The values of the weighting factors [58, 60] have been previously mentioned, but according to the numeration of each distribution function, these ones can be specifically rewritten as follow

$$\begin{cases} w_1 = 4/9 \\ w_2 = w_3 = w_4 = w_5 = 1/9 \\ w_6 = w_7 = w_8 = w_9 = 1/36 \end{cases} \quad (4.14)$$

In the case of the velocity vectors [58, 60] along the propagation lines, these ones are generally given as $c_1(0,0)$, $c_2(c,0)$, $c_3(0,c)$, $c_4(-c,0)$, $c_5(0,-c)$, $c_6(c,c)$, $c_7(-c,c)$, $c_8(-c,-c)$ and $c_9(c,-c)$ where $c = \Delta x/\Delta t$.

The initial condition for the LBM domain is expressed by

$$f_k(x, y, 0) = w_k T_0(x, y, 0) \quad (4.15)$$

The equilibrium distribution function can be calculated using Eq. 4.9 where $T(x, y)$ is defined as follows

$$T(x, y, t) = \sum_{k=1}^9 f_k(x, y, t) \quad (4.16)$$

In LBM, it is very common to use $\Delta x = \Delta y = 1$ and $\Delta t = 1$, therefore the numerical model of this investigation uses the same value of unity for the discretization of the space-time domain.

4.5 Boundary Conditions in the LBM for the SLM process

4.5.1 Dirichlet boundary condition

For the numerical modeling by the LBM, it is of essential significance the conversion of a macroscopic boundary condition into that of a microscopic distribution function since LBM deals with distribution functions. The model is considered by a 2D rectangular lattice where the left, right, and bottom sides are maintained at constant temperature. This temperature refers to the preheated temperature of the substrate at the beginning of the process. Fig. 4.4 depicts the boundary condition (boundary wall) of constant temperature, known as Dirichlet boundary condition, that is applied to the three corresponding sides.

At the same time, the definition of constant temperature boundary condition allows calculating the distribution functions that are not calculated during the streaming process. In this case, it is necessary to establish certain conditions at the positions $x = 0$, $x = L$, and $y = 0$, which correspond to the left, right, and bottom sides of the rectangular domain, respectively, in order to calculate all the distribution functions.

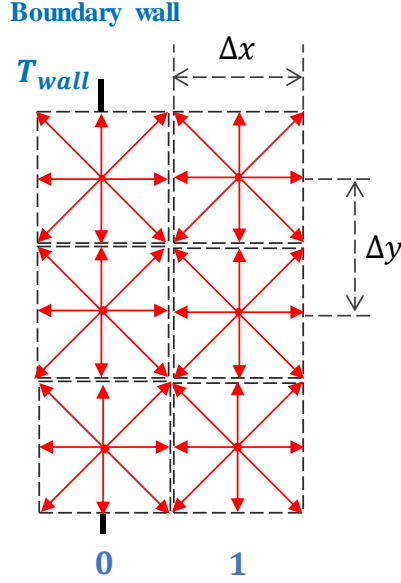


Fig. 4.4 BC for the left side of constant temperature.

At the position $x = 0$, f_2 , f_6 , and f_9 are unknown because they only move (streaming process) to the right side. Therefore, a way to calculate f_2 , f_6 , and f_9 is using the distribution functions f_4 , f_7 , and f_8 due to these ones move to the left side, are known, and must satisfy the following expressions

$$\begin{cases} f_2(0,j) + f_4(0,j) = w_2 T_{wall} + w_4 T_{wall} \\ f_6(0,j) + f_8(0,j) = w_6 T_{wall} + w_8 T_{wall} \\ f_9(0,j) + f_7(0,j) = w_9 T_{wall} + w_7 T_{wall} \end{cases} \quad (4.17)$$

In a similar way, the right side ($x = L$) also maintains the same condition. Thus, the equations to calculate the unknown corresponding distribution functions ($f_4(L,j)$, $f_7(L,j)$, and $f_8(L,j)$) at the right side are

$$\begin{cases} f_4(L,j) + f_2(L,j) = w_4 T_{wall} + w_2 T_{wall} \\ f_7(L,j) + f_9(L,j) = w_7 T_{wall} + w_9 T_{wall} \\ f_8(L,j) + f_6(L,j) = w_8 T_{wall} + w_6 T_{wall} \end{cases} \quad (4.18)$$

Accordingly, the bottom side ($y = 0$) is also under the same boundary condition (T_{wall}). Then, the expressions to calculate the unknown distribution functions at the bottom side can be expressed as follows

$$\begin{cases} f_3(i, 0) + f_5(i, 0) = w_3 T_{wall} + w_5 T_{wall} \\ f_6(i, 0) + f_8(i, 0) = w_6 T_{wall} + w_8 T_{wall} \\ f_7(i, 0) + f_9(i, 0) = w_7 T_{wall} + w_9 T_{wall} \end{cases} \quad (4.19)$$

4.5.2 Convective boundary condition

Robin boundary condition is established when a system interacts with an environment of known temperature. For SLM, the process takes place inside an Argon-filled chamber, which is at a room temperature with a known convection heat transfer coefficient. The boundary condition in the convective contact zone, as shown in Fig. 4.5, considering the heat conduction between the nodes, and related with the energy conservation equation for unsteady-state heat transfer, gives as

$$q_{(i,n) \rightarrow (i,n-1)} - h\Delta y(T(i, n) - T_a) = \rho C_p V_0 \frac{\partial T}{\partial t} \quad (4.20)$$

where ρ and C_p represent the density and specific heat capacity of the corresponding medium, respectively. Since SLM is performed inside a controlled ambient chamber, this one has a known convective heat transfer coefficient h and an ambient temperature T_a . The value of V_0 is equal to $\Delta x \Delta y$ and represents the volume of one cell in the grid. The heat flux term in Eq. 4.20, $q_{(i,n) \rightarrow (i,n-1)}$, is the heat conduction term between the corresponding nodes and can be expressed as follows

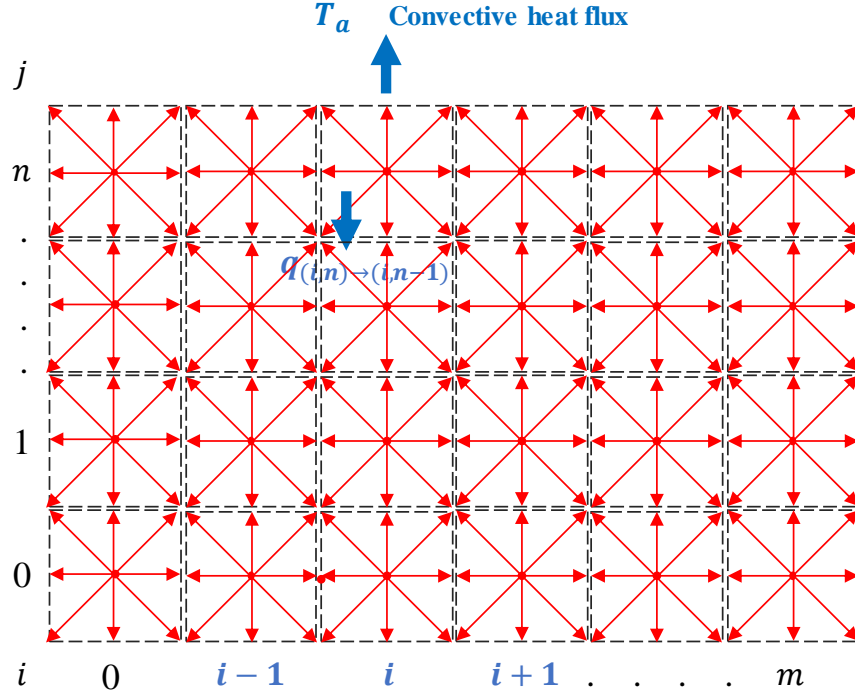


Fig. 4.5 BC within the convective contact zone.

$$q_{(i,n) \rightarrow (i,n-1)} = -k\Delta x \left[\frac{T(i,n) - T(i,n-1)}{\Delta y} \right] \quad (4.21)$$

The value of k is given by the thermal conductivity of the real system (powder bed).

Note that equations 4.20 and 4.21 are equations used for FDM. By substituting Eq. 4.21 into Eq. 4.20, the resultant equation will be

$$-k\Delta x \left[\frac{T(i,n) - T(i,n-1)}{\Delta y} \right] - h\Delta y(T(i,n) - T_a) = \rho C_p V_0 \frac{(T^{t+\Delta t}(i,n) - T(i,n))}{dt} \quad (4.22)$$

where the corresponding values for $T(i,n)$, $T(i,n-1)$, and $T^{t+\Delta t}(i,n)$ in LB formulation are assumed as

$$T(i,n) = \frac{f_3(i,n) + f_5(i,n)}{w_3 + w_5} \quad (4.23)$$

$$T(i, n - 1) = \frac{f_3(i, n - 1) + f_5(i, n - 1)}{w_3 + w_5} \quad (4.24)$$

$$T^{t+\Delta t}(i, n) = \frac{f_3(i, n) + f_5(i, n)}{w_3 + w_5} \quad (4.25)$$

It is important to be careful in Eq. 4.25 due to is similar to equation 4.23 where the distribution function $f_3(i, n)$ at the new time level $t + \Delta t$ is obtained from the streaming process and $f_5(i, n)$ is the distribution function that needs to be determined also at the new time level. The distribution functions in Eq. 4.23 and 4.24 are known from the previous time step t . Therefore, by substituting Eq. 4.23, 4.24, and 4.25 into Eq. 4.22 and solving for the unknown distribution function $f_5(i, n)$ of the new time step, the resultant equation will be

$$\begin{aligned} f_5(i, n) = & \left(\frac{\alpha \Delta t}{(\Delta x)^2} \right) (f_3(i, n - 1) + f_5(i, n - 1)) + \left(1 - \frac{\alpha \Delta t}{(\Delta x)^2} \right) (f_3(i, n) + f_5(i, n)) \\ & - f_3(i, n) + \left(\frac{\alpha \Delta t}{(\Delta x)^2} \right) \left(\frac{h \Delta y}{k} \right) (w_3 T_a + w_5 T_a - f_3(i, n) - f_5(i, n)) \end{aligned} \quad (4.26)$$

where α is the thermal diffusivity of the real system defined as $\alpha = k/\rho C_p$. In this way, the unknown distribution function f_5 at the new time level is related to the energy conservation equation applied in the convective contact zone due to f_5 cannot be obtained by the streaming process. The distribution function f_3 and f_5 in the right side of the equation correspond to the distribution functions calculated in the previous time step as well as the corresponding distribution function f_3 obtained by the streaming process but in the current iteration level.

4.5.3 Heat flux boundary condition

This boundary condition takes place when the laser impacts the simulation domain. In the laser-material contact zone, the energy of the laser is in contact with the material (2D simulation domain), giving, as a result, an increase in the material temperature. Thus, considering the laser energy density to melt the material and the heat conduction between the corresponding nodes, Fig. 4.6, the conservation energy equation for unsteady-state heat transfer is given as

$$q_{(i,n) \rightarrow (i,n-1)} + q''A = \rho C_p V_0 \frac{\partial T}{\partial t} \quad (4.27)$$

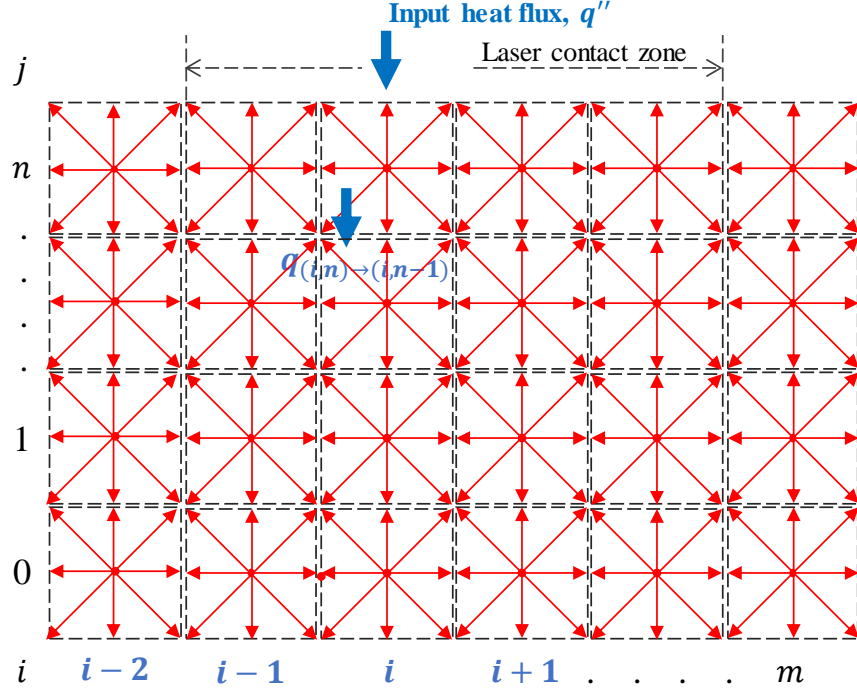


Fig. 4.6 BC within the laser contact zone.

where q'' is the input heat source (laser power) and A is the normal area on which the laser irradiates the material. As the laser approaches the simulation domain in a normal direction, Eq. 4.27 can be related to the distribution function in the same direction, i.e., to the unknown distribution function f_5 . The area and volume in the energy conservation equation are $A = \Delta x$ and $V_0 = \Delta x \Delta y$, respectively. On another hand, the laser energy density is deposited per unit time step Δt , where the number of time steps is calculated accordingly to the laser exposure time (Eq. 4.7).

4.6 Material properties and LBM parameters for the simulations

As mentioned previously, LBM works with particle distribution functions that move along given directions in a lattice structure and collide to exchange their energy. The good working of this process is given by the correct selection of the LBM parameters from the physical properties of the material to be simulated. In this investigation, the first LBM model to represent the SLM process is developed using an Aluminum alloy (AlSi10Mg). The physical properties of this alloy are shown in

Table 4.1. It is worthy to mention that the AlSi10Mg simulation considers the simulated material in its solid phase and keeps constant physical properties. For future investigations, the LBM can be enhanced by taking into account the transformations of the material during the laser melting process, i.e., the powder, liquid, and solid phase, as it has been studied in [2] by FEM.

Table 4.1 Physical properties in solid phase for the AlSi10Mg alloy.

Parameter	Value
Density (solid) [35], ρ (kg/m ³)	2650
Thermal conductivity (solid) at 473 K [35], k (W/m K)	159
Specific heat capacity (solid) at 473 K [35] C_p (J/kg K)	797
Solidus temperature [66], T_S (K)	830
Liquidus temperature [66], T_L (K)	869
Absorptivity [35], A	0.09

Using the physical properties of the AlSi10Mg alloy shown in Table 4.1, a set of simulation parameters needs to be defined for solving the heat conduction problem. These parameters are carefully selected and calculated to ensure stable conditions during the simulation process. Table 4.2 shows the simulation parameters for the LBM and the FDM and FEM. The continuum methods are used as comparative methods.

The selection of the LBM parameters starts by choosing the dimensions of the lattice structure, i.e., how many cells will the simulation domain have? in this case, the LBM parameters L and H. Then, if we divide the real dimension L or H by the number of cells in the same direction (for example 1×10^{-3} m/100 or 0.5×10^{-3} m/50), it has that one cell is 10 μ m, which is the value of Δx and Δy for the FDM and FEM, although in LBM Δx , or Δy is equal to the unity. In the next step, the relaxation time must be chosen properly since it is then used to calculate the diffusion coefficient in LBM using Eq. 4.6. Accordingly, the number of time steps for the LBM simulation is calculated by Eq. 4.7. Due to Fourier number relates the physical properties of the real system with the LBM parameters, the number of time steps is not so complicated to calculate. The LBM time or the number of time steps for the simulation is strictly related to the relaxation time, thus the correct selection of that parameter can help considerably.

Table 4.2 Simulation parameters for AlSi10Mg.

Parameter	FDM/FEM	LBM
Δx	1×10^{-5} m	1
Δy	1×10^{-5} m	1
Δt	2×10^{-7} s	1
Domain length, L	1×10^{-3} m	100
Domain height, H	0.5×10^{-3} m	50
Spot diameter, D	7×10^{-5} m	7
Spot irradiation time, SIT	1×10^{-4} s	456
Thermal diffusivity	7.53×10^{-5} m ² /s	0.165
Fourier number, F_0	0.0075	0.0075
Relaxation time, τ	-	0.995
Collision frequency, ω	-	1.005

As Table 4.2 shows, the 2D simulation domain used to represent the material that is melted by the laser beam is of length $L = 1 \times 10^{-3}$ m and height of $H = 0.5 \times 10^{-3}$ m. Such computational domain is discretized by the selected number of nodes and lattices for the FDM/FEM and LBM, respectively. The simulation domain is able to consider the effect of convection-diffusion on the laser melting processes for all the numerical models developed in this work. The processing parameters (laser powder, laser irradiation time, ambient temperature, etc.) are considered the same as in the experimental methodology. For now, all the simulations take only one spot, which is applied at the position $(x, y) = (L/2, H)$. The ambient and initial temperature for the simulation of SLM AlSi10Mg is $T_a = 25$ °C and $T_o = 200$ °C, respectively. The initial temperature is assumed as the preheating temperature of the material before the laser starts impacting the material.

In a similar way, the physical properties and simulation parameters for the 316L SS alloy are carefully defined and calculated as Table 4.3 and 4.4 show. For this case, the initial temperature of the simulation domain is $T_o = 300$ °C due to the 316L SS thermophysical properties were investigated at the mentioned temperature. The convective heat transfer coefficient is $h = 20$ W/m² K for all the performed simulations.

Table 4.3 Physical properties in solid phase for the 316L SS alloy.

Parameter	Value
Density (solid) [67], ρ (kg/m ³)	7980
Thermal conductivity (solid) at 573 K [67] k (W/m K)	18
Specific heat capacity (solid) at 573 K [67] C_p (J/kg K)	545
Solidus temperature [68], T_S (K)	1658
Liquidus temperature [68], T_L (K)	1723
Absorptivity [68], A	0.35

Table 4.4 Simulation parameters for 316L SS.

Parameter	FDM/FEM	LBM
Δx	1×10^{-5} m	1
Δy	1×10^{-5} m	1
Δt	2×10^{-6} s	1
Domain length, L	1×10^{-3} m	100
Domain height, H	0.5×10^{-3} m	50
Spot diameter, D	7×10^{-5} m	7
Spot irradiation time, SIT	8×10^{-5} s	20
Thermal diffusivity	4.14×10^{-5} m ² /s	0.165
Fourier number, F_0	0.00033	0.00033
Relaxation time, τ	-	0.995
Collision frequency, ω	-	1.005

4.7 Comparison between LBM and FEM

As far as we know, SLM is a complex process due to the strong fluid flow dynamics involved by the laser beam movement. Based on the literature [69], these processes with high complexities of fluid flow like SLM are more difficult to be studied by conventional macroscopic approaches like FEM. Thus, since the SLM process involve certain phenomena like micro scale flow, phase transformations, and effects of convection-diffusion, these ones are easier to be simulated by mesoscopic approaches like LBM rather than FEM.

On the other hand, the main reason of using LBM against FEM is that the governing convection-diffusion equation of SLM can be solved using the mentioned process of diffusion and collision of fictitious particles on a regular lattice [69]. Thanks to LBM uses two simple steps, it can be prevented a great number of algebraic equations which consume a significant memory space. In LBM, it can be established that only the desired data be saved, using just the required computational space for the results. In the results section, it is shown a comparison of the elapsed time to solve the heat conduction equation between LBM and FEM.

4.8 Summary

The development of a 2D LBM for the SLM process is established by considering the physics of the phenomenon (laser interaction with the material). It is observed the implementation of the standard D2Q9 lattice structure in the simulation domain. The boundary conditions are established by taking into account the processing parameters as well as the characteristics of the medium. Finally, the simulation parameters are calculated according to the respective equations and the physical properties of the material to be simulated.

5 Corrosion resistance measurement of 316L stainless steel manufactured by selective laser melting

The aim of this Chapter is to show the importance of the corrosion resistance measurement of a metallic material (316L SS) manufactured by selective laser melting. In particular, the study of the relationship between the surface features and corrosion behavior. Therefore, the corrosion resistance of the SLM 316L SS was measured by linear polarization resistance (LPR) and electrochemical noise (EN) techniques under three different environments and analyzing the horizontal (XY) and vertical (XZ) planes of the samples. It is worthy to mention that the final corrosion properties are highly influenced by the manufacturing process.

5.1 Corrosion studies on SLM 316L SS

The corrosion resistance of a metallic material is one of the most important properties of end-use engineering parts when these ones interact with aggressive environments. Even more when it treats of final components for the aeronautical, automotive, food processing, marine, chemical and petrochemical, and medical industries. Therefore, here is when the electrochemical response of SLM 316L SS parts needs to be determined.

Kong et al. [70] emphasized that the SLM defects like melt pool boundaries, non-equilibrium phases, etc. are some of the main factors that decrease the corrosion resistance of an additively manufactured 316L SS compared with those of traditionally manufactured 316L SS. Nie et al. [71] established that the chemical composition of the passive film formed in an AM 316L SS plays an important role in its corrosion resistance. A minor content of hydroxide in the film combined with a micro-galvanic corrosion effect at the interface of the sub-grain boundaries and sub-grains reduce the potential to repair such passive film, leading to the development of pitting corrosion. In Zhou et al.'s [72] study, it was found that the melt pool boundaries of an SLM 316L SS considerably lead to pitting-corrosion attacks, but it can be significantly prevented by applying recrystallization post-processes which help to disappear the fusion lines produced by the laser process.

Another important study was recently made by Duan et al. [73] who studied that the SLM 316L SS alloy tested in aggressive solutions (1 M NaCl, pH 1 and 3 M NaCl, pH 3) exhibits pitting corrosion at the gas pores induced by the melting process. On the other extreme, in a similar background, the physical properties of the SLM parts also mainly depend on the microstructure orientation and the

surface texture. For instance, the mechanical properties of an SLM material are better in the horizontal direction than in the vertical one [17]. According to Serafin et al. [74], the surface roughness of an SLM material also plays an important role, i.e., the corrosion resistance is better in an SLM surface after polishing than for one unpolished. This is related to a minimum number of cavities, defects, etc. on a polished surface, preventing the development of localized corrosion. Based on this, Geenen et al. [75] also studied that the SLMed 316L SS does not show good electrochemical properties compared to specimens processed by casting, hot isostatic pressing (HIP), and SLM + HIP due to the inhomogeneities caused by the nature of the manufacturing process, reducing the corrosion resistance of the material. In addition to these important findings, the amount of chromium on the surface of a 316L SS alloy influences its corrosion behavior, the obtention of chromium-enriched oxides considerably enhances the corrosion resistance [76].

Improving the corrosion resistance directly by the modification of the SLM processing parameters has proven to be a difficult task, so researchers have been looking at other methods. Heat treatment is the most frequent approach found in literature, in which the SLMed 316L SS components are submitted into a recrystallization post-process, in which dislocations in the grain boundaries disappear [70], as well as residual stress is relieved [77]. After the post-process the electrochemical properties are enhanced, in some cases, the corrosion resistance of the SLMed 316L SS component might be better than a wrought component [73, 78]. Reducing the porosity of SLMed components by heat treatment is of great importance since pores are the principal reason for the reduction of electrochemical and mechanical properties of an AM component. Trelewicz et al. [79] found a relationship between porosity and corrosion in AM alloys, in which crevice corrosion is mainly caused in the pores of the material. Likewise, Sun et al. [80] concluded that pre-existing pores in the SLMed 316L microstructure cause an increase of the metal dissolution, leading to pitting corrosion at low anodic potentials. On the other side of the spectrum, there are inclusions, cracks, and segregated elements which also affect the corrosion resistance of the SLMed parts. MnS inclusions influence the inhibition of pitting and its propagation over the material [81, 82]. Mo segregation causes a loss of passivity and an increase of anodic current density [79].

In order to characterize the electrochemical characteristics of the SLMed 316L SS alloy, electrochemical and microscopy techniques need to be considered. Harun et al. [83] used the potentiodynamic polarization technique to study the corrosion behavior of the SLMed 316L SS exposed to thermal oxidation (TO) at controlled temperature (37°C) in a Ringer's solution. The thermal oxidation process (TO) was the key to find out different oxide layers (Fe_2O_3 and Cr_2O_3) on

the additively manufactured 316L SS alloy where the oxide layer formed at a time of 150 h with 700 °C showed improved corrosion behavior. Chao et al. [82] performed a corrosion study using the SLMed 316L SS tested by cyclic potentiodynamic polarization technique whereby it was found that the passive range exhibited by the SLMed component is wider than of wrought 316L SS. Herein, the large passive area as good anticorrosive property in steel alloys [75] was correlated to a minimal MnS inclusions amount found from microstructural characterization by scanning and transmission electron microscopy (SEM and TEM). In addition, Kong et al.'s study [70] previously mentioned considered non-destructive corrosion tests to evaluate the electrochemical response of SLMed 316L SS, which was subjected to heat treatment to increase its corrosion resistance. After the recrystallization process, electrochemical results verified an outstanding corrosion behavior, superior to wrought.

On the other extreme, it is also important to investigate the type of corrosion occurring in the SLM material. In fact, the most common corrosion studies of an SLM material focus on the obtention of the corrosion resistance rather than the relation of the surface and microstructure orientation with the type of corrosion occurring into the material for different corrosive environments. For this, electrochemical noise (EN) characterization appears to be a promising technology [84] to provide an understanding of the corrosion behavior produced in a metallic material, which would result difficult to understand by other means. Due to the material experiments fluctuations in potential and current, these ones can be represented by a corrosion map [85] thanks to the EN approach. The amplitude of such fluctuations can define the amount of the dissolved material during the corrosion process. Therefore, the aim of this work is the manufacturing of SLM parts using the 316L SS alloy to study its corrosion behavior using the EN technique and its microstructural features by optical microscopy (OM), scanning electron microscopy (SEM), and energy-dispersive X-ray spectroscopy (EDS) as well as X-ray Fluorescence Spectroscopy (XRF) to analyze the chemical composition of the SLM material. The material is treated on two different surfaces, horizontal and vertical, in order to study how the microstructure direction influences the corrosion behavior.

5.2 Material and experimental methods

5.2.1 Material preparation

Having the verification of the powder (section 3.4) and the manufacturing of 10x10x10mm cubic samples (section 3.5), it was carried out the corresponding cutting of the samples in order to obtain the cross-section of each specimen. In this study, the XY and XZ (Z-axis is parallel to the build

direction) planes of the samples were selected as the testing surfaces to carry out the electrochemical tests and verify how the surface orientation influences the final electromechanical properties. Although Fig. 3.7 in chapter 3 only shows the vertical cutting plane, some samples also were cut in a horizontal direction (XY plane), cutting all the specimens in half.

Then, the as-built samples were grinded and polished according to standard procedures, up to 4000 grits SiC abrasive paper. In accordance with these procedures, different working areas corresponding to the horizontal and vertical cross-section of the sample, normal (XY plane), and parallel (XZ plane) to the build direction, respectively, were obtained. Since it is also obtained the SLMed 316L SS microstructure in this work, some of the polished surfaces were etched using Vilella's reagent (1 gram Picric acid, 5 ml Hydrochloric acid (concentrated), 95 ml Ethyl alcohol) for 6 min to be observed by a Zeiss axiobserver.Z1m optical microscope to show the shape and microstructure of the melt pool (section 3.2).

5.2.2 Microscopic observation of the XY and XZ testing surfaces

In order to observe the initial features of the treated surfaces after the polishing process, a surficial observation using the optical microscope was performed on the horizontal and vertical surfaces. This optical observation was carried out for scanning the possible SLM defects that were developed during the laser process. For this, four magnifications in the optical microscope were taken into account to show a selected area of the testing surface, corresponding to the XY and XZ plane of the material. Fig. 5.1 shows the metallographic images of the two analyzed surfaces, which were labeled with a, b, and c, d, for the horizontal and vertical surfaces, respectively. It can be observed that there exists a little level of porosity such as irregularities, inclusions, irregular and spherical defects. It is worthy to mention that a detailed analysis of the SLM irregularities is also considered in section 6.8. For this, a ZEISS EVO Scanning Electron Microscope (SEM) is used, as well as to analyze and observe the corrosion products after the corresponding measurements, section 6.11.

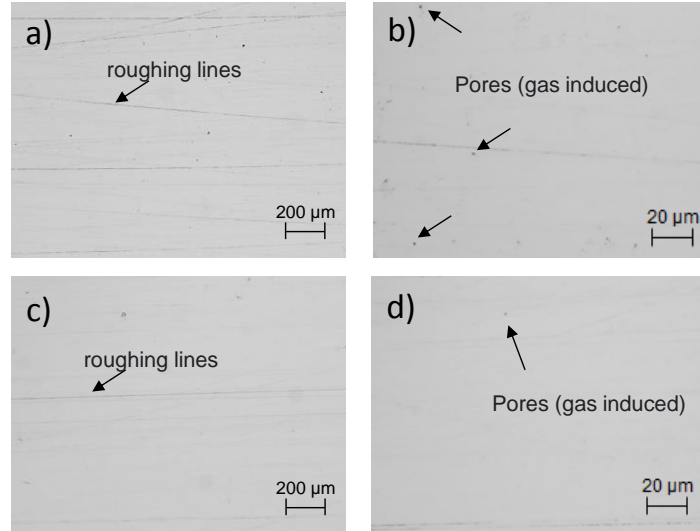


Fig. 5.1 Metallographic images of the SLMed 316L SS horizontal and vertical surfaces showing a little level of porosity. Image, 3a (50x) and 3b (500x) XY plane and 3c (50x) and 3d (500x) XZ plane.

5.2.3 Corrosion testing

The corrosion tests were carried out using a linear polarization resistance (LPR) [86] and electrochemical noise (EN) [87] experimental setup, as shown in Fig. 5.2. A potentiostat / galvanostat (Reference ZRA Gill ACM Instruments) and a three-electrode cell integrate the system, where a saturated calomel electrode (SCE), a platinum mesh, and the SLMed 316L SS sample make up the reference, counter, and work electrode, respectively.

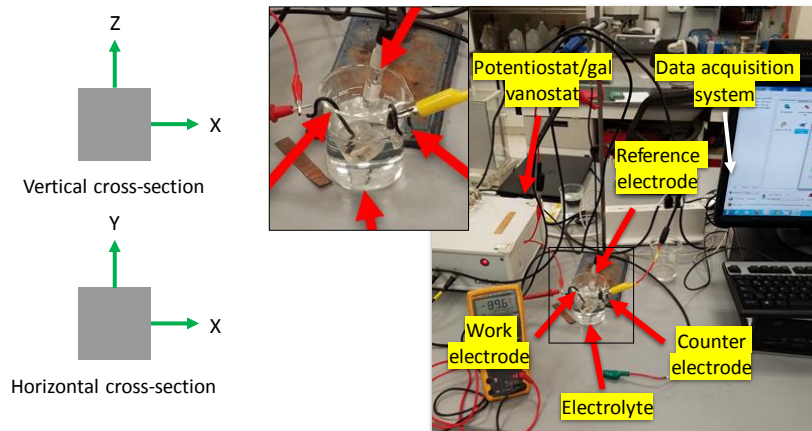


Fig. 5.2 Experimental setup used to perform the corrosion tests; left side, horizontal and vertical cross-section (Z axis is parallel to the build direction) of the work electrodes.

Once the experimental setup was prepared, the SLMed 316L SS polished surface of each sample was exposed and studied into three electrolyte solutions; H₂O, 3.5 wt.% NaCl, and 20% H₂SO₄. The linear polarization resistance (LPR) measurements were carried out with a sinusoidal AC voltage amplitude of ± 10 mV at a scanning rate of 0.166 mV/s. The electrochemical noise (EN) measurements were sampled using 1024 points at a rate of 1 point per second. The exposed area of each sample was 1 cm². All the electrochemical corrosion tests were performed at room temperature (20 °C \pm 2). The final electrochemical properties of the samples immersed in each corrosive environment were an average of three measurements performed. In addition, it is also important to mention that the samples were stored in a desiccator after being polished with 4000 grits SiC abrasive paper for a time of 24 hrs before the electrochemical measurements.

5.3 Summary

This part focused on the preparation of the materials and methods to perform the electrochemical measurements. Also, it was introduced a short background about the corrosion studies that exist in the literature. Such review helped to know about the main findings that have been found when the SLM 316L SS is subjected to corrosion attacks. The metallography inspection of this research allowed observing the initial surface features before introducing the material into the selected corrosion environments.

6 Results and discussion

The purpose of this chapter is to show the experimental and simulation results of the samples that were analyzed in this investigation. Both experimental and simulation results show how the laser impacts the material producing a semicircular form known as melt pool. The characterization (the width and depth) of the melt pool is very important since it helps to know the final microstructure of the SLM material. For now, only the melt pool dimensions are investigated by a 2D experimental and simulation setup of a metallic material processed by SLM.

6.1 Experimental results of melt pool dimensions for the SLM AlSi10Mg alloy

Using the methodology presented in chapter 3 to measure the depth and width of the melt pool, in Fig. 6.1, it is shown the dimensions of some melt pools with values that range from 187.452 to 206.916 and from 68.934 to 81.036 μm for width and depth, respectively. As it can be observed, the laser penetration of the SLM AlSi10Mg material is almost three-layer thickness, which means that the laser re-melts the previous layers. Although the re-melting phenomenon is still not analyzed by this work, this event can cause the generation of spherical pores in the material [88].

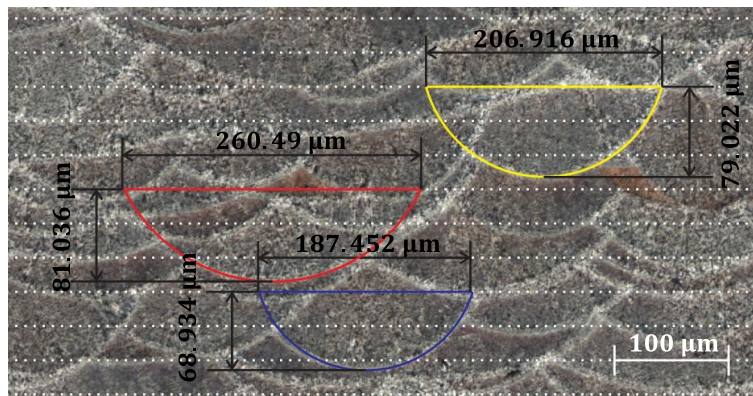


Fig. 6.1 Melt pool dimensions of the SLM AlSi10Mg alloy.

According to the all analyzed data, the SLM AlSi10Mg material produces a melt pool width and depth of 192.1 and 68.9 μm , respectively. These values are very similar with the width of 111.4 and depth of 67.5 μm reported by Li et. al [35] for a successful SLM process of AlSi10Mg powder with 250 W laser power and 200 mm/s scan speed, although the SLM of AlSi10Mg of this research work was carried out using 100 W laser power and 100 mm/s scan speed. Based on the melt pool dimensions, the re-melting process computes quantitatively in a depth of little more than two layers

thickness due to the material is processed using a layer thickness of 30 μm . The characterization of the melt pool is very important because it can be used to validate the simulation results, as is performed by [2].

6.2 Experimental results of melt pool dimensions for the SLM 316L SS alloy

In a similar way, the SLM 316L SS morphology is characterized by its width and depth of the melt pool. The results show that the 316L SS alloy is a melt pool width and depth of 146.28 and 93.5 μm , respectively. Fig. 6.2 shows the SLM microstructure with the characterization of the melt pool. In this case, it is observed that the laser melts the material up to three layers thickness, thus the re-melting process also takes place. Here, it is when the SLM processing parameters optimization plays an important role in the manufacturing of this metallic parts.

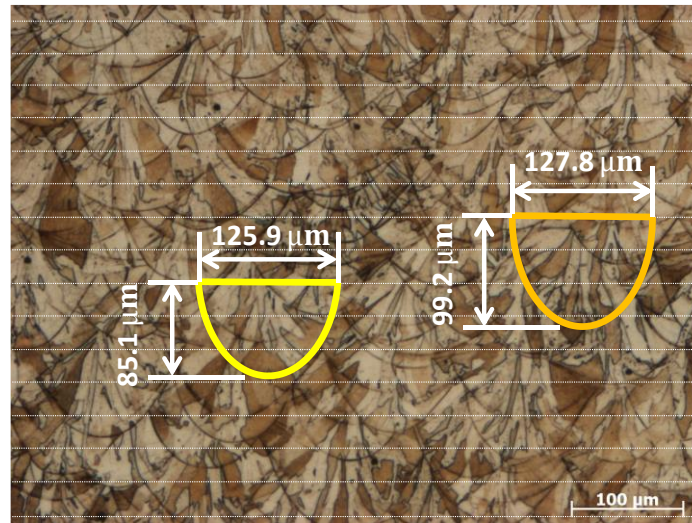


Fig. 6.2 Melt pool dimensions of the SLM 316L SS alloy.

6.3 Simulation results of the SLM AlSi10Mg alloy

The first simulation is performed considering the AlSi10Mg aluminum alloy subjected to a 100 W laser power. The simulation parameters for this alloy are shown in Table 4.1. Using the same simulation parameters, it is possible to enter any value of laser power and get an idea of what value of laser power is better to process the AlSi10Mg alloy by SLM. This is an important advantage of using simulation. Fig. 6.3 and 5.4 show the numerical results using FDM and LBM of the SLM of AlSi10Mg alloy. Additionally, the D2Q4 lattice structure is also introduced in the results.

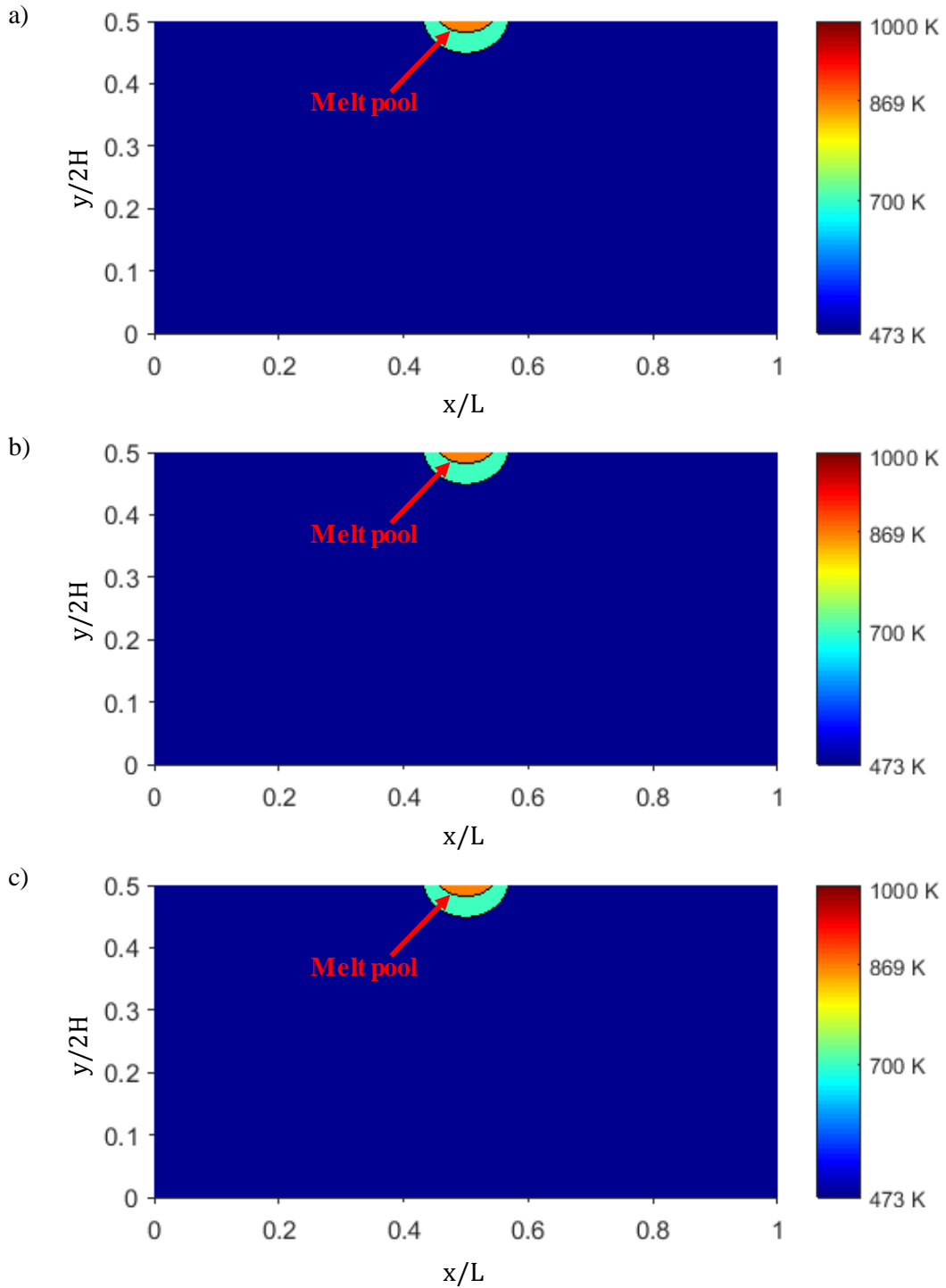


Fig. 6.3 Simulation results by a) FDM, b) LBM D2Q4, and c) LBM D2Q9 methods of the SLM AlSi10Mg alloy at 100 W laser power and 1×10^{-4} s spot irradiation time.

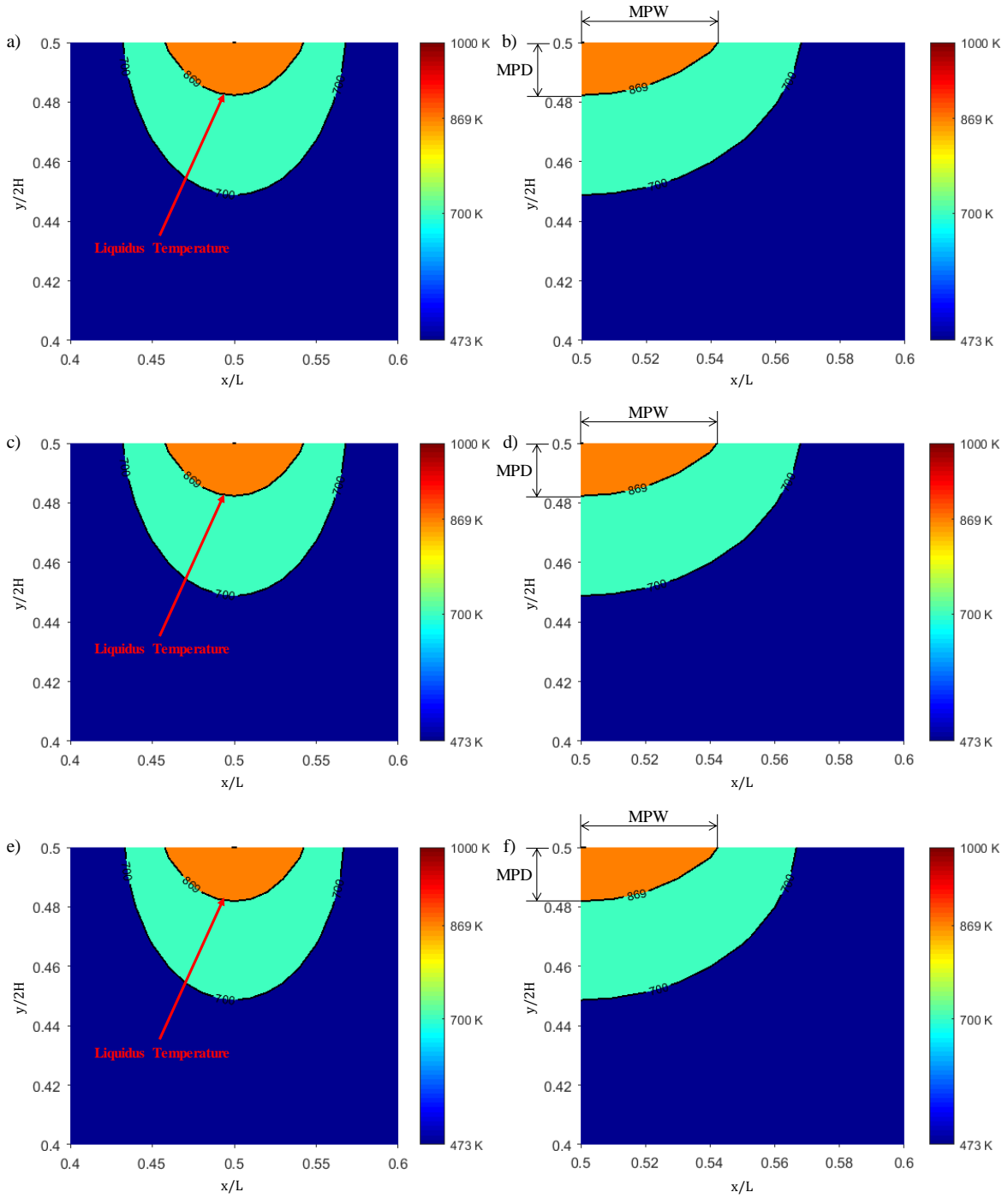


Fig. 6.4 Melt pool with its corresponding dimensions (width and depth) simulated by FDM, a) and b), LBM D2Q4, c) and d), and LBM D2Q9, e) and d), of the SLM AlSi10Mg alloy.

Fig. 6.3 and 6.4 show that the temperature distribution during the SLM process of AlSi10Mg is simulated by three different methods. It is possible to observe the melt pool generated by the laser

as well as its characterization (dimensions). As mentioned previously, melt pool dimensions are important factors to control and reduce defects like porosity, lack of fusion, etc., in the material. See for example [88] where it is established that the surface and pore defects are produced if insufficient heat, lack of fusion, is deposited into the material, due to the particles are partially melted. Thus, using the numerical results of this alloy, it is possible to calculate the melt pool dimensions according to the liquidus temperature pointed out in Fig. 6.4 a), c), and e). In both cases, the melt pool width and depth, MPW and MPD, are very similar. This means that the numerical results agree among the three used methods. The melt pool width is calculated by the double of the difference of $x_1/L = 0.542$ and $x_2/L = 0.5$ that results in $MPW = 8.4 \times 10^{-5}$ m. In a similar way, the melt pool depth of SLM AlSi10Mg is calculated by $2H(y_2 - y_1)$, where $y_2 = 0.5$ and $y_1 = 0.482$, giving as a result of $MPD = 1.8 \times 10^{-5}$ m.

6.4 Simulation results of the SLM 316L SS alloy

The simulation of SLM 316L SS alloy corresponds to the second numerical simulation performed in this investigation. This alloy is subjected to a 400 W laser power and 8×10^{-5} s spot irradiation time. The simulation parameters are shown in Table 4.2. According to the LBM parameters, it is calculated that the LBM needs less computational cost than the continuum methods like FDM. In fact, the LBM based on the D2Q4 and D2Q9 lattice structure for the SLM 316L SS developed in this investigation, uses 14 and 20 time steps, respectively, while the FDM uses 40 time steps. These values of time steps are calculated with the same number of cells and nodes (100) for the corresponding methods. Fig. 6.5 and 6.6 show the simulation results of the melt pool with its corresponding dimensions. As it can be observed, the results agree among the three used methods due to the melt pool dimensions, MPW and MPD, are very similar. According to Fig. 6.6 b), d), and f) the melt pool width is $MPW = 2L(0.555 - 0.5) = 1.1 \times 10^{-4}$ m, and the melt pool depth is calculated as $MPD = 2H(0.5 - 0.476) = 4.8 \times 10^{-5}$ m. For getting an idea about the validation of these results, we can refer to the experimental data, which are approximately calculated as 1.25×10^{-4} m and 8.51×10^{-5} m for width and depth, respectively.

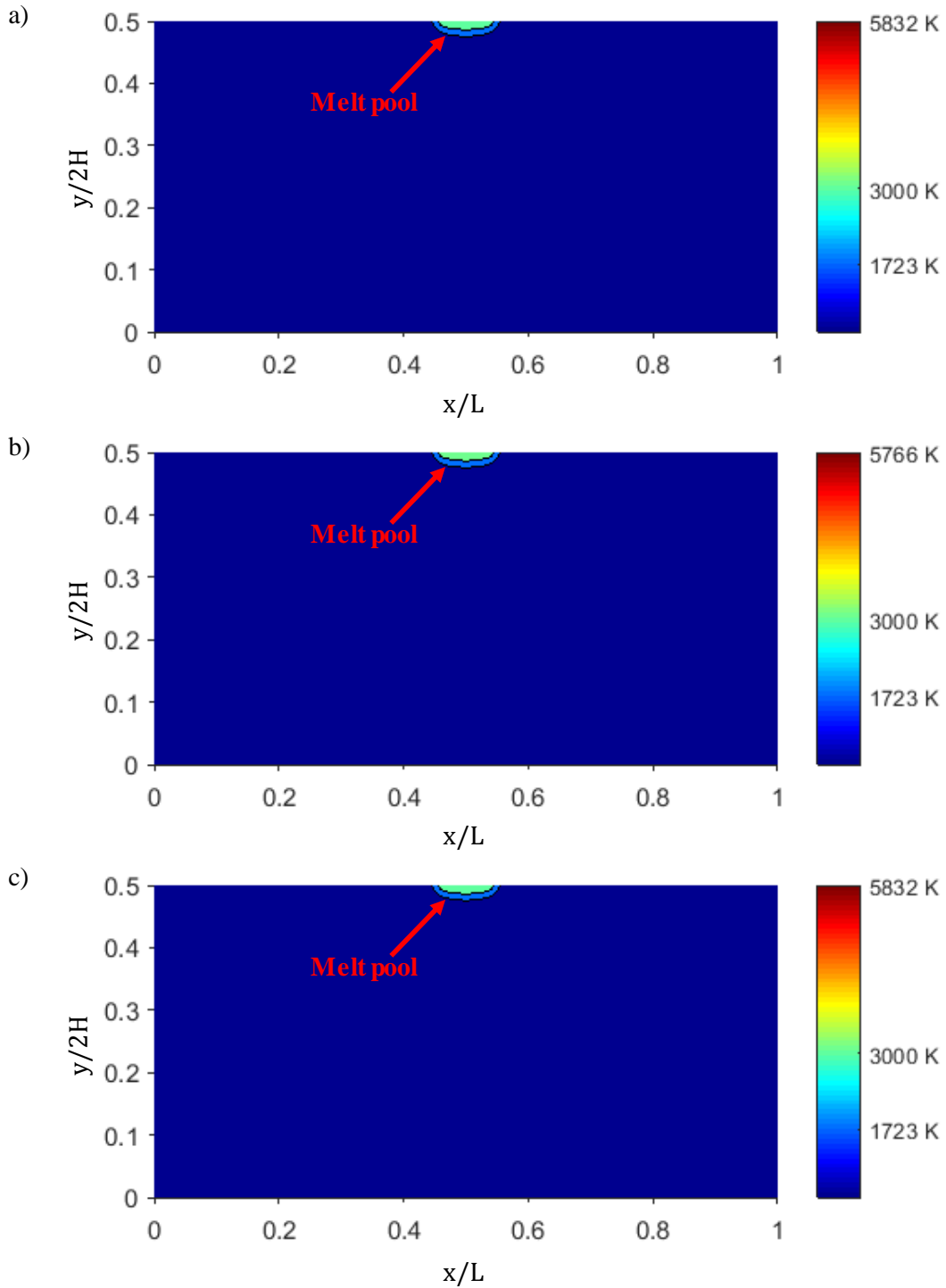


Fig. 6.5 Simulation results by a) FDM, b) LBM D2Q4, and c) LBM D2Q9 of the SLM 316L SS alloy at a 400 W laser power and 8×10^{-5} s spot irradiation time.

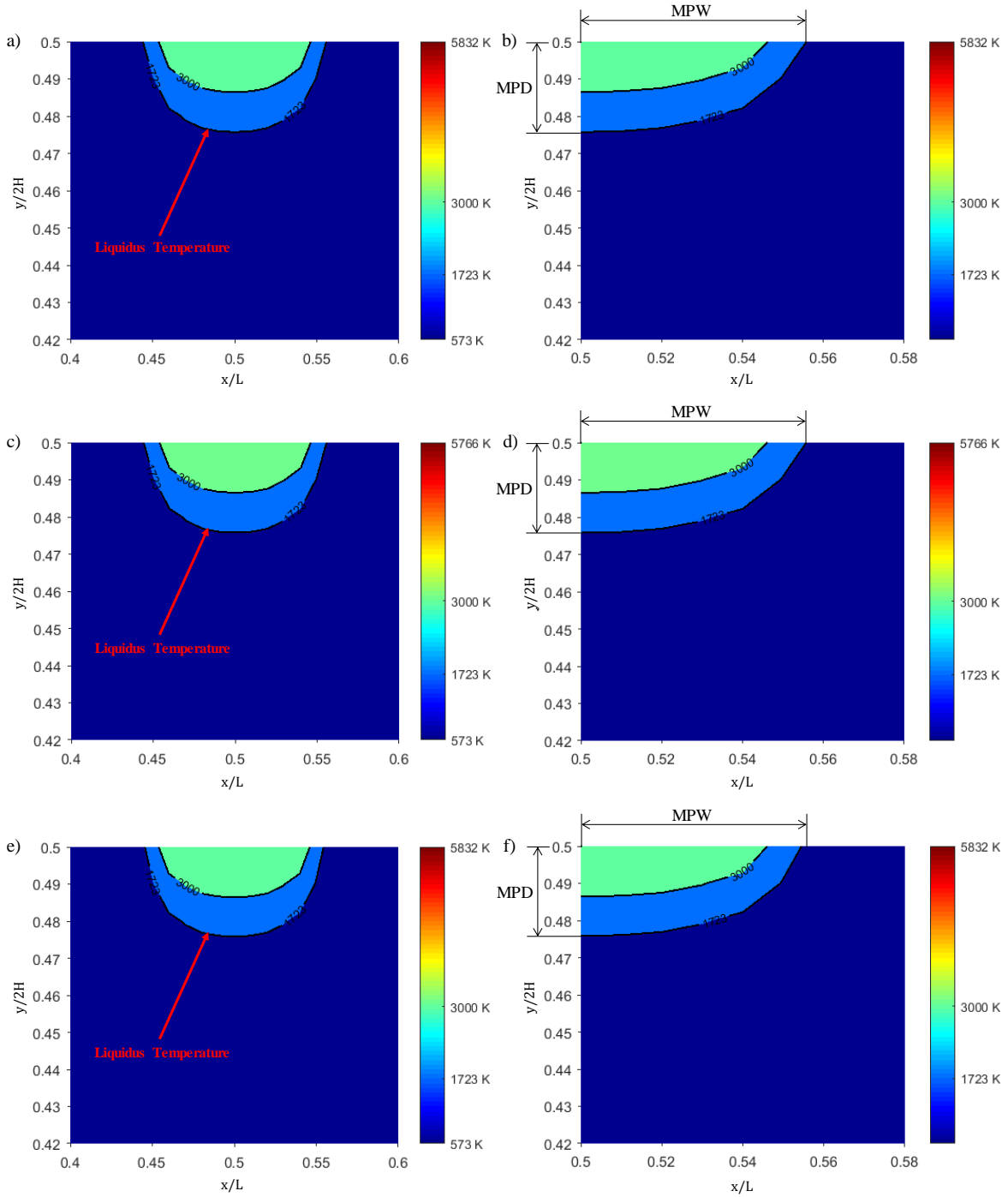


Fig. 6.6 Melt pool with its corresponding dimensions (width and depth) simulated by FDM, a) and b), LBM D2Q4, c) and d), and LBM D2Q9, e) and f) of the SLM 316L SS alloy.

6.5 Comparison among LBM and conventional methods for the SLM AISi10Mg

For the obtention of a results validation of the LBM D2Q9 to simulate the SLM AISi10Mg process, other numerical approaches are also considered by this investigation. The aim is to have a validated initial LBM of the laser melting process that can be used to incorporate more characteristics of the real phenomenon. For this, conventional methods such as FDM and FEM are used to develop a numerical model of SLM with the same features used by the LBM. The comparison among the all used methods allows knowing that discrete models need less computational cost than others, like continuum methods. This is an important advantage of using LBM. Therefore, for showing the validation of the LBM performed by this investigation of SLM, Fig. 6.7 shows the temperature values obtained at the position $x/L = 0.5$ of the simulation domain for all the considered methods. As Fig. 6.7 shows, numerical results agree very well among the four used methods. Note that the temperature decreases over time and position and at $y/2H = 0.5$ the laser impacts on the SLM domain.

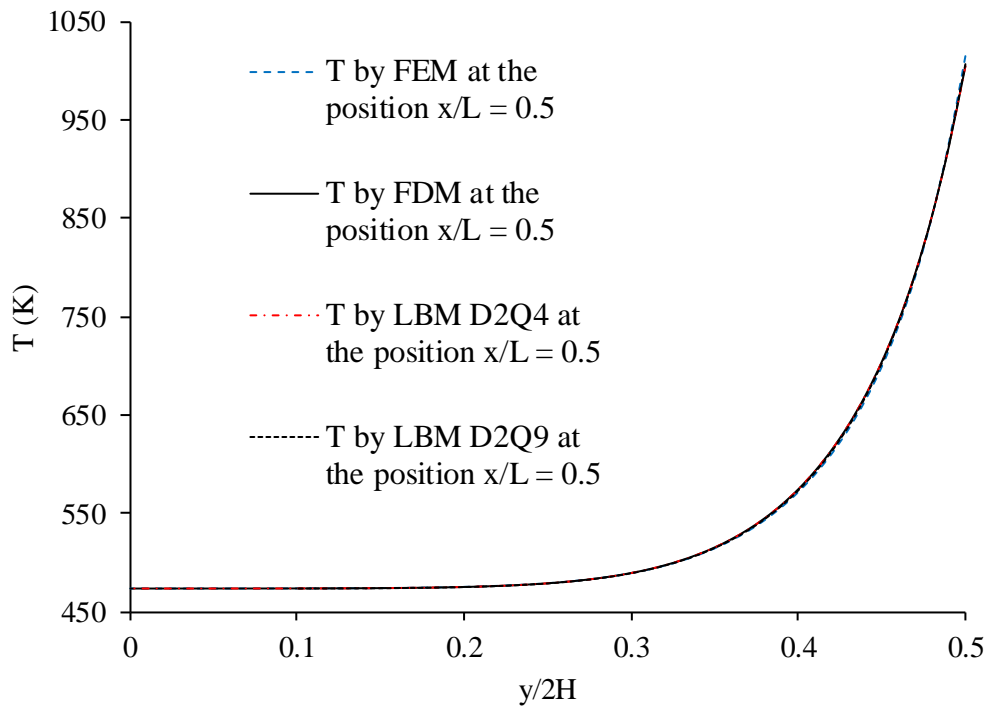


Fig. 6.7 Temperature values at the position $x/L = 0.5$ in the simulation domain for the SLM AISi10Mg alloy simulated by LBM and conventional methods.

6.6 Comparison among LBM and conventional methods for the SLM 316L SS

In a similar way, a comparison among LBM and conventional methods is performed for the SLM 316L SS alloy. Fig. 6.8 shows the temperature values obtained at the position $x/L = 0.5$ of the simulation domain. For this comparison, the FEM line seems not to be so close to the FDM and LBM methods. In addition to that, the numerical simulations of SLM 316L SS give temperatures higher than the liquidus temperature just at the surface where the laser impacts the material. Here is when thermophysical properties dependent on temperature need to be considered as well as the phase transformations during the laser melting process, in this case, the solid, liquid, gas, or interface phases (recommendation for future work).

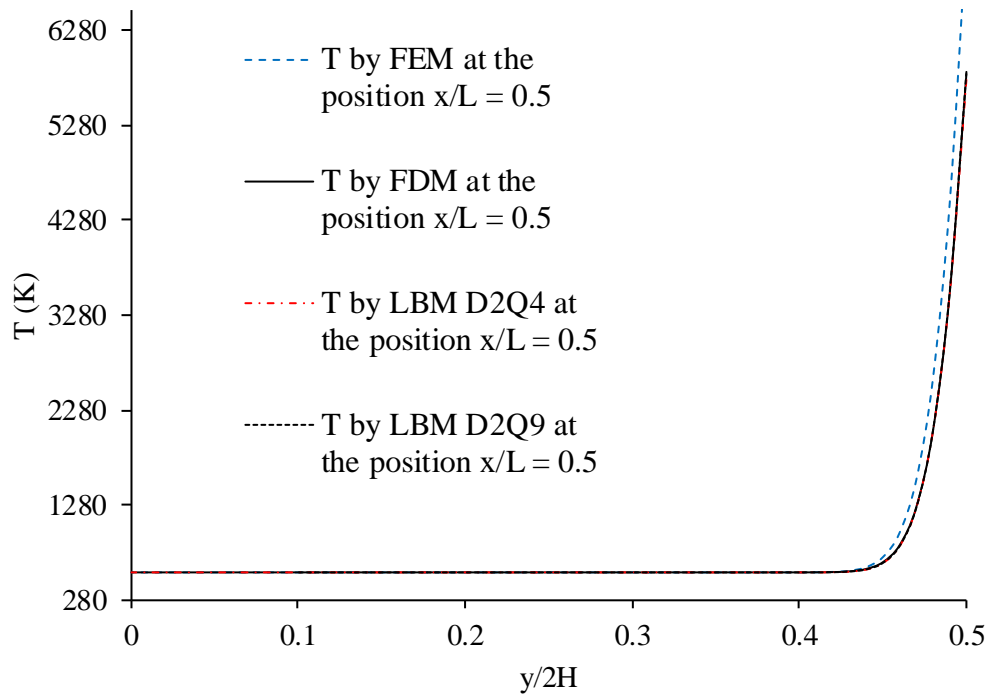


Fig. 6.8 Temperature values at the position $x/L = 0.5$ in the simulation domain for the SLM 316L SS alloy simulated by LBM and conventional methods.

6.7 Advantages of using LBM against continuum methods for the simulation of SLM process

In order to know about the advantages of using LBM against continuum methods for the simulation of SLM process, it was performed a comparison of the elapsed time spent computing solution

required to solve the SLM heat conduction problem by LBM and FDM/FEM. This comparison shows that the LBM is faster than the FEM. At the same time, it can be compared that FDM solves the computational routine of SLM with a similar or less time than the LBM. For this, Table 5.1 shows the execution time of each used method to simulate the laser melting process.

Table 6.1 Estimated execution time for the LBM and FDM/FEM simulations.

Simulation	Method of solution	Number of time steps or iterations	Commercial software for the computational routine	Estimated execution time
SLM AlSi10Mg	FDM	500	Matlab	0.4759 s
	FEM	47	Ansys 17.0	32 s
	LBM D2Q4	301	Matlab	1.0779 s
	LBM D2Q9	456	Matlab	2.3619 s
SLM 316L SS	FDM	40	Matlab	0.1342 s
	FEM	26	Ansys 17.0	26 s
	LBM D2Q4	14	Matlab	0.3759 s
	LBM D2Q9	20	Matlab	0.6629 s

For the FDM and LBM, the elapsed time during the simulation was obtained by the **tic** and **toc** functions of the Matlab software, giving the value of the elapsed time in seconds. In the FEM, it was used the Preconditioned Conjugate Gradient (PCG) iterative equation solver, since it requires less disk file space, being faster for large methods. Using this solver, it is generated a .PCS file in the directory of the solution, which gives detailed information about the performance of the simulation. In this way, the information of that file is used to calculate the elapsed time during the simulation by the difference between the time at the first and at the last iteration. This information is printed in the appendix section in which it can be calculated that the elapsed time for the FEM simulations of SLM AlSi10Mg and 316LSS is 32 s and 26 s, respectively. Based on these values, it is observed that the LBM is faster than the FEM.

6.8 Chemical microanalysis

X-ray energy dispersive spectroscopy (EDS) analyses were also performed in order to characterize the specimen's defects morphology before making the electrochemical measurements. For this, a selected area of the horizontal and vertical testing surface was explored in which imperfections with their respective shape and chemical composition were identified. Fig. 6.9 shows two SEM micrographs displaying some SLM irregularities with their corresponding chemical composition. In

this case, Fig. 6.9a presents an SLM defect of 18 μm of longitude in the horizontal surface. Its elemental composition at a specific area inside of it, red zone in Fig. 6.9b, shows high contents of Si and Mn as well as O. On the other extreme, the irregularity shown in Fig. 6c with its respective chemical composition in Fig. 6.9d, presents high contents in Fe and O and is in the vertical surface of the material. The compositional analysis of the SLM defect shown in Fig. 6.9a has confirmed the results by Chao et al.'s [82] study, where it was reported that the SLMed 316L SS alloy is susceptible to content spherical and irregular defects with Si and O. In addition to this, it can be observed that the SLM defects shown in Fig. 6.9a and c have a different shape with each other, i.e., while in Fig. 6.9a the pore has an outstretched shape, in Fig. 6.9c there are two types, spherical and irregular shaped pores. Although the SLM defect presented in Fig. 6.9a is not completely spherical, it seems that it was formed from a spherical SLM defect. According to this, it can be established that the horizontal surface of an SLMed material suffers from shape-outstretched pores formed from spherical pores while the vertical surface has spherical and irregular pores. It is well known that spherical pores are provoked by gas-induced from the liquid metal during the fast solidification process and irregular defects are associated with the lack of metallic powder [46].

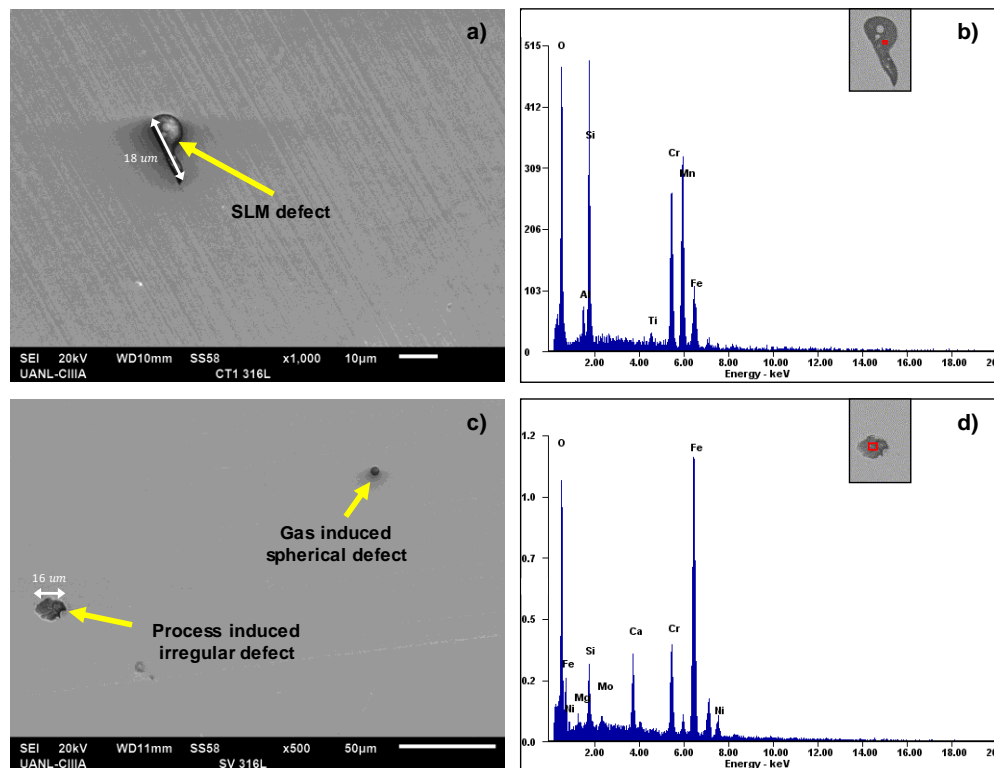


Fig. 6.9 SEM images of the polished surfaces of the samples displaying some SLM defects in the material (left-hand side) and chemical composition obtained by EDS of those irregularities (right-hand side).

Although EDS analyses were carried out at the microscopic level (SEM), these agree with the results of nano-inclusions (TEM) reported by Chao et al. [82], where the elemental composition of the nano-defects reported high contents of Si and Mn. In fact, Saeidi et al.'s [89] study pointed out that nano-inclusions are formed due to the accumulation of O, Al, Si, and Mn. Based on this, the SEM image of the horizontal surface shown in Fig. 6.10 confirms the same, i.e., certain impurities with high contents of Mn, Cr, and O have also been localized which could lead to the formation of (MnCr)O inclusions. Even though these defects cannot influence as localized pitting sites, the Cr content accompanied by the high Si content could mean the formation of Silicates, as was reported by Kong et al. [70].

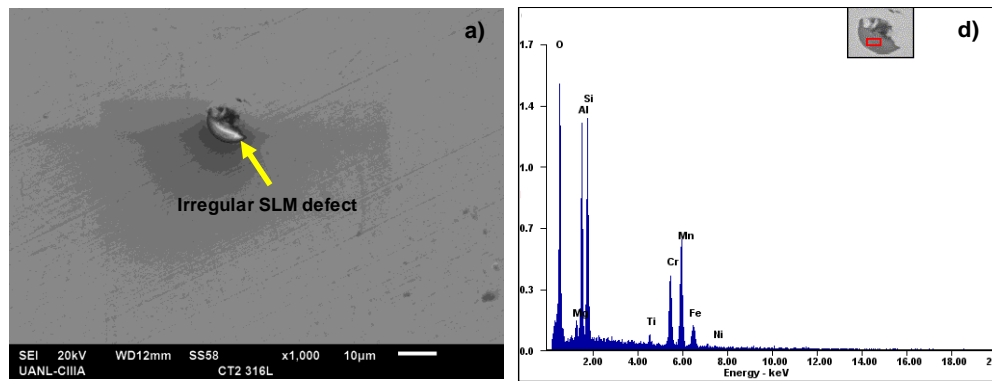


Fig. 6.10 a) SLM inclusion found on the polished surface and b) its EDS chemical composition showing high contents of O, Al, Si, and Mn.

6.9 Characterization of the microstructure

Fig. 6.11 shows the microstructure evolution of the SLMed 316L stainless steel. The micrograph was obtained by optical microscopy (OM) which shows the resulting micro/macro-structure of the horizontal and vertical surfaces, normal and parallel to the build direction, respectively. It can be observed the shape of the melt pool for both surfaces and for certain points how grains tend to grow up from the fusion line to the center of the melt pool. It is well known that the growth direction to the melt pool center is because the thermal gradients produced by the SLM process are higher in the melt pool center than along the fusion line [46, 89, 90]. In addition, the microstructure is characterized by martensitic with a dark brown tone, pointed out with the yellow arrow, whereas austenite is shown with a clearer brown tone and pointed out with the blue arrow. It can be observed from Fig. 6.11a,b that the fusion lines or melt pool boundaries are generated by the Gaussian distribution of the laser energy density. Although the melt pool boundaries are not so

distinguishable, it is possible to appreciate the shape of the melt pool for each metallographic image. Fig. 6.11a shows the melt pools with a shape of enlarged ovals located at 90° due to the scan rotation between the successive layers (SLM processing parameter mentioned in Table 3.5) and Fig. 6.11b illustrates the cross-section of the melt pool with a semicircular shape, typical of the SLM process.

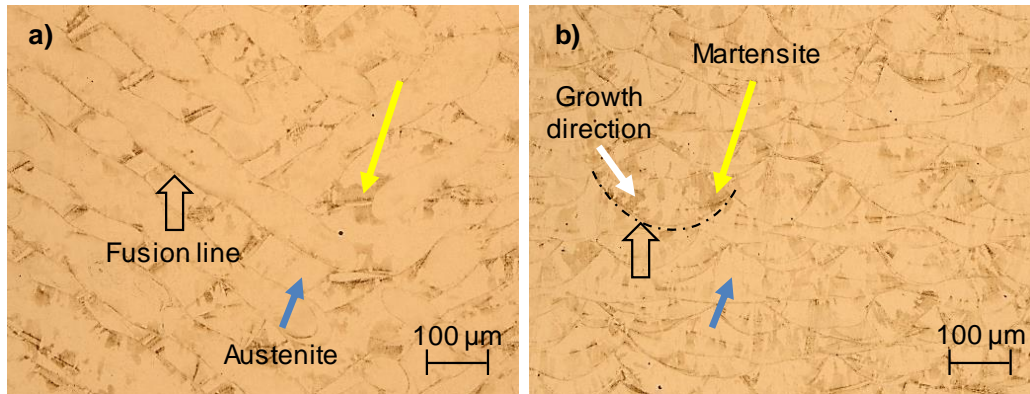


Fig. 6.11 Representative optical micrograph showing the SLMed 316L SS microstructure of the horizontal a) and vertical b) surfaces. Growth direction is indicated with a white arrow while the fusion line is shown with an open arrow.

It is important to notice how the powder melting manufacturing process can produce fine grains which could influence the final electromechanical characteristics of the material. As for the SLM microstructure in the horizontal surface (XY plane) of the sample, it has been established that fusion lines could not be completely true. According to Rao et al. [17], this is because the melt pool cores are not totally normal to the observation XY plane being that the samples are subjected to the cutting and polishing process. Nevertheless, the SLM microstructures of this research work were taken carefully, based on the standard procedures. It is important to highlight that the size of the melt pool (melt pool width and depth) is not considered in the influence on the corrosion behavior.

6.10 Corrosion results

6.10.1 Linear polarization resistance (LPR)

Corrosion rate measurements undertaken of the SLMed samples were calculated using the Stern-Geary relationship [91], Eq. 6.1

$$i_{corr} = \frac{\beta}{\Delta E/\Delta I} = \frac{\beta}{R_p} \quad (6.1)$$

where β is the Stern-Geary constant, ΔE potential gradient, ΔI current gradient and $\Delta E/\Delta I$ is the polarization resistance (R_p). Note that in Eq. 6.2 the Stern-Geary constant can be calculated from the anodic (b_a) and cathodic b_c Tafel slopes [92].

$$\beta = \frac{b_a b_c}{2.3(b_a + b_c)} \quad (6.2)$$

Based on the LPR technique, the SLMed 316L SS was studied into the three electrolytes, and its corrosion characteristics (E_{corr} , I_{corr} , and corrosion rate) were obtained. Firstly, the horizontal samples were considered for the electrochemical measurements. For this, Table 6.2 shows the corresponding parameters, where it can be observed that the major corrosion rate is 1.31×10^{-3} mm/year obtained in H_2SO_4 in comparison with the value of 8.85×10^{-5} mm/year calculated in NaCl, as well as with the value of 7.8×10^{-5} mm/year for the H_2O electrolyte.

Table 6.2 Electrochemical parameters of the SLMed 316L SS tested in horizontal (XY plane).

Sample	Electrolyte	Electrochemical parameters		
		E_{corr} vs SCE (mV)	I_{corr} (mA/cm ²)	Corrosion rate (mm/year)
Horizontal (XY plane)	H_2O	-123 ± 6	7.29×10^{-6} $\pm 4 \times 10^{-7}$	7.8×10^{-5} $\pm 4 \times 10^{-6}$
	3.5 wt. % NaCl	22 ± 1	8.27×10^{-6} $\pm 4 \times 10^{-7}$	8.85×10^{-5} $\pm 4 \times 10^{-6}$
	20% H_2SO_4	112 ± 5	1.23×10^{-4} $\pm 6 \times 10^{-6}$	1.31×10^{-3} $\pm 6 \times 10^{-5}$

On the other hand, the electrochemical parameters were also obtained for the vertical samples. For this, Table 6.3 shows the corrosion rate values of 9.2×10^{-5} , 2.45×10^{-3} , and 2.4×10^{-2} mm/year, which correspond to the H_2O , NaCl, and H_2SO_4 electrolytes, respectively. Note that the major corrosion rate is 2.4×10^{-2} mm/year obtained in H_2SO_4 and the minor is $9.2 \times$

10^{-5} mm/year calculated in H₂O. As it can be noticed, the results between the two samples indicate that the corrosion rates for the XZ samples are higher than that for the XY samples. These results give a first notion of how the surface orientation of an SLM material influences its corrosion resistance.

Table 6.3 Electrochemical parameters of the SLMed 316L SS tested in vertical (XZ plane).

Sample	Electrolyte	Electrochemical parameters		
		E_{corr} vs SCE (mV)	I_{corr} (mA/cm ²)	Corrosion rate (mm/year)
Vertical (XZ plane)	H ₂ O	23 ± 1	8.6×10^{-6} $\pm 4 \times 10^{-7}$	9.2×10^{-5} $\pm 5 \times 10^{-6}$
	3.5 wt. % NaCl	-108 ± 5	2.3×10^{-4} $\pm 1 \times 10^{-5}$	2.45×10^{-3} $\pm 2 \times 10^{-3}$
	20% H ₂ SO ₄	278 ± 14	2.3×10^{-3} $\pm 1 \times 10^{-4}$	2.4×10^{-2} $\pm 1 \times 10^{-3}$

6.10.2 Electrochemical noise (EN)

Electrochemical noise (EN) tests were also performed in this research work. Although linear polarization resistance (LPR) gives a prediction about the corrosion resistance of the SLMed 316L SS, it is difficult to understand the type of corrosion by that mean. For this, in Fig. 6.12a it can be observed the potential time series that the samples experiment when they were immersed in a chloride-containing solution at room temperature (20 °C ±2). At the side (Fig. 6.12b), it is shown the current time series of the samples. Herein, it can be noticed that the XZ sample seems to be more active than the XY sample. This is because the corrosion current density of the vertical sample increases rapidly for certain periods of time, even recording a few transients of high frequency and amplitude compared with the horizontal sample, as shown by the red line. According to Gaona et al. [85], the characteristics of those transients can lead to localized corrosion. On the other hand, it can be noticed that the horizontal sample maintains a constant potential during the test. Although there are also some transients in the XY sample, the stability in its corrosion potential indicates that it could have been generated by a passive film formed by chromium oxide, even after the cutting process of the samples. Additionally, the surface orientation also influences the corrosion behavior and the film oxide composition [17, 93]. In fact, the corrosion film formed naturally after cutting generates a small barrier to the aggressive agents of the electrolytes such as Cl⁻ ions. Nevertheless,

once the system begins to interact, this passive film has a way to a dissolution of metal ions (M^+) in the anodic zones, while in the cathodic zones the reduction of oxygen is carried out through the formation of OH^- ions.

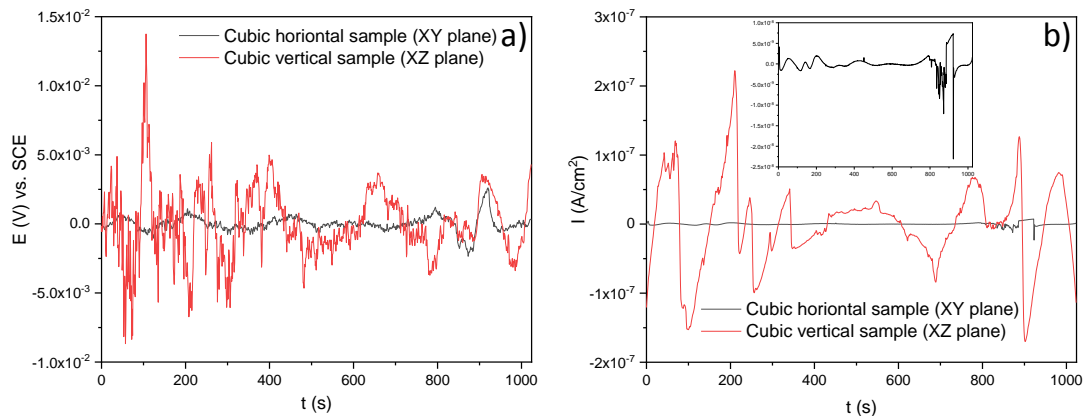


Fig. 6.12 Time series in potential and current of the SLMed 316L SS in 3.5 wt. % NaCl, a) potential versus time and b) current versus time.

Andreatta et al. [94], reported that the 316L SS alloy evaluated in NaCl with acid and neutral environment presents a passivate behavior wider than the alloys fabricated conventionally. Besides, the SLMed 316L SS alloys do not present a tendency to pitting metastable [94]. On the other extreme, Sander et al. [95] determined that the typical frequency of pitting metastable in 3D printed 316L samples is, in many cases, considerably lower than the forged 316L. In addition, those with the highest frequency of metastable pitting are associated with higher porosity. The transients present in these samples are typical of stable pitting behavior.

Fig. 6.13 shows the corrosion behavior of the SLM material developed by the electrochemical noise (EN) test using H_2SO_4 . In this case, the horizontal sample also tries to maintain a constant potential while the vertical sample increases its potential by several periods of time and then decreases throughout time. In Fig. 6.13b, it seems there are a few transients in current that could mean pitting corrosion for both samples.

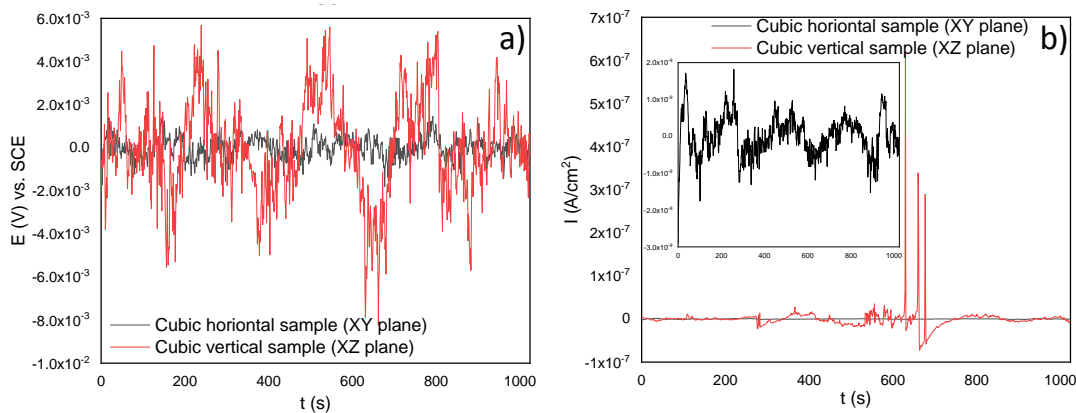


Fig. 6.13 Time series in potential and current for the SLMed 316L SS in 20% H_2SO_4 , a) potential versus time and b) current versus time.

In Fig. 6.14a and b, it can observe the time series in potential and current, respectively, of the horizontal and vertical samples immersed in H_2O . Note that the electrochemical response of the XZ sample marks several transients that could mean metastable pitting typical of these alloys [95] (Fig. 6.14b), fortunately, its corrosion potential is maintained constant (Fig. 6.14a). In the case of the XY sample, this slightly increases its corrosion potential and tends to passivate due to its constant corrosion current density. However, the vertical sample seems to be more active than the horizontal sample since it has higher transients.

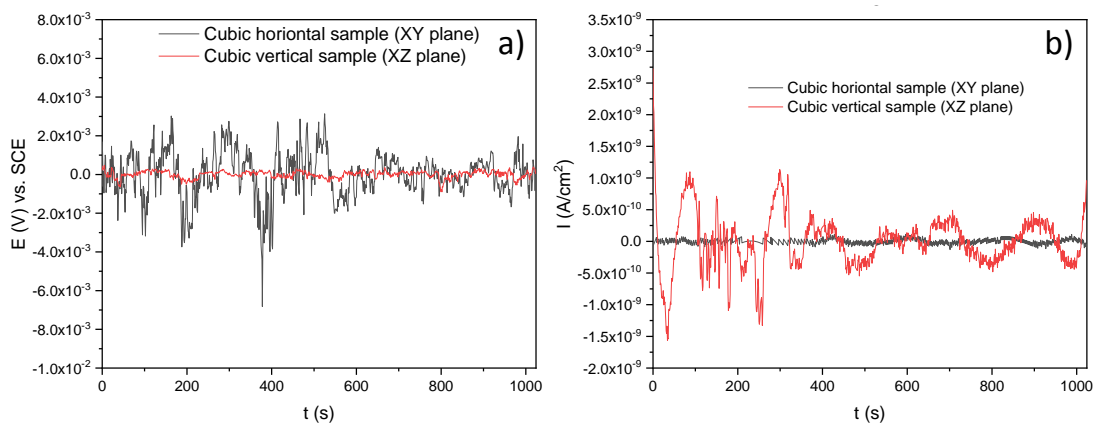


Fig. 6.14 Times series in potential and current for the SLMed 316L SS in H_2O , a) potential versus time and b) current versus time.

In order to summarize, Table 6.4 shows the electrochemical noise (EN) characteristics such as electrochemical noise resistance (R_n), corrosion current density (I_{corr}), corrosion rate, skewness,

and the corrosion type that the samples experiment when were immersed into the three electrolytes. It can be noticed that all the samples (horizontal and vertical) lead to two types of corrosion, localized for NaCl, and uniform for the H₂SO₄ and H₂O electrolytes. It can be noted that the minor corrosion rate is 1×10^{-5} mm/year for the H₂O electrolyte. The identification of the corrosion type is based on statistical moments with Skewness, which are the 3rd and 4th statistical moments [96].

Table 6.4 Electrochemical noise (EN) characteristics of the SLMed 316L SS tested in the three electrolytes (3.5 wt. % NaCl, 20% H₂SO₄, and H₂O)

Electrolyte	Sample		
	Horizontal (XY plane)	Vertical (XZ plane)	
3.5 wt. % NaCl	R_n ($\Omega - \text{cm}^2$)	299514	41451
	I_{corr} (mA/cm ²)	$8.7 \times 10^{-5} \pm 4 \times 10^{-6}$	$6.27 \times 10^{-5} \pm 4 \times 10^{-6}$
	Corrosion rate (mm/year)	$9.9 \times 10^{-4} \pm 5 \times 10^{-5}$	$7.1 \times 10^{-4} \pm 4 \times 10^{-5}$
	Skewness	-1.65	-0.012
	Corrosion type	Localized	Localized
20% H ₂ SO ₄	R_n ($\Omega - \text{cm}^2$)	926782	422588
	I_{corr} (mA/cm ²)	$2.8 \times 10^{-4} \pm 1 \times 10^{-5}$	$6.15 \times 10^{-5} \pm 6 \times 10^{-6}$
	Corrosion rate (mm/year)	$3.2 \times 10^{-3} \pm 2 \times 10^{-4}$	$7 \times 10^{-4} \pm 4 \times 10^{-5}$
	Skewness	-0.17	0.27
	Corrosion type	Uniform	Uniform
H ₂ O	R_n ($\Omega - \text{cm}^2$)	29136364	422588
	I_{corr} (mA/cm ²)	$8.9 \times 10^{-7} \pm 4 \times 10^{-8}$	$6.15 \times 10^{-5} \pm 3 \times 10^{-6}$
	Corrosion rate (mm/year)	$1 \times 10^{-5} \pm 5 \times 10^{-7}$	$7 \times 10^{-4} \pm 4 \times 10^{-5}$
	Skewness	0.05	0.27
	Corrosion type	Uniform	Uniform

In Fig. 6.15 a histogram is illustrated in order to compare the corrosion rate between the two samples (horizontal and vertical), taking into account the three electrolytes. In effect, it can be observed that the minor corrosion rate is presented in the XY sample, immersed in H₂O. On the contrary, the sample with the worst corrosion behavior is also horizontal but immersed in H₂SO₄ since it has a major corrosion rate (3.2×10^{-3} mm/year) according to the graph. It is worthy to mention that the obtained results of the corrosion current densities are an average of the anodic and

cathodic reactions registered on the surface of the material immersed into the corresponding electrolyte throughout testing time.

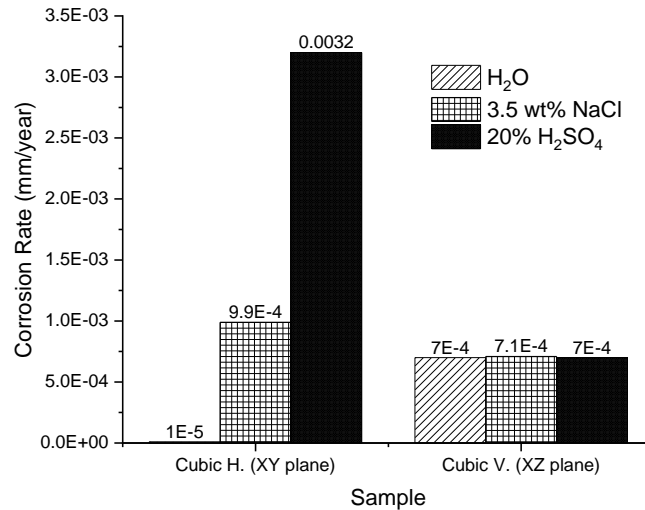


Fig. 6.15 Comparison of the corrosion rate between the samples into the three electrolytes. The number of points for each corrosion test was 1024 points at a rate of 1 point per second. It is shown the average corrosion rate for each performed testing.

6.11 Corroded surfaces of the SLMed samples

Fig. 6.16 shows the optical microscope images after the electrochemical tests, in which a localized attack is observed in the NaCl solution, as a product of the Cl ions present. In the electrolyte of H₂O and H₂SO₄ the corrosion mechanism is uniform; however, the acid generates a greater dissolution of the oxide layer formed by the AM 316L stainless steel.

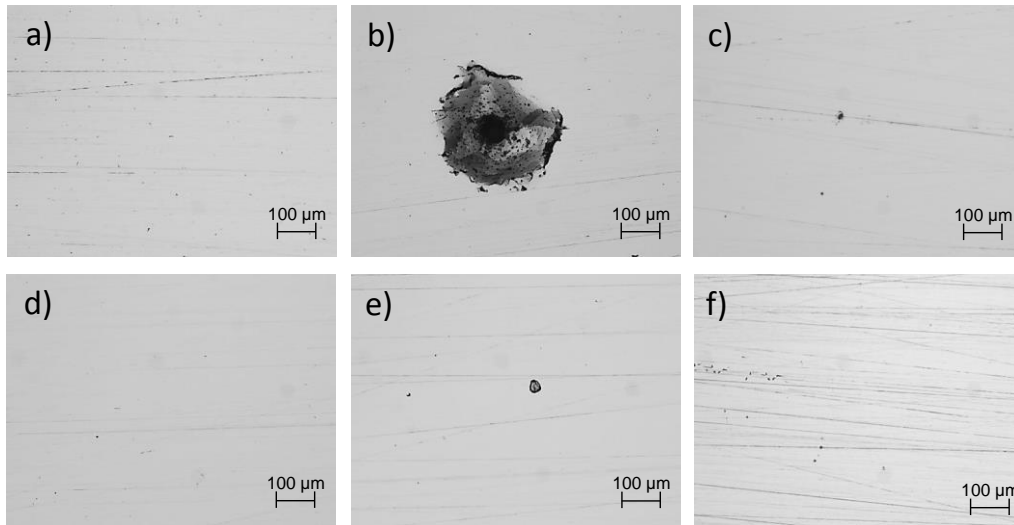


Fig. 6.16 Morphologies of the specimens after the electrochemical tests. Optical Microscope at 100X. XY plane: H₂O (a), NaCl (b), and H₂SO₄ (c); XZ plane: H₂O (d), NaCl (e), and H₂SO₄ (f).

In Fig. 6.17, it is shown the morphologies taken by SEM and EDAX analysis of the XY and XZ specimens evaluated in NaCl. It is observed that the pits are developed within the sub-grains due to the galvanic pair that develops between the Mo-enriched phases (sub-grain boundaries) that are segregated during the fabrication due to the rapid solidification which does not give time to the Mo atoms to complete the diffusion [97, 98] and the Fe-enriched phases.

Through EDAX analysis, it can be observed for both specimens in the XY and XZ planes, the presence of the element chlorine, which will preferentially attack the sub-grains that act as anodes and the grain boundaries enriched in Mo as cathode [80]. In addition, the presence of the elements of the base material (chromium, nickel, molybdenum, manganese) and the traces of elements that correspond to the test electrolyte also influence.

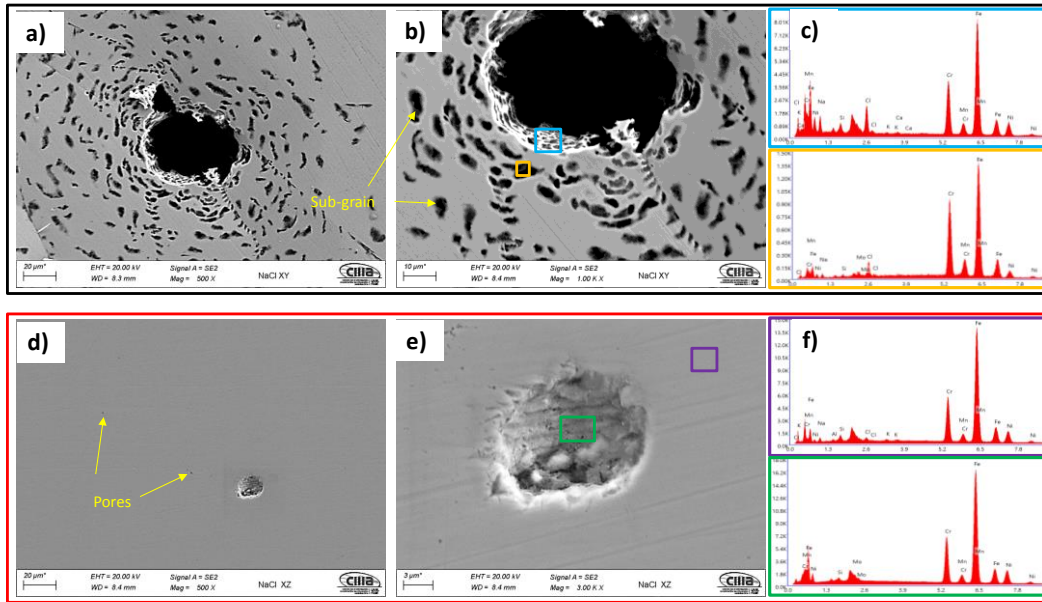


Fig. 6.17 Morphologies of the specimens after the electrochemical tests in 3.5 wt. % NaCl at 500x and 1000x. XY plane (a), (b), and (c); XZ plane (d), (e), and (f). ZEISS EVO Scanning Electron Microscope (SEM).

The corrosion process of the 316L AM alloys in the H_2SO_4 electrolyte presents a very different behavior from that observed in a saline environment. In this case, for the specimens in the XY plane, the corrosion process is generated over the entire surface of the sample, and in some cases, it develops within the imperfections of the material, developed by the manufacturing process, specifically in the pore walls. The EDAX analyses show the presence of sulfur which, together with the acidic pH of the electrolyte, develops the corrosion process; the corrosion products are not identified into the imperfection core, which indicates that the process is developed through the walls (Fig. 6.18).

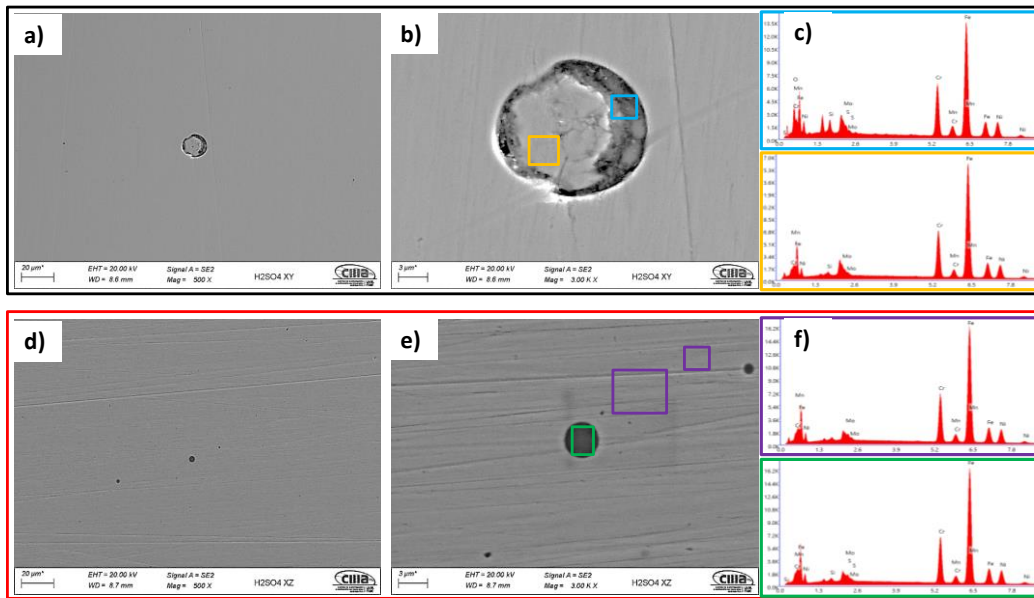


Fig. 6.18 Morphologies of the specimens after the electrochemical tests in H_2SO_4 at 500x and 1000x. XY plane (a), (b), and (c); XZ plane (d), (e), and (f). ZEISS EVO Scanning Electron Microscope (SEM).

It was found that the SLMed 316 L SS alloy presents a little increment in the corrosion rate with a vertical orientation compared with the horizontal direction. This was proved by LPR when the material is immersed in the three electrolytes. It can be supposed that the variation in the corrosion resistance is because of the surface orientation of the SLM parts. Besides, based on the EDS analyses performed in the SLM defects, these ones indicate that there are high concentrations of O, Al, Si, and Mn into the analyzed irregular and spherical pores, which could cause loss of passivity and an increment of the corrosion current density, as it was observed in the vertical samples.

On another hand, as for the material tested by the EN technique, this method shows that the SLMed 316L SS alloy also has a corrosion resistance higher in the horizontal direction than for the vertical one when the material is tested in H_2O . On the contrary, it is lower in NaCl and H_2SO_4 for the XY plane due to the spherical pores which develop localized corrosion for the NaCl electrolyte. It can be observed that the localized attack, as a result of Cl ions, is presented in the pore walls rather than in the cores. Nevertheless, it can be established that the surface orientation of an SLM material does play an important role in its corrosion resistance when there are not severe SLM defects. In fact, pits are developed within the sub-grains due to the galvanic pair that develops between the Mo-enriched phases (sub-grain boundaries).

It is worthy to mention that the EN technique, as well as the morphology observation via EDS, SEM, XRF analyses, gives important considerations of AM parts processed by SLM. In fact, the experimental morphology observation indicates that the horizontal surface suffers from spherical gas-induced pores meanwhile the vertical surface presents spherical and irregular pores associated with the lack of metallic powder during the laser process. As for the EN technique, this one makes a first calculation of the type of corrosion developed for an additively manufactured material considering three different environments since the corrosion studies in the literature have been only focused on corrosion resistance.

Although it does not still have a quantifiable factor, e.g., the grain size in vertical and horizontal directions, levels of porosity in both surfaces, size of the melt pool, etc., that can quantitatively compare the best corrosion behavior in the horizontal samples, this study opens the door to study the SLMed 316 corrosion behavior from a viewpoint more microstructural for future investigations. Besides, it can be studied the corrosion resistance of SLMed 316L SS products considering the amount of chromium on the surface of the material.

6.12 Summary

Two simulations of LBM for the SLM AlSi10Mg and 316L SS alloys were performed. Both simulations consider the physics of the phenomenon and the processing parameters such as the power of the laser, spot irradiation time, laser diameter, preheating temperature, ambient temperature, and the physical properties of each selected material. The simulations can compute the temperature field produced by the laser. It was possible to calculate the melt pool dimensions, width and depth. The numerical results of LBM are compared with the numerical results of conventional methods, which are in good agreement. According to the experimental observation, it was also possible to obtain the dimensional characterization of the melt pool. The experimental results give an idea of how the laser impacts the material where the numerical results show similar qualitative information (melt pool geometry). It was studied the influence of the microstructure orientation as well as the surface features on the corrosion behavior of the SLM 316L SS. The electrochemical results indicated that the material develops a major corrosion rate in the XZ plane than the XY plane.

7 Conclusions and future work

7.1 Conclusion

- The development of a numerical tool for studying the SLM aluminum and steel alloys represents great attention for the industry and scientific communities. In this case, a different simulation via LBM using the standard D2Q9 lattice structure has been developed to simulate the laser melting process of the AlSi10Mg and 316L SS alloys. It is worthy to mention that in literature the most used techniques to study the SLM process have been the weighted residual approaches such as FDM, FEM, and FVM. This indicates that only certain investigations of SLM have followed the idea of using distribution functions. In fact, the most common SLM materials studied by distribution functions have been nickel and titanium-based alloys.
- Knowing that there is a great number of metallic materials that can be processed by SLM where only a few have been studied by discrete numerical techniques such as LBM, the development of a LBM for the laser melting process of aluminum and steel alloys will impact the knowledge of this research field. In addition to that, aluminum and steel alloys are also great candidates for the aerospace industry. For this reason, it is important to develop fast and effective numerical tools that allow to simulate the effect of the processing parameters on the thermal behavior of the material since the final properties of an SLM material are mainly dependent on the thermal field during the manufacturing process.
- In this investigation, the numerical model of SLM based on the LBM is able to predict the thermal evolution produced by the laser beam. It could observe how the laser transfers energy to the solid material (simulation domain) increasing its temperature and producing the melt pool. The zone (melt pool) where the laser impacts the material is characterized by its width and depth. These parameters are very important for the final microstructure prediction of the material. Using conventional methods to also simulate the SLM process, it was observed that the melt pool dimensions are in good quantitative agreement with those other continuum methods. On the other hand, experimental observations were also performed in this research work. These data show a qualitative agreement with the numerical results. In order to obtain a quantitative comparison between experimental and numerical results, the SLM model needs to incorporate more characteristics of the

phenomenon, such as laser movement, layer deposition, phases transformation, which were not considered by this methodology.

- Although an initial LBM for Selective laser melting (SLM) aluminum and steel alloys has been developed, this model is able to simulate the temperature distribution with less computational time than the conventional methods. The standard D2Q9 lattice structure for the SLM 316L SS alloy reproduced the numerical results with the half of the number of time steps used in FDM. This is an important advantage that proves that LBM is faster than FDM. On the other extreme, the number of time steps in the simulation of the SLM AlSi10Mg alloy by LBM was also less. The calculations were performed according to the exposure time of the laser irradiation, which is an important parameter in the SLM process, and optimizing it, can reduce costs and time of manufacturing during the processing of AM parts.
- Finally, the 2D LBM developed for SLM was compared with the numerical results of continuum approaches. It was obtained the temperature distribution along the middle line of the simulation domain which shows to be consistent with the other used methods. This method was able to consider some characteristics of the SLM process such as laser power, pre-heating temperature of the medium, ambient temperature, spot irradiation time, laser diameter, as well as the heat conduction problem and convective heat losses. To emphasize the potential of this numerical model, it was possible to solve the governing differential equation of the SLM process in only two steps known as collision and streaming. Once again, the elapsed computational time spent for the solution in each model verified that the LBM method is faster than the FEM.

As for the study of the electrochemical properties of the SLMed 316L SS, the following remarks were found:

- The SEM and EDS analyses performed on the polished surface of the samples indicated the formation of irregular and spherical pores with contents of O, Al, Si, and Mn in the SLM defect. The spherical pores were attributed to the induced gas during the fast solidification process, and irregular defects with dimensions of approximately 18 μm were associated

with the lack of metallic powder. It was confirmed by the EDS analyses of this research work that inclusions in the SLMed 316L SS were formed due to the accumulation of O, Al, Si, N, and Mn.

- Using the electrochemical technique of RPL, it was found out that the best corrosion behavior was developed in the horizontal samples than for the vertical ones. This could be because according to the tests, the SLMed 316L surfaces developed an initial passive-active behavior due to a corrosion film formed after the cutting process. At the same time, this oxide layer could form due to the interaction of the material with chloride-containing and acid solutions, similar to the oxide layers (Fe_2O_3 and Cr_2O_3) formed through the thermal oxidation (TO) process on an SLMed 316L SS in the literature.
- Through the electrochemical noise (EN) technique, the -1.65 and -0.012 skewness factors were calculated, which indicates that the SLMed specimens developed localized corrosion in NaCl, for the horizontal and vertical samples, respectively. The localized corrosion associated with the Cl ions attacked mainly the subgrains of the microstructure and, in some cases, defects such as pores. Although the initiation of metastable pits was found due to some pre-existing SLM defects (pores) on surfaces, it could not transition to stable growing pits, thanks to the corrosion film formed in the material. For the H_2O and H_2SO_4 electrolytes, the corrosion type was uniform for the two orientations, due to it developing over the entire surface of the samples. Besides, according to the EN parameters, it was determined that the best corrosion rate in H_2O was 1×10^{-5} mm/year for the horizontal samples compared with the value of 7×10^{-4} mm/year for the vertical ones. However, the XY samples presented a minor corrosion resistance than for the XZ samples both tested in the NaCl and H_2SO_4 electrolytes.
- The morphology identified by SEM was correlated with the results obtained from the electrochemical techniques, where it was observed that the pits developed within the subgrains due to the galvanic pair that developed between the Mo-enriched phases (subgrain boundaries) that were segregated during the fabrication.

7.2 Scientific contribution of this research work

It has developed an SLM model based on the LBM to predict the melt pool geometry for the manufacture of the AlSi10Mg and 316L SS alloys. Due to the melt pool influences the SLM accurate and efficiency, this numerical tool can give an initial idea about the SLM processing parameters needed to produce the desired melt pool dimensions. According to this, the cost of production, energy, characterization, and processing time can be reduced considerable.

The SLM model obtained by the lattice Boltzmann method can work like a fast and powerful tool to know the melt pool characteristics and thermal behavior of two important alloys (AlSi10Mg and 316L SS) processed by SLM, which are widely used for aeronautical applications such as brackets, sensors housing, etc.

The development of this numerical model for SLM can give qualitative and quantitative information for performing settings and recommendations in the processing parameters to optimize the process. With this model, it can be fixed a certain processing parameter and vary another up to it relates to the proper melt pool dimensions. For example, based on a known value of the laser power, it can be adjusted the scanning speed needed for the wanted purpose, maintaining other processing parameters constant, such as the exposure time, ambient temperature, etc. This will allow obtaining a successful SLM process in real-time.

7.3 Future work

In order to expand this research work and obtain the LBM model almost real to the SLM process, the following recommendations could be considered for future researches.

The numerical model of this work is developed as an initial LBM of SLM, which has not considered all the processing parameters such as laser movement, layer-by-layer material deposition as well as the substrate properties where the material is deposited.

For now, the developed LBM considers the thermo-physical properties of the medium as constants. Therefore, in order to obtain more accurate melt pool dimensions, the corresponding thermo-physical properties must be considered dependent on temperature, this should be a great improvement for the model.

The LBM for SLM developed during this work treats the medium in solid phase. So, an attractive alternative to keep improving the model is taking into account the phase transformations of solid, liquid, gas, or interface in the simulation domain. Based on literature, interface phase is considered as a phase that has at least one gas cell. This represents the transition zone between liquid and gas phase.

The LBM with the D2Q9 lattice structure for the SLM developed in the present research is still in 2D. An expansion using the D3Q15, or D3Q19 lattice structure to 3D could be performed. This will help to have more accurate results and the model will be almost real.

In order to obtain an enhanced model for the prediction of final properties during the selective laser melting aluminum and steel alloys, this method can be coupled with a Cellular Automata model for the prediction and control of the microstructure evolution during the process. The control of the microstructure and geometry of the melt pool from the processing parameters will allow manufacturing an SLM material with the desired properties such as mechanical strength, corrosion resistance, roughness, residual stresses, etc.

Additionally, based on a dimensionless expression for calculating an SLM parameter (laser power, scanning speed, etc.) as a function of the desired bulk density, obtained in the literature via dimensional analyses; it could be carried out the LBM calculations by using the set of processing parameters obtained by such dimensionless expressions. This will not only allow the comparison between the two approaches, but it could be monitoring the melt pool geometry as well as the thermal fields during the laser process. Besides, the knowledge of the thermal behavior plays an important role to predict the thermal variables such as temperature gradient, cooling rate, and solidification rate of the molten pool, which are important parameters for the control of the solidification process.

8 References

- [1] M. Zavala-Arredondo, N. Boone, J. Willmott, D.T.D. Childs, P. Ivanov, K.M. Groom, K. Mumtaz, Laser diode area melting for high speed additive manufacturing of metallic components, *Mater. Desig.* 117 (2017) 305–315.
- [2] O. Lopez-Botello, U. Martinez-Hernandez, J. Ramírez, C. Pinna, K. Mumtaz, Two-dimensional simulation of grain structure growth within selective laser melted AA-2024. *Mater. Desig.* 113, (2017) 369–376.
- [3] L.E. Murr, E. Martinez, K.N. Amato, S.M. Gaytan, J. Hernandez, D.A. Ramirez, P.W. Shindo, F. Medina, R.B. Wicker, Fabrication of metal and alloy components by additive manufacturing: Examples of 3D materials science, *J. Mater. Res. Technol.* 1 (2012) 42-54.
- [4] C.H. Fu, Y.B. Guo, Three-dimensional temperature gradient mechanism in selective laser melting of Ti-6Al-4V, *J. Manuf. Sci. Eng.* 136 (2014) 0610041 - 6100417.
- [5] C. Körner, E. Attar, P. Heinl, Mesoscopic simulation of selective beam melting processes, *J. Mater. Proc. Tech.* 211 (2011) 978–987.
- [6] W. Yan, W. Ge, J. Smith, S. Lin, O.L. Kafka, F. Lin, W.K. Liu, Multi-scale modeling of electron beam melting of functionally graded materials, *Acta Mater.* 115 (2016) 403-412
- [7] S.R. Ch, A. Raja, P. Nadig, R. Jayaganthan, N.J. Vasa, Influence of working environment and built orientation on the tensile properties of selective laser melted AlSi10Mg alloy, *Mater. Sci. Eng.* 750 (2019) 141–151.
- [8] R. Liu, Z. Wang, T. Sparks, F. Liou, J. Newkirk, Aerospace applications of laser additive

manufacturing, Elsevier (2016) 351-371.

- [9] N.T. Aboulkhair, I. Maskery, C. Tuck, I. Ashcroft, N.M. Everitt, On the formation of AlSi10Mg single tracks and layers in selective laser melting: Microstructure and nano-mechanical properties, *J. Mater. Proc. Tech.* 230 (2016) 88–98.
- [10] E. Zaretsky, A. Stern, N. Frage, Dynamic response of AlSi10Mg alloy fabricated by selective laser melting, *Mater. Sci. Eng.* 688 (2017) 364–370.
- [11] M. Leary, M. Mazur, J. Elambasseril, M. McMillan, T. Chirent, Y. Sun, M. Qian, M. Easton, M. Brandt, Selective laser melting (SLM) of AlSi12Mg lattice structures, *Mater. Desig.* (2016) 344–357
- [12] T. Kurzynowski, K. Gruber, W. Stopyra, B. Kuźnicka, E. Chlebus, Correlation between process parameters, microstructure and properties of 316L stainless steel processed by selective laser melting, *Mater. Sci. Eng.* 718 (2018) 64–73.
- [13] S. Liu, H. Zhu, G. Peng, J. Yin, X. Zeng, Microstructure prediction of selective laser melting AlSi10Mg using finite element analysis, *Mater. Des.* 142 (2018) 319–328.
- [14] W. Pei, W. Zhengying, C. Zhen, L. Junfeng, Z. Shuzhe, D. Jun, Numerical simulation and parametric analysis of selective laser melting process of AlSi10Mg powder, *Appl. Phys. A* (2017) 123-540.
- [15] X. Shi, S. Ma, C. Liu, Q. Wu, Parameter optimization for Ti-47Al-2Cr-2Nb in selective laser melting based on geometric characteristics of single scan tracks, *Opt. Laser Technol.* 90 (2017) 71–79.

- [16] G. Kasperovich, J. Haubrich, J. Gussone, G. Requena, Correlation between porosity and processing parameters in TiAl6V4 produced by selective laser melting, *Mater. Desig.* 105 (2016) 160–170.
- [17] H. Rao, S. Giet, K. Yang, X. Wu, C.H.J. Davies, The influence of processing parameters on aluminium alloy A357 manufactured by selective laser melting, *Mater. Desig.* 109 (2016) 334–346.
- [18] L. Rickenbacher, T. Etter, S. Hovel, High temperature material properties of IN738LC processed by selective laser melting (SLM) technology, *Rapid Prototyp. J.* 19 (2013) 282–290.
- [19] M. Leary, M. Mazur, H. Williams, E. Yang, A. Alghamdi, B. Lozanovski, X. Zhang, D. Shidid, L. Farahbod-Sternahl, G. Witt, I. Kelbassa, P. Choong, M. Qian, M. Brandt, Inconel 625 lattice structures manufactured by selective laser melting (SLM): Mechanical properties, deformation and failure modes. *Jmade* (2017), doi:10.1016/j.matdes.2018.06.010
- [20] L.E. Criales, Y.M. Arisoy, B. Lane, S. Moylan, A. Donmez, T. Özel, Laser powder bed fusion of nickel alloy 625: Experimental investigations of effects of process parameters on melt pool size and shape with spatter analysis, *Int. J. Mach. Tools Manuf.* 121 (2017) 22–36.
- [21] C. Li, R. White, X.Y. Fang, M. Weaver, Y.B. Guo, Microstructure evolution characteristics of Inconel 625 alloy from selective laser melting to heat treatment, *Mater. Sci. Eng. A* 705 (2017) 20–31.
- [22] I. Koutiri, E. Pessard, P. Peyre, O. Amlou, T. De Terris, Influence of SLM process parameters on the surface finish, porosity rate and fatigue behavior of as-built Inconel 625 parts, *J. Mater. Proc. Tech.* (2010), <https://doi.org/10.1016/j.jmatprotec.2017.12.043>.

- [23] N.T. Aboulkhair, N.M. Everitt, I. Ashcroft, C. Tuck, Reducing porosity in AlSi10Mg parts processed by selective laser melting, *Addit. Manuf.* 1–4 (2014) 77–86.
- [24] W. Li, S. Li, J. Liu, A. Zhang, Y. Zhou, Q. Wei, C. Yan, Y. Shi, Effect of heat treatment on AlSi10Mg alloy fabricated by selective laser melting: Microstructure evolution, mechanical properties and fracture mechanism, *Mater. Sci. Eng. A* 663 (2016) 116–125.
- [25] N.T. Aboulkhair, I. Maskery, C. Tuck, I. Ashcroft, N.M. Everitt, The microstructure and mechanical properties of selectively laser melted AlSi10Mg: The effect of a conventional T6-like heat treatment, *Mater. Sci. Eng. A* 667 (2016) 139–146.
- [26] J. Wu, X.Q. Wang, W. Wang, M.M. Attallah, M.H. Loretto, Microstructure and strength of selectively laser melted AlSi10Mg, *Acta Mater.* 117 (2016) 311–320.
- [27] B. Song, Q. Yan, Y. Shi, Comparative study of performance comparison of AlSi10Mg alloy prepared by selective laser melting and casting, *J. Mater. Sci. Technol.* (2019), doi: <https://doi.org/10.1016/j.jmst.2019.08.049>
- [28] L.E. Loh, C.K. Chua, W.Y. Yeong, J. Song, M. Mapar, S.L. Sing, Z.H. Liu, D.Q. Zhang, Numerical investigation and an effective modelling on the selective laser melting (SLM) process with aluminium alloy 6061, *Int. J. Heat Mass Transf.* 80 (2015) 288–300.
- [29] J. Liu, Q. Sun, C. Zhou, X. Wang, H. Li, K. Guo, J. Sun, Achieving Ti6Al4V alloys with both high strength and ductility via selective laser melting, *Mater. Sci. Eng. A* 766 (2019) 138319.
- [30] H. Ali, H. Ghadbeigi, K. Mumtaz, Effect of scanning strategies on residual stress and mechanical properties of selective laser melted Ti6Al4V, *Mater. Sci. Eng. A* 712 (2018)

175–187.

- [31] A. Rai, H. Helmer, C. Körner, Simulation of grain structure evolution during powder bed based additive manufacturing, *Addit. Manuf.* 13 (2017) 124–134.
- [32] A. Rai, M. Markl, C. Körner, A coupled cellular automaton–lattice Boltzmann model for grain structure simulation during additive manufacturing, *Comput. Mater. Sci.* 124 (2016) 37–48.
- [33] A.R. Ansari, W.S. Hwang, W.C. Huang, T.W. Tsai, Determination and controlling of grain structure of metals after laser incidence : Theoretical approach, *Nat. Publ. Gr.* 1 (2017) 1–11.
- [34] P. Gao, W. Huang, H. Yang, G. Jing, Q. Liu, G. Wang, Z. Wang, X. Zeng, Cracking behavior and control of α -solidifying Ti-40Al-9V-0.5Y alloy produced by selective laser melting, *J. Mater. Sci. Technol.* (2019), doi: <https://doi.org/10.1016/j.jmst.2019.08.026>
- [35] Y. Li, D. Gu, Parametric analysis of thermal behavior during selective laser melting additive manufacturing of aluminum alloy powder, *Mater. Desig.* 63 (2014) 856–867.
- [36] M. Zheng, L. Wei, J. Chen, Q. Zhang, C. Zhong, X. Lin, W. Huang, A novel method for the molten pool and porosity formation modelling in selective laser melting, *Int. J. Heat Mass Transf.* 140 (2019) 1091–1105.
- [37] A. Großmann, J. Felger, T. Frölich, J. Gosmann, C. Mittelstedt, Melt pool controlled laser powder bed fusion for customised low-density lattice structures, *Mater. Desig.* 181 (2019) 108054
- [38] A. Großmann, J. Möllene, T. Frölich, H. Merschroth, J. Felger, M. Weigold, A. Sielaff, C.

Mittelstedt, Dimensionless process development for lattice structure design in laser powder bed fusion, *Mater. Desig.* (2020), <https://doi.org/10.1016/j.matdes.2020.108952>

- [39] Y. Yang, A. Großmann, P. Kuhn, J. Möllene, L. Kropholler, C. Mittelstedt, B.X. Xu, Validated dimensionless scaling law for melt pool width in laser powder bed fusion, *J. Mater. Process. Tech.* (2021), doi: <https://doi.org/>
- [40] J.A. Estrada-Díaz, A. Elías-Zúñiga, O. Martínez-Romero, J. Rodríguez-Salinas, D. Olvera-Trejo, A mathematical dimensional model for predicting bulk density of Inconel 718 parts produced by selective laser melting, *Mater.* 14(3) (2021), 1-20 512, <https://doi.org/10.3390/ma14030512>
- [41] J.A. Estrada-Díaz, A. Elías-Zúñiga, O. Martínez-Romero, D. Olvera-Trejo, Enhanced mathematical model for producing highly dense metallic components through selective laser melting, *Mater.* 14(6) (2021) 1571, <https://doi.org/10.3390/ma14061571>
- [42] K. Antony, N. Arivazhagan, K. Senthilkumaran, Numerical and experimental investigations on laser melting of stainless steel 316L metal powders, *J. Manuf Process* (2014).
- [43] M. Matthews, J. Trapp, G. Guss, A. Rubenchik, Direct measurements of laser absorptivity during metal melt pool formation associated with powder bed fusion additive manufacturing processes, *J. Laser Appl.* 30, 032302 (2018); doi: 10.2351/1.5040636
- [44] X.C. Wang, T. Laoui, J. Bonse, J.P. Kruth, B. Lauwers, L. Froyen, Direct selective laser sintering of hard metal powders: experimental study and simulation, *Int. J. Adv. Manuf. Technol.* (2002) 19:351–357.
- [45] Z. Dong, Y. Liu, W. Li, J. Liang, Orientation dependency for microstructure, geometric

accuracy and mechanical properties of selective laser melting AlSi10Mg lattices, *J. Alloys Compd.* 791 (2019) 490-500.

- [46] Z. Xiong, Z. Li, Z. Sun, S. Hao, Y. Yang, M. Li, C. Song, P. Qiu, L. Cui, Selective laser melting of NiTi alloy with superior tensile property and shape memory effect, *J. Mater. Sci. Technol.* 35 (2019) 2238–2242.

- [47] B. Mondal, S.C. Mishra, Lattice Boltzmann method applied to the solution of the energy equations of the transient conduction and radiation problems on non-uniform lattices, *Int. J. Heat Mass Transf.* (2008) 68–82.

- [48] A.A. Mohamad, Lattice Boltzmann method fundamentals and engineering applications with computer codes, Springer, London, Dordrecht, Heidelberg, New York 2011.

- [49] Ł. Łach, D. Svyetlichnyy, R. Straka, Heat flow model based on lattice Boltzmann method for modeling of heat transfer during phase transformation, *Int. J. Numer. Meth. Fluid Flow* 2255–2271, (2020) 2255–2271.

- [50] B. Blais, J.M. Tucny, D. Vidal, F. Bertrand, A Conservative lattice Boltzmann model for the volume-averaged Navier-Stokes equations based on a novel collision operator, *J. Comput. Phys.* (2015) <http://dx.doi.org/10.1016/j.jcp.2015.03.036>.

- [51] L. Li, R. Mei, J.F. Klausner, Lattice Boltzmann models for the convection-diffusion equation : D2Q5 vs D2Q9, *Int. J. Heat Mass Transf.* 108 (2017) 41–62.

- [52] R. Chaabane, F. Askri, S.B. Nasrallah, Application of the lattice Boltzmann method for solving conduction problems with heat flux boundary condition, *International Renewable Energy Congress* (2009) 120–124.

- [53] M. Szucki, J.S. Suchy, J. Leito, P. Malinowski, J. Sobczyk, Application of the lattice Boltzmann method for simulation of the mold filling process in the casting industry, *Heat Mass Transfer* (2017) 3421–3431.
- [54] N.I. Prasianakis, I.V. Karlin, Lattice Boltzmann method for thermal flow simulation on standard lattices, *Phys. Rev.* (2007) 1–11.
- [55] E. Walther, R. Bennacer, C. De Sa, Lattice Boltzmann method and diffusion in materials with large diffusivity ratios, *Thermal Science* (2017) 1173–1182.
- [56] M.V. Elsen, F. Al-Bender, J.P. Kruth, Application of dimensional analysis to selective laser melting, *Rapid Prototyp. J.* (2008) 15–22.
- [57] T. Mukherjee, V. Manvatkar, A. De, T. DebRoy, Dimensionless numbers in additive manufacturing, *J. Appl. Phys.* 121 (2017) 064904.
- [58] S.C. Mishra, A. Lankadasu, K.N. Beronov, Application of the lattice Boltzmann method for solving the energy equation of a 2-D transient conduction-radiation problem, *Int. J. Heat Mass Transf.* (2005) 3648–3659.
- [59] S.C. Mishra, H.K. Roy, Solving transient conduction and radiation heat transfer problems using the lattice Boltzmann method and the finite volume method, *J. Comput. Phys.* 223 (2007) 89–107.
- [60] W.S. Jiaung, J.R. Ho, C.P. Kuo, Lattice Boltzmann method for the heat conduction problem with phase, *Numer. Heat Transfer* (2010) 37–41.
- [61] R. Das, S.C. Mishra, M. Ajith, R. Uppaluri, An inverse analysis of a transient 2-D

conduction–radiation problem using the lattice Boltzmann method and the finite volume method coupled with the genetic algorithm, *Journal of Quantitative Spectroscopy and Radiative Transfer* 109 (2008) 2060–2077.

- [62] S.J. Almalawi, A. Oztekin, Flow simulations using two dimensional thermal lattice Boltzmann method, *J. Appl. Mathematics* (2012) doi:10.1155/2012/135173.
- [63] M. Eshraghi, S.D. Felicelli, An implicit lattice Boltzmann model for heat conduction with phase change, *Int. J. Heat Mass Transf.* (2012) 2420–2428.
- [64] Y.S. Xu, R.M. Wang, G.N. Li, Y.Q. Zheng, Numerical simulation of driven convective heat transfer based lattice Boltzmann method in a Porous Cavity, *J. Chemistry* (2015) doi.org/10.1155/2015/710341.
- [65] R. Hamila, R. Chaabane, F. Askri, A. Jemni, S.B. Nasrallah, Lattice Boltzmann method for heat transfer problems with variable thermal conductivity, *Int. J. Heat Technol.* (2017) 313–324.
- [66] H. Hu, X. Ding, L. Wang, Numerical analysis of heat transfer during multi-layer selective laser melting of AlSi10Mg, *Int. J. Light Electron Opt.* (2016) 8883–8891.
- [67] F.R. Liu, Q. Zhang, W.P. Zhou, J.J. Zhao, J.M. Chen, Micro scale 3D FEM simulation on thermal evolution within the porous structure in selective laser sintering, *J. Mater. Process. Tech.* (2012) 2058–2065.
- [68] C. Tang, J.L. Tan, C.H. Wong, A numerical investigation on the physical mechanisms of single track defects in selective laser melting, *Int. J. Heat Mass Transf.* (2018) 957–968.

- [69] D. Kandhai, D.J.E. Vidal, A.G. Hoekstra, H. Hoefsloot, P. Iedema, P.M.A. Sloop, A comparison between Lattice-Boltzmann and finite-element simulations of fluid flow in static mixer reactors, *Int. J. Modern Phys.* (1998) 1123–1128.
- [70] D. Kong, X. Ni, C. Dong, L. Zhang, C. Man, J. Yao, K. Xiao, X Li, Heat treatment effect on the microstructure and corrosion behavior of 316L stainless steel fabricated by selective laser melting for proton exchange membrane fuel cells, *Electrochim. Acta* 276 (2018) 293–303. <https://doi.org/10.1016/j.electacta.2018.04.188>
- [71] J. Nie, L. Wei, Y. Jiang, Q. Li, H. Luo, Corrosion mechanism of additively manufactured 316 L stainless steel in 3.5 wt.% NaCl solution, *Materials Today Communications* (2020), doi: <https://doi.org/10.1016/j.mtcomm.2020.101648>
- [72] C. Zhou, S. Hu, Q. Shi, H. Tao, Y. Song, J. Zheng, P. Xu, L. Zhang, Improvement of corrosion resistance of SS316L manufactured by selective laser melting through subcritical annealing, *Corros. Sci.* (2019), doi: <https://doi.org/10.1016/j.corsci.2019.108353>
- [73] Z. Duan, C. Man, C. Dong, Z. Cui, D. Kong, L. Wang, X. Wang, Pitting behavior of SLM 316L stainless steel exposed to chloride environments with different aggressiveness: Pitting mechanism induced by gas pores, *Corros. Sci.* 167 (2020) 108520, <https://doi.org/10.1016/j.corsci.2020.108520>
- [74] D. Serafin, T. Bartkowiak, W.J. Nowak, B. Wierzba, Influence of microgeometry of iron surface on the oxidation process – a comparison of multiscale geometric methods and their applicability, *Appl. Surf. Sci.* (2020), doi: <https://doi.org/10.1016/j.apsusc.2020.146838>
- [75] K. Geenen, A. Röttger, W. Theisen, Corrosion behavior of 316L austenitic steel processed by selective laser melting, hot-isostatic pressing, and casting, *Mater. Corros.* 68 (7) (2017)

- [76] L. Jinlong, Y. Meng, L. Tongxiang, The effect of surface enriched chromium and grain refinement by ball milling on corrosion resistance of 316L stainless steel, *Materials Research*, <http://dx.doi.org/10.1016/j.materresbull.2017.03.022>
- [77] A.H. Etefagh, S. Guo, Electrochemical behavior of AISI316L stainless steel parts produced by laser-based powder fusion process and the effect of post annealing process, *Addit. Manuf.* 22 (2018) 153-156. <https://doi.org/10.1016/j.addma.2018.05.014>
- [78] M.J.K. Lodhi, K.M. Deen, W. Haider, Corrosion behavior of additively manufactured 316L stainless steel in acidic media, *Materialia* 2 (2018) 111-121. <https://doi.org/10.1016/j.mtla.2018.06.015>
- [79] G. Sander, S. Thomas, V. Cruz, M. Jurg, N. Birbilis, X. Gao, M. Brameld, C.R. Hutchinson, On the corrosion and metastable pitting characteristics of 316L stainless steel produced by selective laser melting, *J. Electrochem. Soc.* 164 (6) (2017) 250-257. DOI: 10.1149/2.0551706jes
- [80] J.R. Trelewicz, G.P. Halada, O.K. Donaldson, G. Manogharan, Microstructure and corrosion resistance of laser additively manufactured 316L stainless steel, *JOM* 68, 3 (2016) 850–859. DOI: 10.1007/s11837-016-1822-4
- [81] Y. Sun, A. Moroz, K. Alrbaey, Sliding wear characteristics and corrosion behaviour of selective laser melted 316L stainless steel, *J. Mater. Eng. Perform.* 23 (2014) 518-526. DOI: 10.1007/s11665-013-0784-8

- [82] Q. Chao, V. Cruz, S. Thomas, N. Birbilis, P. Collins, A. Taylor, P.D. Hodgson, D. Fabijanic, On the enhanced corrosion resistance of a selective laser melted austenitic stainless steel, *Scripta Mater.* 141 (2017) 94-98. <http://dx.doi.org/10.1016/j.scriptamat.2017.07.037>
- [83] W.S.W. Harun, R.I.M. Asri, F.R.M. Romlay, S. Sharif, N.H.M. Jan, F. Tsumori, Surface characterisation and corrosion behaviour of oxide layer for SLMed-316L stainless steel, *J. Alloys Compd.* 748 (2018) 1044-1052. <https://doi.org/10.1016/j.jallcom.2018.03.233>
- [84] Z. Li-jun, Z. Xu-bei, Z. Zhao, Z. Jian-qing, Electrochemical noise characteristics in corrosion process of AZ91D magnesium alloy in neutral chloride solution, *Trans. Nonferrous Met. Soc. China* 19 (2009) 496-503. DOI: 10.1016/S1003-6326(08)60302-7
- [85] C. Gaona-Tiburcio, M.R. Aguilar L, P. Zambrano Robledo, F. Estupiñán López, J.A. Cabral Miramontes, D. Nieves-Mendoza, E. Castillo-González, F. Almeraya-Calderón, Electrochemical Noise Analysis of Nickel Based Superalloys in Acid Solutions, *Int. J. Electrochem. Sci.* 9 (2014) 523-533.
- [86] ASTM International. ASTM G59-972014. Standard Test Method for Conducting Potentiodynamic Polarization Resistance Measurements; ASTM International: West Conshohocken, PA, USA, (2014). Available online: www.astm.org (accessed on 8 March 2021).
- [87] ASTM International. ASTM G199-092014. Standard Guide for Electrochemical Noise Measurement; ASTM International: West Conshohocken, PA, USA, (2014). Available online: www.astm.org (accessed on 8 March 2021).

- [88] S.A. Khairallah, A.T. Anderson, A. Rubenchik, W.E. King, Laser powder-bed fusion additive manufacturing: Physics of complex melt flow and formation mechanisms of pores, spatter, and denudation zones, *Acta Mater.* (2016) 36–45.
- [89] K. Saeidi, X. Gao, F. Lofaj, L. Kvetkova, Z.J. Shen, Transformation of austenite to duplex austenite-ferrite assembly in annealed stainless steel 316L consolidated by laser melting, *J. Alloys Compd.* 633 (2015) 463-469. <http://dx.doi.org/10.1016/j.jallcom.2015.01.249>
- [90] D. Wang, C. Song, Y. Yang, Y. Bai, Investigation of crystal growth mechanism during selective laser melting and mechanical property characterization of 316L stainless steel parts, *Mater. Desig.* 100 (2016) 291-299. <http://dx.doi.org/10.1016/j.matdes.2016.03.111>
- [91] ASTM International. ASTM G102-892015e1. Calculation of Corrosion Rates and Related Information from Electrochemical Measurements; ASTM International: West Conshohocken, PA, USA, (2015). Available online: www.astm.org (accessed on 8 March 2021).
- [92] M. Sanchez-Carrillo, J.P. Flores-de los Rios, C.G. Nava-Dino, H. Flores-Zuñiga, R. Narro-Garcia, M.C. Maldonado-Orozco, F.H. Estupiñan-Lopez, J.G. Chacon-Nava, Transformation temperatures and electrochemical behavior of Polycrystalline Fe-Doped Ni-Mn-Ga and Co-Ni-Ga alloys, *Int. J. Electrochem. Sci.* 13 (2018) 6666–6675. doi: 10.20964/2018.07.08 Received:
- [93] Z. Sun, X. Tan, S.B. Tor, C.K. Chua, Simultaneously enhanced strength and ductility for 3D-printed stainless steel 316L by selective laser melting, *NPG Asia Mater.* 10 (2018) 127–136. DOI 10.1038/s41427-018-0018-5
- [94] F. Andreatta, A. Lanzutti, E. Vaglio, G. Totis, M. Sortino, L. Fedrizzi, Corrosion behaviour

of 316L stainless steel manufactured by selective laser melting, *Mater. Corros.* (2019) 1-13, DOI: 10.1002/maco.201910792

- [95] G. Sander, S. Thomas, V. Cruz, M. Jurg, N. Birbilis, X. Gao, M. Brameld, C.R. Hutchinson, On the corrosion and metastable pitting characteristics of 316L stainless steel produced by selective laser melting. *J. Electrochem. Soc.* (2017), 164, 250–257.
- [96] R.A. Cottis, Interpretation of electrochemical noise data, *Corrosion–Vol. 57*, No. 3 (2001), Nace International, 265-285.
- [97] M. Ziętała, T. Durejko, M. Polański, I. laKunce, T. Płociński, W. Zieliński, M. Łazińska, W. Stępniewski, T. Czujko, K.J. Kurzydłowski, Z. Bojar, The microstructure, mechanical properties and corrosion resistance of 316L stainless steel fabricated using laser engineered net shaping, *Mater. Sci. Eng. A* 677 (2016) 1–10, <http://dx.doi.org/10.1016/j.msea.2016.09.028>
- [98] K. Saeidi, X. Gao, Y. Zhong, Z.J. Shen, Hardened austenite steel with columnar sub-grain structure formed by laser melting, *Mater. Sci. Eng. A* 625 (2015) 221–229, <http://dx.doi.org/10.1016/j.msea.2014.12.018>

APPENDIX 1

In this part, it is presented the two LBM codes for the SLM process of the AlSi10Mg and 316L SS alloys. These codes were developed by the commercial Matlab software.

SLM AlSi10Mg simulation by FDM

```
clear all
clc
%-----START_TIME = CLOCK
tic
%%%%%%%%%%%%%%%%%%%%%%%%%%%%%%%%%%%%%%%%%%%%%%%%%%%%%%%%%%%%%%%%%%%%%%%%
%2D FDM MODEL FOR SLM AlSi10Mg L0S1
%%%%%%%%%%%%%%%%%%%%%%%%%%%%%%%%%%%%%%%%%%%%%%%%%%%%%%%%%%%%%%%%%%%%%%%%
%-----PARAMETERS FOR MODEL GENERATION
PBL = 1000e-6; %POWDER BED LENGTH (m)
SH = 500e-6; %SUBSTRATE HIGH (m)
LH = 30e-6; %LAYER HIGH (m)
LN = 0; %LAYER NUMBER
D = 80e-6; %BEAM DIAMETER (m)
SIT = 1e-4; %SPOT IRRADIATION TIME (s)
RT = 5e-2; %RECOATING TIME (s)
PD = 20e-6; %PD PHYSICAL (m)
Spots = 1; %NUM. SPOTS
dx2 = 10e-6; %dx PHYSICAL (m)
dy2 = 10e-6; %dy PHYSICAL (m)

PBH = SH + LN*LH; %POWDER BED HIGH (m)
RL = D + (Spots-1)*PD; %RASTER LENGTH (m)
%-----PARAMETERS IN FDM
dt = 0.2e-6; %s
dx = 10e-6; %m
dy = 10e-6; %m
mstep = 500; %TIME STEPS FOR LASER IRRADIATION (SIT)
mcstep = 250000; %TIME STEPS FOR INITIAL CONVECTION (RT)
vall = 1; %NUM.VALUES FOR PLOTTING CONVECTION
val2 = 1; %NUM.VALUES FOR PLOTTING IRRADIATION

m = int16(PBL/dx);
n = int16(PBH/dx);
RLC = RL/dx; %RASTER LENGTH CELLS
X0 = (m/2+1) - RLC/2; %INITIAL X0 SPOT CELLS
%-----PARAMETERS FOR LASER POSITION
XCS = zeros(1,Spots);
for SN=1:Spots
    XL = X0 + (SN-1)*(PD/dx);
    XR = X0 + (SN-1)*(PD/dx) + D/dx;
    XC = XL + ((XR-XL)/2);
    XCS(1,SN) = XC;
end
%-----PHYSICAL PROPERTIES
alpha = 7.53e-5; %THERMAL DIFUSIVITY PHYSICAL (m2/s)
density = 2650; %DENSITY (kg/m3)
```

```

Cp = 797; %SPECIFIC HEAT CAPACITY (J/kg K)
TC = 0; %CONVECTION TIME CONTROL
TCS = 0; %CONVECTION TIME STEP
TI = 0; %LASER IRRADIATION TIME CONTROL
PWR = 100; %LASER POWER (W)
LEA = 0.09; %LASER ENERGY ABSORPTIVITY
GC = 0.865; %GAUSSIAN CONSTANT
Aspot = (pi*D*D)/4; %SPOT AREA (m2)
Aspot2 = D; %SPOT AREA (m2)
Heatflux = LEA*GC*PWR/Aspot; %HEAT FLUX (W/m2)
Volflux = PWR/(Aspot*dy/2); %VOLUMETRIC HEAT FLUX (W/m3)
tk = 159; %THERMAL CONDUCTIVITY (W/m K)
chtc = 20; %CONVECTIVE TRANSFER COEFFICIENT (W/m2 K)
ta = 25+273; %ROOM TEMPERATURE 25°C
TL = 869; %LIQUIDS TEMPERATURE
IT = 200+273; %POWDER BED TEMPERATURE 25°C
Twall = 200+273; %TEMPERATURE AT THE WALLS
TG = 700; %TEMPERATURE FOR CONTOURF
%-----VERIFY VALUES
VALUE = ['verify: m = ', num2str(m), ' n = ', num2str(n), ' mstep = ',
num2str(mstep), ' mcstep = ', num2str(mcstep)];
disp(VALUE)
%-----INITIAL CONDITIONS & VARIABLES DEFINITION
fo = zeros(n+1, m+1);
f = zeros(n+1, m+1);
for j=1:n+1
    for i=1:m+1
        fo(j,i) = IT;
        if(i==1)
            fo(j,i) = Twall;
        end
        if(i==m+1)
            fo(j,i) = Twall;
        end
        if(j==n+1)
            fo(j,i) = Twall;
        end
    end
end
end
%-----VARIABLES FOR LISTTING RESULTS
fS = zeros(n+1,m+1); %f FOR EACH SPOT
fCSP = zeros(n+1,Spots); %f OF PBL/2, STARTING AT THE SPOT CENTER
fTT = zeros(Spots*(mstep/vall),Spots); %f OVER TIME (TI)
fTI = zeros((mstep/vall),Spots); %f OF IRRADIATION TIME (SPOT CENTER)
MP = zeros((mstep/vall),1); %MELTING POINT
TIME = zeros((mstep/vall),1); %SIMULATION TIME
fTTS1 = zeros((mstep/vall),1); %f OF SPOT 1
%-----Do LN = 1 (NO DEPOSITION) FOR CALCULATING VARIABLES
LN = 1;
for kk=1:LN %LOOP FOR LAYERS DEPOSITION FROM "kk" to "LN"
    PBHLD = (((LN-kk)*LH)/dx)+1;
    PBHLY = PBH-((LN-kk)*LH);
    x = 0:dx:PBL;
    y = PBHLY:-dy:0;
    [x, y]=meshgrid(x,y);
    fp = zeros(n+2-PBHLD,m+1);
    %////////////////////////////////////

```

```

%//////////LOOP FOR SPOTS//////////
%//////////
for SN=1:Spots %LOOP FOR SPOTS FROM "SN" to "Spots"
    XL = X0 + (SN-1)*(PD/dx);
    XR = X0 + (SN-1)*(PD/dx) + D/dx;
    XC = XL + ((XR-XL)/2);
    for tstep=1:mstep %LOOP FOR SPOT IRRADIATION TIME
        for i=2:m
            for j=PBHLD+1:n
                termx = (fo(j+1,i)+fo(j-1,i))/(dx*dx);
                termy = (fo(j,i-1)+fo(j,i+1))/(dy*dy);
                dd = (1/(dx*dx))+1/(dy*dy));
                f(j,i) = fo(j,i) + dt*alpha*(termx+termy-
2*fo(j,i)*dd);
            end
        end
        %-----BOUNDARY CONDITIONS
        %-----TEMPERATURE OF Twall AT THE LEFT AND RIGTH SIDES
        for j=n+1:-1:PBHLD
            f(j,1) = Twall;
            f(j,m+1) = Twall;
        end
        %-----TEMPERATURE OF Twall AT THE BUTTOM SIDE
        for i=2:m
            f(n+1,i) = Twall;
        end
        %-----CONVECTION & LASER IRRADIATION
        for i=m:-1:2
            CTE = (alpha*dt)/(dx*dx);
            CTE2 = tk / (tk+(chtc*dy)); %Acc to Kaluza G.
            CTE3 = (chtc*dy)/(tk+(chtc*dy)); %Acc to Kaluza G.
            if i > XR %FROM m TO XL+1 FOR CONVECTION
                %Shen, B. OK
                f(PBHLD,i)=CTE*(fo(PBHLD,i+1)+fo(PBHLD,i-
1)+fo(PBHLD+1,i))+(1-3*CTE)*fo(PBHLD,i)+CTE*(chtc*dx*(ta-
fo(PBHLD,i))/tk);
            end
            if i <= XR && i >= XL %FROM XL TO XR FOR THE HEAT FLUX
                %Shen, B. OK
                f(PBHLD,i)=CTE*(fo(PBHLD,i+1)+fo(PBHLD,i-
1)+fo(PBHLD+1,i))+(1-3*CTE)*fo(PBHLD,i)+CTE*(Heatflux*dx/tk);
            end
            if i < XL %FROM XR-1 TO 2 FOR CONVECTION
                %Shen, B. OK
                f(PBHLD,i)=CTE*(fo(PBHLD,i+1)+fo(PBHLD,i-
1)+fo(PBHLD+1,i))+(1-3*CTE)*fo(PBHLD,i)+CTE*(chtc*dx*(ta-
fo(PBHLD,i))/tk);
            end
        end
        %-----UPDATE fo
        for j=PBHLD:n+1
            for i=1:m+1
                fo(j,i) = f(j,i);
                fp(j-PBHLD+1,i) = fo(j,i);
            end
        end
        %-----SAVE IRRADIATION RESULTS

```

```

TI = TC + ((SN-1)*SIT + tstep*dt);
if (mod(tstep, val2) == 0)
    figure(1)
    contourf( x, y, fp);
    axis equal;
    title('Temperatura','FontSize',16);
    xlabel('x [unidades]','FontSize',16);
    ylabel('y [unidades]','FontSize',16);
    drawnow;
    %-----f VS TIME AT THE CENTER OF EACH SPOT
    TIIS = (SN-1)*(mstep/val2) + (tstep/val2);
    TIS = TCS + TIIS;
    TIME(TIS,1) = TI;
    fTT(TIIS,1,kk) = f(PBHL,D,XCS(1));
    fTTS1(TIS,1) = f(PBHL,D,XCS(1));
    fTI(tstep/val2,SN,kk) = f(PBHL,D,XC);
    MP(TIS,1) = TL;
end
end %END OF SPOT IRRADIATION TIME
%-----RESULTS AT THE SPOT CENTER
for j=PBHL,D:n+1
    fCSP(j-PBHL,D+1,SN) = f(j,XC);
end
%-----f DURING EACH SPOT
for j=PBHL,D:n+1
    for i=1:m+1
        fS(j-PBHL,D+1,i) = f(j,i);
    end
end
end %END OF SPOTS
end %END OF LAYER DEPOSITION
%-----END_TIME = CLOCK;
toc
disp(TI)
Tmax = max(fCSP);
%-----PARAMETERS FOR CHECKING RESULTS kk=0
LN = 0;
kk = 0;
PBHL,D = ((LN-kk)*LH)/dx)+1;
PBHL,Y = PBH-((LN-kk)*LH);
x1 = 0:dx:PBL;
y1 = PBHL,Y:-dy:0;
[x1, y1]=meshgrid(x1,y1);
fL0S1 = zeros(n+2-PBHL,D,m+1);
for j=1:n+2-PBHL,D
    for i=1:m+1
        fL0S1(j,i) = fS(j,i,1);
    end
end
end
%-----LIST AND CHECK RESULTS AT XC (L1 ALSO APPLY FOR L0)
fmiddleL0S1 = zeros(n+2-PBHL,D,1);
for j=1:n+2-PBHL,D
    fmiddleL0S1(j,1) = fL0S1(j,XC(1));
end
%-----PLOT AND CHECK RESULTS
%-----T vs y fmiddleL0S1
figure(2)

```

```

plot (y1, fmiddleL0S1, '-g', 'LineWidth',2.00);
hold on;
xlabel('y (m)', 'FontSize',16, 'FontName', 'Times');
ylabel('T (K)', 'FontSize',16, 'FontName', 'Times');
legend({'SPOT 1'});
lgd = legend;
lgd.FontSize = 9;
box on;

```

SLM AlSi10Mg simulation by LBM

```

clear all
clc
%-----START_TIME = CLOCK
tic
%%%%%%%%%%%%%%%%%%%%%%%%%%%%%%%%%%%%%%%%%%%%%%%%%%%%%%%%%%%%%%%%%%%%%%%%
%2D LBM MODEL FOR SLM AlSi10Mg L0S1
%%%%%%%%%%%%%%%%%%%%%%%%%%%%%%%%%%%%%%%%%%%%%%%%%%%%%%%%%%%%%%%%%%%%%%%%
%-----PARAMETERS FOR MODEL GENERATION
PBL = 1000e-6; %POWDER BED LENGTH (m)
SH = 500e-6; %SUBSTRATE HIGH (m)
LH = 30e-6; %LAYER HIGH (m)
LN = 0; %LAYER NUMBER
D = 80e-6; %BEAM DIAMETER (m)
SIT = 1e-4; %SPOT IRRADIATION TIME (s)
RT = 5e-2; %RECOATING TIME (s)
PD = 20e-6; %PD PHYSICAL (m)
Spots = 1; %NUM. SPOTS
dx2 = 10e-6; %dx PHYSICAL (m)
dy2 = 10e-6; %dy PHYSICAL (m)

PBH = SH + LN*LH; %POWDER BED HIGH (m)
RL = D + (Spots-1)*PD; %RASTER LENGTH (m)
%-----PARAMETERS IN LBM
dt = 1; %dt in LB
dx = 1; %dx in LB
dy = 1; %dy in LB
mstep = 456; %TIME STEPS FOR LASER IRRADIATION (SIT)
mcstep = 75282; %TIME STEPS FOR INITIAL CONVECTION (RT)
val1 = 1; %NUM.VALUES FOR PLOTTING CONVECTION
val2 = 1; %NUM.VALUES FOR PLOTTING IRRADIATION
dtc = RT/mcstep; %dte (s)
dti = SIT/mstep; %dti (s)

m = int16(PBL/dx2);
n = int16(PBH/dx2);
RLB = RL/dx2; %RASTER LENGTH LATTICE
X0 = (m/2+1) - RLB/2; %INITIAL X0 SPOT LATTICE
%-----PARAMETERS FOR LASER POSITION
XCS = zeros(1,Spots);
for SN=1:Spots
    XL = X0 + (SN-1)*(PD/dx2);
    XR = X0 + (SN-1)*(PD/dx2) + D/dx2;
    XC = XL + ((XR-XL)/2);
    XCS(1,SN) = XC;
end

```

```

%-----PHYSICAL PROPERTIES
alphaP = 7.53e-5; %THERMAL DIFUSIVITY PHYSICAL (m2/s)
density = 2650; %DENSITY (kg/m3)
Cp = 797; %SPECIFIC HEAT CAPACITY (J/kg K)
TC = 0; %CONVECTION TIME CONTROL
TCS = 0; %CONVECTION TIME STEP
TI = 0; %LASER IRRADIATION TIME CONTROL
PWR = 100; %LASER POWER (W)
LEA = 0.09; %LASER ENERGY ABSORPTIVITY
GC = 0.865; %GAUSSIAN CONSTANT
Aspot = (pi*D*D)/4; %SPOT AREA (m2)
Aspot2 = D; %SPOT AREA (m2)
Heatflux = LEA*GC*PWR/Aspot; %HEAT FLUX (W/m2)
Volflux = PWR/(Aspot*dy2/2); %VOLUMETRIC HEAT FLUX (W/m3)
tk = 159; %THERMAL CONDUCTIVITY (W/m K)
chtc = 20; %CONVECTIVE TRANSFER COEFFICIENT (W/m2 K)
ta = 25+273; %ROOM TEMPERATURE 25°C
TL = 869; %LIQUIDS TEMPERATURE
IT = 200+273; %POWDER BED TEMPERATURE 200°C
Twall = 200+273; %TEMPERATURE AT THE WALLS
TG = 700; %TEMPERATURE FOR CONTOURF

%-----PARAMETERS FOR LB
alpha1 = 0.165; %DIFUSIVITY IN LB FOR IRRADIATION TIME
alpha2 = 0.5; %DIFUSIVITY IN LB FOR RECOATING TIME
ck = dx/dt; csq = ck*ck;
omega1 = 1/(3.0*alpha1/(dt*csq)+0.5); %Equation 3.10, solving for
omega. Notebook pp.23
Tao1 = 1/omega1;
omega2 = 1/(3.0*alpha2/(dt*csq)+0.5); %Equation 3.10, solving for
omega. Notebook pp.23
Tao2 = 1/omega2;

%-----VERIFY VALUES
VALUE = ['verify: m = ', num2str(m), ' n = ', num2str(n), ' mstep = ',
num2str(mstep), ' mcstep = ', num2str(mcstep), ' Tao1 = ', num2str(Tao1)
, ' Tao2 = ', num2str(Tao2)];
disp(VALUE)

%-----INITIAL CONDITIONS & VARIABLES DEFINITION
rho = zeros(n+1, m+1);
f = zeros(n+1, m+1, 9);
w = [4/9 1/9 1/9 1/9 1/9 1/36 1/36 1/36 1/36];
for j=n+1:-1:1
    for i=1:m+1
        sum = 0;
        for k=1:9
            f(j,i,k) = w(k)*IT;
            if (i==1)
                f(j,i,k) = w(k)*Twall;
            end
            if (i==m+1)
                f(j,i,k) = w(k)*Twall;
            end
            if (j==n+1)
                f(j,i,k) = w(k)*Twall;
            end
            sum = sum + f(j,i,k);
        end
        rho(j,i) = sum;
    end
end

```

```

end
end
%-----VARIABLES FOR LISTTING RESULTS
rhoS    = zeros(n+1,m+1); %rho FOR EACH SPOT
rhoCSP  = zeros(n+1,Spots); %rho OF PBL/2, STARTING AT THE SPOT CENTER
rhoTT   = zeros(Spots*(mstep/vall),Spots); %rho OVER TIME (TI)
rhoTI   = zeros((mstep/vall),Spots); %rho OF IRRADIATION TIME (SPOT
CENTER)
MP      = zeros((mstep/vall),1); %MELTING POINT
TIME    = zeros((mstep/vall),1); %SIMULATION TIME
rhoTTS1 = zeros((mstep/vall),1); %rho OF SPOT 1
%-----Do LN = 1 (NO DEPOSITION) FOR CALCULATING VARIABLES
LN = 1;
for kk=1:LN      %LOOP FOR LAYERS DEPOSITION FROM "kk" to "LN"
    PBHLD = ((LN-kk)*LH)/dx2)+1;
    PBHLY = PBH-((LN-kk)*LH);
    x = 0:dx2:PBL;
    y = PBHLY:-dy2:0;
    [x, y]=meshgrid(x,y);
    rhop = zeros(n+2-PBHLD,m+1);
    %////////////////////////////////////
    %////////////////////////////////////
    %////////////////////////////////////
    for SN=1:Spots %LOOP FOR SPOTS FROM "SN" to "Spots"
        XL = X0 + (SN-1)*(PD/dx2);
        XR = X0 + (SN-1)*(PD/dx2) + D/dx2;
        XC = XL + ((XR-XL)/2);
        for tstep=1:mstep %LOOP FOR SPOT IRRADIATION TIME
            for j=n+1:-1:PBHLD
                for i=1:m+1
                    for k=1:9
                        feq = w(k)*rho(j,i);
                        f(j,i,k) = omegal*feq + (1-omegal)*f(j,i,k);
                    end
                end
            end
        end
        %-----STREAMING FOR F3 AND F7
        for j=PBHLD:n
            for i=1:m
                f(j,i,3) = f(j+1,i,3);
                if (i==m)
                    f(j,i+1,3) = f(j+1,i+1,3);
                end
                f(j,i,7) = f(j+1,i+1,7);
            end
        end
        %-----STREAMING FOR F2 AND F6
        for j=PBHLD:n
            for i=m+1:-1:2
                f(j,i,2) = f(j,i-1,2);
                if (j==n)
                    f(j+1,i,2) = f(j+1,i-1,2);
                end
                f(j,i,6) = f(j+1,i-1,6);
            end
        end
        %-----STREAMING FOR F5 AND F9

```

```

for j=n+1:-1:PBHLD+1
  for i=m+1:-1:2
    f(j,i,5) = f(j-1,i,5);
    if (i==2)
      f(j,i-1,5) = f(j-1,i-1,5);
    end
    f(j,i,9) = f(j-1,i-1,9);
  end
end
end
%-----STREAMING FOR F4 AND F8
for j=n+1:-1:PBHLD+1
  for i=1:m
    f(j,i,4) = f(j,i+1,4);
    if(j==PBHLD+1)
      f(j-1,i,4) = f(j-1,i+1,4);
    end
    f(j,i,8) = f(j-1,i+1,8);
  end
end
end
%-----BOUNDARY CONDITIONS
%-----TEMPERATURE OF Twall AT THE LEFT AND RIGTH SIDES
for j=n+1:-1:PBHLD
  f(j,1,2) = w(2)*Twall + w(4)*Twall - f(j,1,4);
  f(j,1,6) = w(6)*Twall + w(8)*Twall - f(j,1,8);
  f(j,1,9) = w(9)*Twall + w(7)*Twall - f(j,1,7);
  f(j,m+1,4) = w(4)*Twall + w(2)*Twall - f(j,m+1,2);
  f(j,m+1,8) = w(8)*Twall + w(6)*Twall - f(j,m+1,6);
  f(j,m+1,7) = w(7)*Twall + w(9)*Twall - f(j,m+1,9);
end
%-----TEMPERATURE OF Twall AT THE BUTTOM SIDE
for i=1:m+1
  f(n+1,i,3) = w(3)*Twall + w(5)*Twall - f(n+1,i,5);
  f(n+1,i,7) = w(7)*Twall + w(9)*Twall - f(n+1,i,9);
  f(n+1,i,6) = w(6)*Twall + w(8)*Twall - f(n+1,i,8);
end
%-----CONVECTION & LASER IRRADIATION
for i=m:-1:2
  CTE = (alpha1*dt)/(dx*dx);
  CTE2 = tk / (tk+(chtc*dy2)); %Acc to Kaluza,
G.
  CTE3 = (chtc*dy2)/(tk+(chtc*dy2)); %Acc to Kaluza,
G.
  if i > XR %FROM m TO XR+1 FOR CONVECTION
    f(PBHLD,i,5)=CTE*(f(PBHLD+1,i,3)+f(PBHLD+1,i,5))+(1-
CTE)*(f(PBHLD,i,3)+f(PBHLD,i,5))-
f(PBHLD,i,3)+CTE*(chtc*dx2/tk)*(w(3)*ta+w(5)*ta-f(PBHLD,i,3)-
f(PBHLD,i,5));
  end
  if i <= XR && i >= XL %FROM XR TO XL FOR THE HEAT FLUX
    f(PBHLD,i,5)=CTE*f(PBHLD+1,i,5)+(1-
CTE)*f(PBHLD,i,5)+CTE*(Heatflux*dx2/tk);
  end
  if i < XL %FROM XR-1 TO 2 FOR CONVECTION
    f(PBHLD,i,5)=CTE*(f(PBHLD+1,i,3)+f(PBHLD+1,i,5))+(1-
CTE)*(f(PBHLD,i,3)+f(PBHLD,i,5))-
f(PBHLD,i,3)+CTE*(chtc*dx2/tk)*(w(3)*ta+w(5)*ta-f(PBHLD,i,3)-
f(PBHLD,i,5));
  end
end

```

```

        end
    end
    %-----UPDATE f and rho
    for j=n+1:-1:PBHLD
        for i=1:m+1
            sum = 0;
            for k=1:9
                sum = sum + f(j,i,k);
            end
            rho(j,i) = sum;
            rhop(j-PBHLD+1,i) = rho(j,i);
        end
    end
    %-----SAVE IRRADIATION RESULTS
    TI = TC + ((SN-1)*SIT + tstep*dti);
    if (mod(tstep, val2) == 0)
        figure(1)
        contourf( x, y, rhop);
        axis equal;
        title('Temperatura','FontSize',16);
        xlabel('x [unidades]','FontSize',16);
        ylabel('y [unidades]','FontSize',16);
        drawnow;
        %-----rho VS TIME AT THE CENTER OF EACH SPOT
        TIIS = (SN-1)*(mstep/val2) + (tstep/val2);
        TIS = TCS + TIIS;
        TIME(TIS,1) = TI;
        rhoTT(TIIS,1,kk) = rho(PBHLD,XCS(1));
        rhoTTS1(TIS,1) = rho(PBHLD,XCS(1));
        rhoTI(tstep/val2,SN,kk) = rho(PBHLD,XC);
        MP(TIS,1) = TL;
    end
end %END OF SPOT IRRADIATION TIME
%-----RESULTS AT THE SPOT CENTER
for j=PBHLD:n+1
    rhoCSP(j-PBHLD+1,SN) = rho(j,XC);
end
%-----rho DURING EACH SPOT
for j=PBHLD:n+1
    for i=1:m+1
        rhoS(j-PBHLD+1,i) = rho(j,i);
    end
end
end %END OF SPOTS
end %END OF LAYER DEPOSITION
%-----END_TIME = CLOCK
toc
disp(TI)
Tmax = max(rhoCSP);
%-----PARAMETERS FOR CHECKING RESULTS kk=0
LN = 0;
kk = 0;
PBHLD = (((LN-kk)*LH)/dx2)+1;
PBHLY = PBH-((LN-kk)*LH);
x1 = 0:dx2:PBL;
y1 = PBHLY:-dy2:0;
[x1, y1]=meshgrid(x1,y1);

```

```

rhoL0S1 = zeros(n+2-PBHLd,m+1);
for j=1:n+2-PBHLd
    for i=1:m+1
        rhoL0S1(j,i) = rhoS(j,i,1);
    end
end
%-----LIST AND CHECK RESULTS AT XC (L1 ALSO APPLY FOR L0)
rhomiddleL0S1 = zeros(n+2-PBHLd,1);
for j=1:n+2-PBHLd
    rhomiddleL0S1(j,1) = rhoL0S1(j,XC(1));
end
%-----PLOT AND CHECK RESULTS
%-----T vs y rhomiddleL0S1
figure(2)
plot (y1, rhomiddleL0S1, '-g', 'LineWidth',2.00);
hold on;
xlabel('y (m)', 'FontSize',16, 'FontName', 'Times');
ylabel('T (K)', 'FontSize',16, 'FontName', 'Times');
legend({'SPOT 1'});
lgd = legend;
lgd.FontSize = 9;
box on;

```

SLM 316L SS simulation by FDM

```

clear all
clc
%-----START_TIME = CLOCK
tic
%////////////////////////////////////
%2D FDM MODEL FOR SLM 316L SS L0S1
%////////////////////////////////////
%-----PARAMETERS FOR MODEL GENERATION
PBL = 1000e-6;           %POWDER BED LENGTH (m)
SH = 500e-6;           %SUBSTRATE HIGH (m)
LH = 30e-6;            %LAYER HIGH (m)
LN = 0;                %LAYER NUMBER
D = 80e-6;             %BEAM DIAMETER (m)
SIT = 80e-6;          %SPOT IRRADIATION TIME (s)
RT = 5e-2;             %RECOATING TIME (s)
PD = 20e-6;            %PD PHYSICAL (m)
Spots = 1;             %NUM. SPOTS
dx2 = 10e-6;           %dx PHYSICAL (m)
dy2 = 10e-6;           %dy PHYSICAL (m)

PBH = SH + LN*LH;      %POWDER BED HIGH (m)
RL = D + (Spots-1)*PD; %RASTER LENGTH (m)
%-----PARAMETERS IN FDM
dt = 2e-6;             %s
dx = dx2;              %m
dy = dy2;              %m
mstep = 40;            %TIME STEPS FOR LASER IRRADIATION (SIT)
mcstep = 250;          %TIME STEPS FOR INITIAL CONVECTION (RT)
val1 = 1;              %NUM.VALUES FOR PLOTTING CONVECTION
val2 = 1;              %NUM.VALUES FOR PLOTTING IRRADIATION

```

```

m = int16(PBL/dx);
n = int16(PBH/dx);
RLC = RL/dx; %RASTER LENGTH CELLS
X0 = (m/2+1) - RLC/2; %INITIAL X0 SPOT CELLS
%-----PARAMETERS FOR LASER POSITION
XCS = zeros(1,Spots);
for SN=1:Spots
    XL = X0 + (SN-1)*(PD/dx);
    XR = X0 + (SN-1)*(PD/dx) + D/dx;
    XC = XL + ((XR-XL)/2);
    XCS(1,SN) = XC;
end
%-----PHYSICAL PROPERTIES
alpha = 4.14e-6; %THERMAL DIFUSIVITY PHYSICAL (m2/s)
density = 7980; %DENSITY (kg/m3)
Cp = 545; %SPECIFIC HEAT CAPACITY (J/kg K)
TC = 0; %CONVECTION TIME CONTROL
TCS = 0; %CONVECTION TIME STEP
TI = 0; %LASER IRRADIATION TIME CONTROL
PWR = 100; %LASER POWER (W)
LEA = 0.35; %LASER ENERGY ABSORPTIVITY
GC = 0.865; %GAUSSIAN CONSTANT
Aspot = (pi*D*D)/4; %SPOT AREA (m2)
Aspot2 = D; %SPOT AREA (m2)
Heatflux = LEA*GC*PWR/Aspot; %HEAT FLUX (W/m2)
Volflux = PWR/(Aspot*dy/2); %VOLUMETRIC HEAT FLUX (W/m3)
tk = 18; %THERMAL CONDUCTIVITY (W/m K)
chtc = 20; %CONVECTIVE HEAT TRANSFER COEFFICIENT
(W/m2 K)
ta = 25+273; %ROOM TEMPERATURE 25°C
TL = 1723; %LIQUIDUS TEMPERATURE
IT = 300+273; %POWDER BED TEMPERATURE 300°C
Twall = 300+273; %TEMPERATURE AT THE WALLS
TG = 3000; %TEMPERATURE FOR CONTOURF
%-----VERIFY VALUES
VALUE = ['verify: m = ', num2str(m), ' n = ', num2str(n), ' mstep = ',
num2str(mstep), ' mcstep = ', num2str(mcstep)];
disp(VALUE)
%-----INITIAL CONDITIONS & VARIABLES DEFINITION
fo = zeros(n+1, m+1);
f = zeros(n+1, m+1);
for j=1:n+1
    for i=1:m+1
        fo(j,i) = IT;
        if(i==1)
            fo(j,i) = Twall;
        end
        if(i==m+1)
            fo(j,i) = Twall;
        end
        if(j==n+1)
            fo(j,i) = Twall;
        end
    end
end
end
%-----VARIABLES FOR LISTTING RESULTS

```

```

fS      = zeros(n+1,m+1); %f FOR EACH SPOT
fCSP    = zeros(n+1,Spots); %f OF PBL/2, STARTING AT THE SPOT CENTER
fTT      = zeros(Spots*(mstep/vall),Spots); %f OVER TIME (TI)
fTI      = zeros((mstep/vall),Spots); %f OF IRRADIATION TIME (SPOT CENTER)
MP       = zeros((mstep/vall),1); %MELTING POINT
TIME     = zeros((mstep/vall),1); %SIMULATION TIME
fTTS1    = zeros((mstep/vall),1); %f OF SPOT 1
%-----Do LN = 1 (NO DEPOSITION) FOR CALCULATING VARIABLES
LN = 1;
for kk=1:LN      %LOOP FOR LAYERS DEPOSITION FROM "kk" to "LN"
    PBHLD = (((LN-kk)*LH)/dx)+1;
    PBHLY = PBH-((LN-kk)*LH);
    x = 0:dx:PBL;
    y = PBHLY:-dy:0;
    [x, y]=meshgrid(x,y);
    fp = zeros(n+2-PBHLD,m+1);
    %////////////////////////////////////
    %////////////////////////////////////
    %////////////////////////////////////
    for SN=1:Spots %LOOP FOR SPOTS FROM "SN" to "Spots"
        XL = X0 + (SN-1)*(PD/dx);
        XR = X0 + (SN-1)*(PD/dx) + D/dx;
        XC = XL + ((XR-XL)/2);
        for tstep=1:mstep %LOOP FOR SPOT IRRADIATION TIME
            for i=2:m
                for j=PBHLD+1:n
                    termx = (fo(j+1,i)+fo(j-1,i))/(dx*dx);
                    termy = (fo(j,i-1)+fo(j,i+1))/(dy*dy);
                    dd = (1/(dx*dx))+1/(dy*dy);
                    f(j,i) = fo(j,i) + dt*alpha*(termx+termy-
2*fo(j,i)*dd);
                end
            end
            %-----BOUNDARY CONDITIONS
            %-----TEMPERATURE OF Twall AT THE LEFT AND RIGTH SIDES
            for j=n+1:-1:PBHLD
                f(j,1) = Twall;
                f(j,m+1) = Twall;
            end
            %-----TEMPERATURE OF Twall AT THE BUTTOM SIDE
            for i=2:m
                f(n+1,i) = Twall;
            end
            %-----CONVECTION & LASER IRRADIATION
            for i=m:-1:2
                CTE = (alpha*dt)/(dx*dx);
                CTE2 = tk / (tk+(chtc*dy)); %Acc to Kaluza G.
                CTE3 = (chtc*dy)/(tk+(chtc*dy)); %Acc to Kaluza G.
                if i > XR %FROM m TO XL+1 FOR CONVECTION
                    %Shen, B. OK
                    f(PBHLD,i)=CTE*(fo(PBHLD,i+1)+fo(PBHLD,i-
1)+fo(PBHLD+1,i))+(1-3*CTE)*fo(PBHLD,i)+CTE*(chtc*dx*(ta-
fo(PBHLD,i))/tk);
                end
                if i <= XR && i >= XL %FROM XL TO XR FOR THE HEAT FLUX
                    %Shen, B. OK

```

```

        f(PBHL D,i)=CTE*(fo(PBHL D,i+1)+fo(PBHL D,i-
1)+fo(PBHL D+1,i))+(1-3*CTE)*fo(PBHL D,i)+CTE*(Heatflux*dx/tk);
    end
    if i < XL                %FROM XR-1 TO 2 FOR CONVECTION
        %Shen, B. OK
        f(PBHL D,i)=CTE*(fo(PBHL D,i+1)+fo(PBHL D,i-
1)+fo(PBHL D+1,i))+(1-3*CTE)*fo(PBHL D,i)+CTE*(chtc*dx*(ta-
fo(PBHL D,i))/tk);
    end
end
%-----UPDATE fo
for j=PBHL D:n+1
    for i=1:m+1
        fo(j,i) = f(j,i);
        fp(j-PBHL D+1,i) = fo(j,i);
    end
end
%-----SAVE IRRADIATION RESULTS
TI = TC + ((SN-1)*SIT + tstep*dt);
if (mod(tstep, val2) == 0)
    figure(1)
    contourf( x, y, fp);
    axis equal;
    title('Temperatura','FontSize',16);
    xlabel('x [unidades]','FontSize',16);
    ylabel('y [unidades]','FontSize',16);
    drawnow;
    %-----f VS TIME AT THE CENTER OF EACH SPOT
    TIIS = (SN-1)*(mstep/val2) + (tstep/val2);
    TIS = TCS + TIIS;
    TIME(TIS,1) = TI;
    fTT(TIIS,1,kk) = f(PBHL D,XCS(1));
    fTTS1(TIS,1) = f(PBHL D,XCS(1));
    fTI(tstep/val2,SN,kk) = f(PBHL D,XC);
    MP(TIS,1) = TL;
end
end %END OF SPOT IRRADIATION TIME
%-----RESULTS AT THE SPOT CENTER
for j=PBHL D:n+1
    fCSP(j-PBHL D+1,SN) = f(j,XC);
end
%-----f DURING EACH SPOT
for j=PBHL D:n+1
    for i=1:m+1
        fS(j-PBHL D+1,i) = f(j,i);
    end
end
end %END OF SPOTS
end %END OF LAYER DEPOSITION
%-----END_TIME = CLOCK;
toc
disp(TI)
Tmax = max(fCSP);
%-----PARAMETERS FOR CHECKING RESULTS kk=0
LN = 0;
kk = 0;
PBHL D = ((LN-kk)*LH)/dx)+1;

```

```

PBHLY = PBH - ((LN-kk)*LH);
x1 = 0:dx:PBL;
y1 = PBHLY:-dy:0;
[x1, y1]=meshgrid(x1,y1);
fL0S1 = zeros(n+2-PBHLd,m+1);
for j=1:n+2-PBHLd
    for i=1:m+1
        fL0S1(j,i) = fs(j,i,1);
    end
end
end
%-----LIST AND CHECK RESULTS AT XC (L1 ALSO APPLY FOR L0)
fmiddleL0S1 = zeros(n+2-PBHLd,1);
for j=1:n+2-PBHLd
    fmiddleL0S1(j,1) = fL0S1(j,XC(1));
end
%-----PLOT AND CHECK RESULTS
%-----T vs y fmiddleL0S1
figure(2)
plot (y1, fmiddleL0S1, '-g', 'LineWidth',2.00);
hold on;
xlabel('y (m)', 'FontSize',16, 'FontName', 'Times');
ylabel('T (K)', 'FontSize',16, 'FontName', 'Times');
legend({'SPOT 1'});
lgd = legend;
lgd.FontSize = 9;
box on;

```

SLM 316L SS simulation by LBM

```

clear all
clc
%-----START_TIME = CLOCK
tic
%////////////////////////////////////
%2D LBM MODEL FOR SLM 316L SS L0S1
%////////////////////////////////////
%-----PARAMETERS FOR MODEL GENERATION
PBL = 1000e-6;           %POWDER BED LENGTH (m)
SH = 500e-6;            %SUBSTRATE HIGH (m)
LH = 30e-6;             %LAYER HIGH (m)
LN = 0;                 %LAYER NUMBER
D = 80e-6;              %BEAM DIAMETER (m)
SIT = 80e-6;           %SPOT IRRADIATION TIME (s)
RT = 5e-2;              %RECOATING TIME (s)
PD = 20e-6;             %PD PHYSICAL (m)
Spots = 1;              %NUM. SPOTS
dx2 = 10e-6;           %dx PHYSICAL (m)
dy2 = 10e-6;           %dy PHYSICAL (m)

PBH = SH + LN*LH;       %POWDER BED HIGH (m)
RL = D + (Spots-1)*PD;  %RASTER LENGTH (m)
%-----PARAMETERS IN LBM
dt = 1;                 %dt in LB
dx = 1;                 %dx in LB

```

```

dy = 1; %dy in LB
mstep = 14; %TIME STEPS FOR LASER IRRADIATION (SIT)
mcstep = 75282; %TIME STEPS FOR INITIAL CONVECTION (RT)
vall = 1; %NUM.VALUES FOR PLOTTING CONVECTION
val2 = 1; %NUM.VALUES FOR PLOTTING IRRADIATION
dtc = RT/mcstep; %dtc (s)
dti = SIT/mstep; %dti (s)

m = int16(PBL/dx2);
n = int16(PBH/dx2);
RLB = RL/dx2; %RASTER LENGTH LATTICE
X0 = (m/2+1) - RLB/2; %INITIAL X0 SPOT LATTICE
%-----PARAMETERS FOR LASER POSITION
XCS = zeros(1,Spots);
for SN=1:Spots
    XL = X0 + (SN-1)*(PD/dx2);
    XR = X0 + (SN-1)*(PD/dx2) + D/dx2;
    XC = XL + ((XR-XL)/2);
    XCS(1,SN) = XC;
end
%-----PHYSICAL PROPERTIES
alphaP = 4.14e-6; %THERMAL DIFUSIVITY PHYSICAL (m2/s)
density = 7980; %DENSITY (kg/m3)
Cp = 545; %SPECIFIC HEAT CAPACITY (J/kg K)
TC = 0; %CONVECTION TIME CONTROL
TCS = 0; %CONVECTION TIME STEP
TI = 0; %LASER IRRADIATION TIME CONTROL
PWR = 100; %LASER POWER (W)
LEA = 0.35; %LASER ENERGY ABSORPTIVITY
GC = 0.865; %GAUSSIAN CONSTANT
Aspot = (pi*D*D)/4; %SPOT AREA (m2)
Aspot2 = D; %SPOT AREA (m2)
Heatflux = LEA*GC*PWR/Aspot; %HEAT FLUX (W/m2)
Volflux = PWR/(Aspot*dy2/2); %VOLUMETRIC HEAT FLUX (W/m3)
tk = 18; %THERMAL CONDUCTIVITY (W/m K)
chtc = 20; %CONVECTIVE TRANSFER COEFFICIENT (W/m2 K)
ta = 25+273; %ROOM TEMPERATURE 25°C
TL = 1723; %LIQUIDS TEMPERATURE
IT = 300+273; %POWDER BED TEMPERATURE 300°C
Twall = 300+273; %TEMPERATURE AT THE WALLS
TG = 3000; %TEMPERATURE FOR CONTOURF
%-----PARAMETERS FOR LB
alpha1 = 0.23; %DIFUSIVITY IN LB FOR IRRADIATION TIME
alpha2 = 0.5; %DIFUSIVITY IN LB FOR RECOATING TIME
ck = dx/dt; csq = ck*ck;
omega1 = 1/(3.0*alpha1/(dt*csq)+0.5); %Equation 3.10, solving for
omega. Notebook pp.23
Tao1 = 1/omega1;
omega2 = 1/(3.0*alpha2/(dt*csq)+0.5); %Equation 3.10, solving for
omega. Notebook pp.23
Tao2 = 1/omega2;
%-----VERIFY VALUES
VALUE = ['verify: m = ', num2str(m), ' n = ', num2str(n), ' alpha = ',
num2str(alpha1), ' mstep = ', num2str(mstep), ' mcstep = ',
num2str(mcstep), ' Tao1 = ', num2str(Tao1), ' Tao2 = ', num2str(Tao2)];
disp(VALUE)
%-----INITIAL CONDITIONS & VARIABLES DEFINITION

```

```

rho = zeros(n+1, m+1);
f = zeros(n+1, m+1, 9);
w = [4/9 1/9 1/9 1/9 1/9 1/36 1/36 1/36 1/36];
for j=n+1:-1:1
    for i=1:m+1
        sum = 0;
        for k=1:9
            f(j,i,k) = w(k)*IT;
            if (i==1)
                f(j,i,k) = w(k)*Twall;
            end
            if (i==m+1)
                f(j,i,k) = w(k)*Twall;
            end
            if (j==n+1)
                f(j,i,k) = w(k)*Twall;
            end
            sum = sum + f(j,i,k);
        end
        rho(j,i) = sum;
    end
end
%-----VARIABLES FOR LISTTING RESULTS
rhoS = zeros(n+1,m+1); %rho FOR EACH SPOT
rhoCSP = zeros(n+1,Spots); %rho OF PBL/2, STARTING AT THE SPOT CENTER
rhoTT = zeros(Spots*(mstep/vall),Spots); %rho OVER TIME (TI)
rhoTI = zeros((mstep/vall),Spots); %rho OF IRRADIATION TIME (SPOT
CENTER)
MP = zeros((mstep/vall),1); %MELTING POINT
TIME = zeros((mstep/vall),1); %SIMULATION TIME
rhoTTS1 = zeros((mstep/vall),1); %rho OF SPOT 1
%-----Do LN = 1 (NO DEPOSITION) FOR CALCULATING VARIABLES
LN = 1;
for kk=1:LN %LOOP FOR LAYERS DEPOSITION FROM "kk" to "LN"
    PBHLD = (((LN-kk)*LH)/dx2)+1;
    PBHLY = PBH-((LN-kk)*LH);
    x = 0:dx2:PBL;
    y = PBHLY:-dy2:0;
    [x, y]=meshgrid(x,y);
    rhop = zeros(n+2-PBHLD,m+1);
    %////////////////////////////////////
    %////////////////////////////////////
    %////////////////////////////////////
    for SN=1:Spots %LOOP FOR SPOTS FROM "SN" to "Spots"
        XL = X0 + (SN-1)*(PD/dx2);
        XR = X0 + (SN-1)*(PD/dx2) + D/dx2;
        XC = XL + ((XR-XL)/2);
        for tstep=1:mstep %LOOP FOR SPOT IRRADIATION TIME
            for j=n+1:-1:PBHLD
                for i=1:m+1
                    for k=1:9
                        feq = w(k)*rho(j,i);
                        f(j,i,k) = omegal*feq + (1-omegal)*f(j,i,k);
                    end
                end
            end
        end
    end
end
%-----STREAMING FOR F3 AND F7

```

```

for j=PBHLD:n
  for i=1:m
    f(j,i,3) = f(j+1,i,3);
    if (i==m)
      f(j,i+1,3) = f(j+1,i+1,3);
    end
    f(j,i,7) = f(j+1,i+1,7);
  end
end
%-----STREAMING FOR F2 AND F6
for j=PBHLD:n
  for i=m+1:-1:2
    f(j,i,2) = f(j,i-1,2);
    if (j==n)
      f(j+1,i,2) = f(j+1,i-1,2);
    end
    f(j,i,6) = f(j+1,i-1,6);
  end
end
%-----STREAMING FOR F5 AND F9
for j=n+1:-1:PBHLD+1
  for i=m+1:-1:2
    f(j,i,5) = f(j-1,i,5);
    if (i==2)
      f(j,i-1,5) = f(j-1,i-1,5);
    end
    f(j,i,9) = f(j-1,i-1,9);
  end
end
%-----STREAMING FOR F4 AND F8
for j=n+1:-1:PBHLD+1
  for i=1:m
    f(j,i,4) = f(j,i+1,4);
    if (j==PBHLD+1)
      f(j-1,i,4) = f(j-1,i+1,4);
    end
    f(j,i,8) = f(j-1,i+1,8);
  end
end
%-----BOUNDARY CONDITIONS
%-----TEMPERATURE OF Twall AT THE LEFT AND RIGTH SIDES
for j=n+1:-1:PBHLD
  f(j,1,2) = w(2)*Twall + w(4)*Twall - f(j,1,4);
  f(j,1,6) = w(6)*Twall + w(8)*Twall - f(j,1,8);
  f(j,1,9) = w(9)*Twall + w(7)*Twall - f(j,1,7);
  f(j,m+1,4) = w(4)*Twall + w(2)*Twall - f(j,m+1,2);
  f(j,m+1,8) = w(8)*Twall + w(6)*Twall - f(j,m+1,6);
  f(j,m+1,7) = w(7)*Twall + w(9)*Twall - f(j,m+1,9);
end
%-----TEMPERATURE OF Twall AT THE BUTTOM SIDE
for i=1:m+1
  f(n+1,i,3) = w(3)*Twall + w(5)*Twall - f(n+1,i,5);
  f(n+1,i,7) = w(7)*Twall + w(9)*Twall - f(n+1,i,9);
  f(n+1,i,6) = w(6)*Twall + w(8)*Twall - f(n+1,i,8);
end
%-----CONVECTION & LASER IRRADIATION
for i=m:-1:2

```

```

CTE = (alpha1*dt)/(dx*dx);
CTE2 = tk / (tk+(chtc*dy2)); %Acc to Kaluza,
G.
CTE3 = (chtc*dy2)/(tk+(chtc*dy2)); %Acc to Kaluza,
G.
if i > XR %FROM m TO XR+1 FOR CONVECTION
f(PBHLd,i,5)=CTE*(f(PBHLd+1,i,3)+f(PBHLd+1,i,5))+(1-
CTE)*(f(PBHLd,i,3)+f(PBHLd,i,5))-
f(PBHLd,i,3)+CTE*(chtc*dx2/tk)*(w(3)*ta+w(5)*ta-f(PBHLd,i,3)-
f(PBHLd,i,5));
end
if i <= XR && i >= XL %FROM XR TO XL FOR THE HEAT FLUX
f(PBHLd,i,5)=CTE*f(PBHLd+1,i,5)+(1-
CTE)*f(PBHLd,i,5)+CTE*(Heatflux*dx2/tk);
end
if i < XL %FROM XR-1 TO 2 FOR CONVECTION
f(PBHLd,i,5)=CTE*(f(PBHLd+1,i,3)+f(PBHLd+1,i,5))+(1-
CTE)*(f(PBHLd,i,3)+f(PBHLd,i,5))-
f(PBHLd,i,3)+CTE*(chtc*dx2/tk)*(w(3)*ta+w(5)*ta-f(PBHLd,i,3)-
f(PBHLd,i,5));
end
end
end
%-----UPDATE f and rho
for j=n+1:-1:PBHLd
for i=1:m+1
sum = 0;
for k=1:9
sum = sum + f(j,i,k);
end
rho(j,i) = sum;
rhop(j-PBHLd+1,i) = rho(j,i);
end
end
%-----SAVE IRRADIATION RESULTS
TI = TC + ((SN-1)*SIT + tstep*dti);
if (mod(tstep, val2) == 0)
figure(1)
contourf( x, y, rhop);
axis equal;
title('Temperatura','FontSize',16);
xlabel('x [unidades]','FontSize',16);
ylabel('y [unidades]','FontSize',16);
drawnow;
%-----rho VS TIME AT THE CENTER OF EACH SPOT
TIIS = (SN-1)*(mstep/val2) + (tstep/val2);
TIS = TCS + TIIS;
TIME(TIS,1) = TI;
rhoTT(TIIS,1,kk) = rho(PBHLd,XCS(1));
rhoTTS1(TIS,1) = rho(PBHLd,XCS(1));
rhoTI(tstep/val2,SN,kk) = rho(PBHLd,XC);
MP(TIS,1) = TL;
end
end %END OF SPOT IRRADIATION TIME
%-----RESULTS AT THE SPOT CENTER
for j=PBHLd:n+1
rhoCSP(j-PBHLd+1,SN) = rho(j,XC);
end

```

```

%-----rho DURING EACH SPOT
for j=PBHLD:n+1
    for i=1:m+1
        rhoS(j-PBHLD+1,i) = rho(j,i);
    end
end
end %END OF SPOTS
end %END OF LAYER DEPOSITION
%-----END_TIME = CLOCK
toc
disp(TI)
Tmax = max(rhoCSP);
%-----PARAMETERS FOR CHECKING RESULTS kk=0
LN = 0;
kk = 0;
PBHLD = ((LN-kk)*LH)/dx2)+1;
PBHLY = PBH-(LN-kk)*LH);
x1 = 0:dx2:PBL;
y1 = PBHLY:-dy2:0;
[x1, y1]=meshgrid(x1,y1);
rhoL0S1 = zeros(n+2-PBHLD,m+1);
for j=1:n+2-PBHLD
    for i=1:m+1
        rhoL0S1(j,i) = rhoS(j,i,1);
    end
end
%-----LIST AND CHECK RESULTS AT XC (L1 ALSO APPLY FOR L0)
rhomiddleL0S1 = zeros(n+2-PBHLD,1);
for j=1:n+2-PBHLD
    rhomiddleL0S1(j,1) = rhoL0S1(j,XC(1));
end
%-----PLOT AND CHECK RESULTS
%-----T vs y rhomiddleL0S1
figure(2)
plot (y1, rhomiddleL0S1, '-g', 'LineWidth',2.00);
hold on;
xlabel('y (m)', 'FontSize',16, 'FontName', 'Times');
ylabel('T (K)', 'FontSize',16, 'FontName', 'Times');
legend({'SPOT 1'});
lgd = legend;
lgd.FontSize = 9;
box on;

```

APPENDIX 2

SLM simulation by FDM and LBM considering laser movement (based on point distance), layer deposition, recoating time (5×10^{-3} s) (convection), and number of spots.

Table A2.1 Simulation parameters for AlSi10Mg with laser movement, layer deposition, recoating time 5×10^{-3} s, and number of spots.

Parameter	FDM	LBM
Δx	1×10^{-5} m	1
Δy	1×10^{-5} m	1
Δt	2×10^{-7} s	1
Domain length, L	1×10^{-3} m	100
Substrate height, SH	5×10^{-4} m	50
Layer height, LH	3×10^{-5} m	3
Spot diameter, D	8×10^{-5} m	8
Point distance, PD	2×10^{-5} m	2
Layers number, LN	2	2
Spots number, SN	3	3
Spot irradiation time, SIT (Steps)	1×10^{-4} s (500)	456 steps
Recoating time, RT (Steps)	5×10^{-3} s (25000)	7528 steps
Thermal diffusivity	7.53×10^{-5} m ² /s	0.165 * 0.5 **
Fourier number, F_0	0.0075 * 0.3764 **	0.0075 * 0.3764 **
Relaxation time, τ	-	0.995 * 2**
Collision frequency, ω	-	1.005 * 0.5 **

*The corresponding value for the laser irradiation time (1×10^{-4} s)

**The corresponding value for the recoating time (5×10^{-3} s)

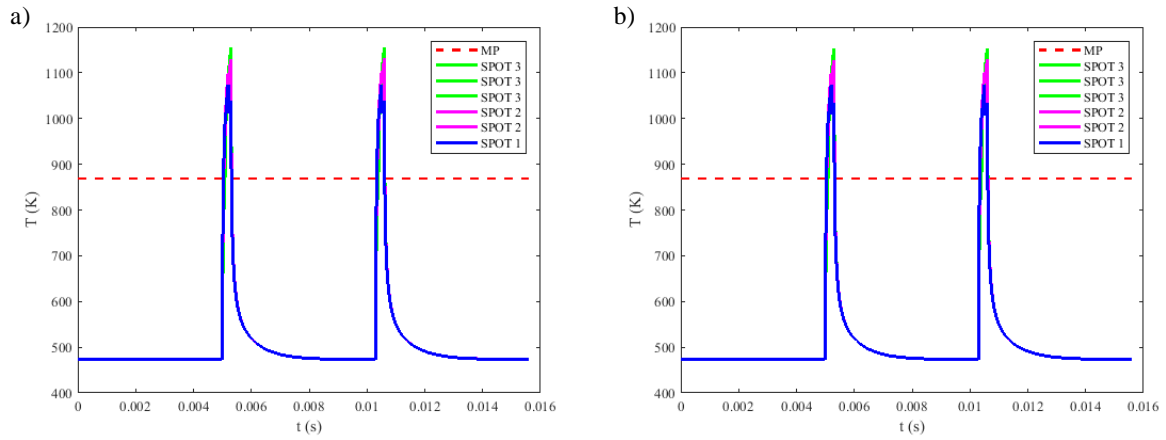


Fig. A2.1 Temperature vs time at the center of each spot during the deposition of SLM AlSi10Mg alloy with a recoating time of 5×10^{-3} s, a) FDM and b) LBM

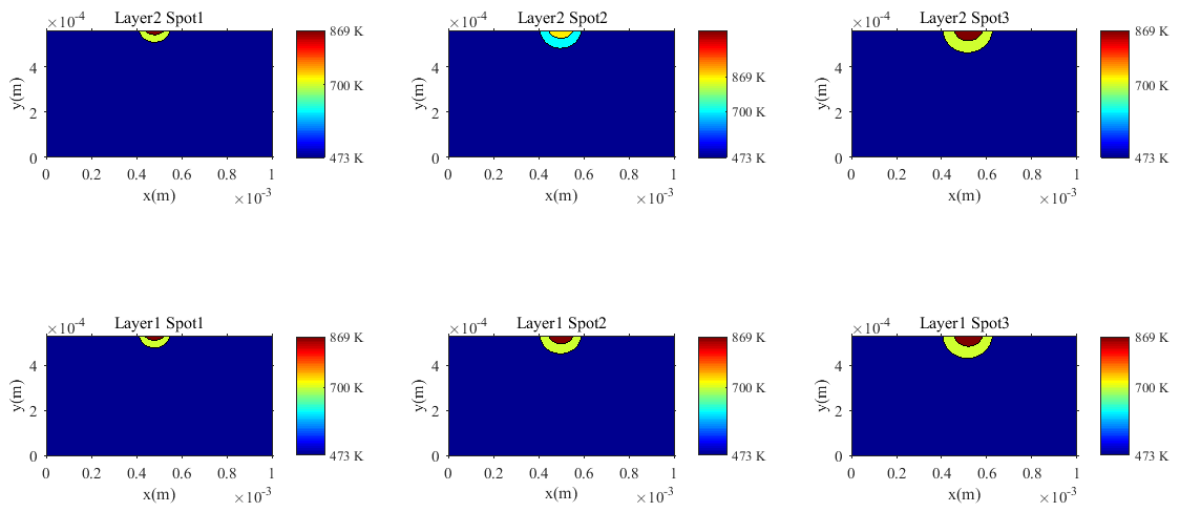


Fig. A2.2 Temperature vs XY position during the laser scanning and layer deposition of SLM AlSi10Mg. Simulation via FDM.

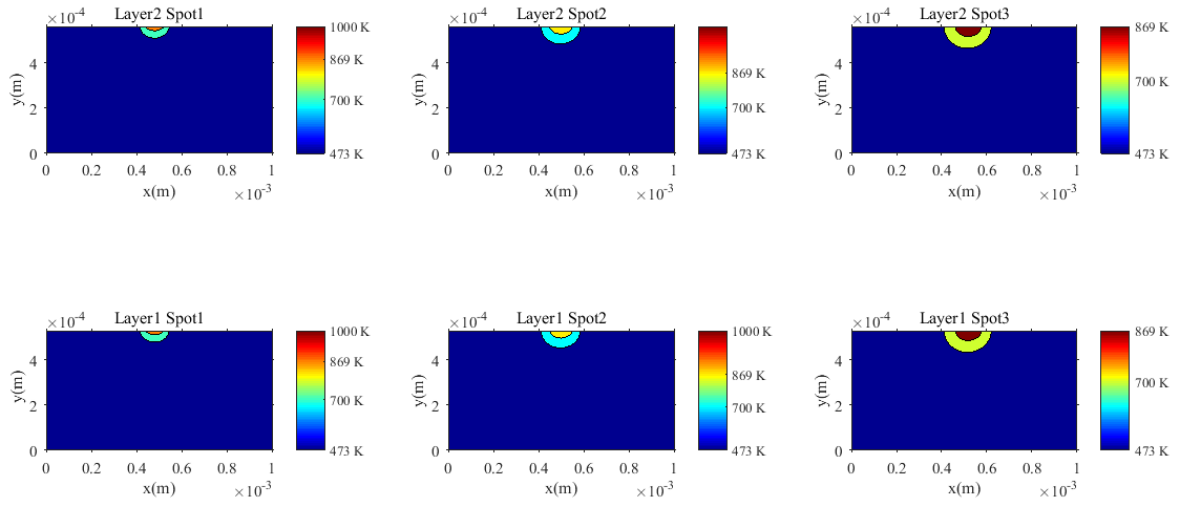


Fig. A2.3 Temperature vs XY position during the laser scanning and layer deposition of SLM AlSi10Mg. Simulation via LBM.

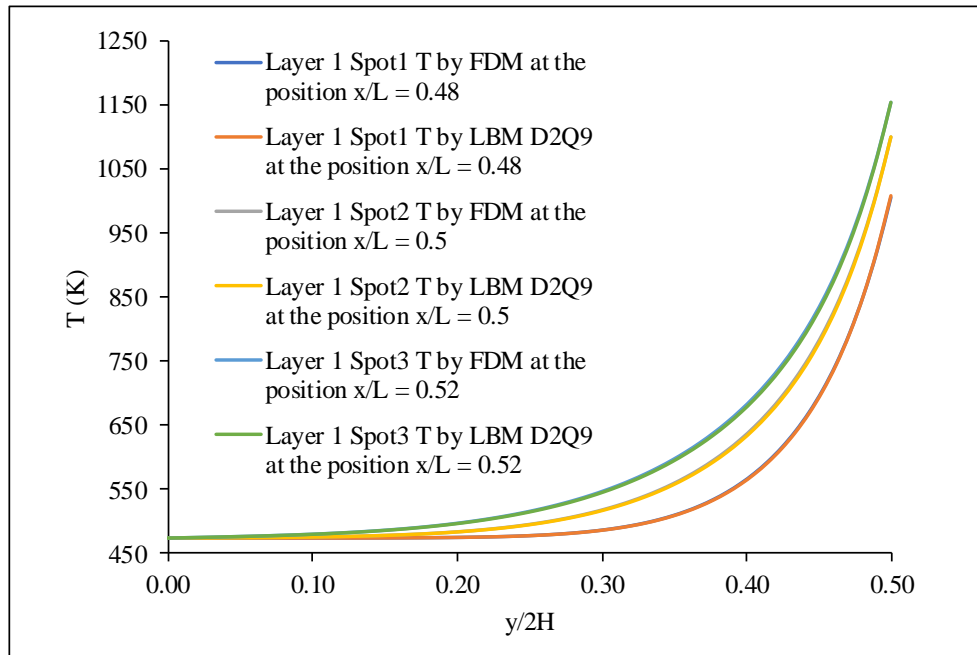


Fig. A2.4 Comparison of temperature values for the three simulated spots in the first layer via FDM and LBM.

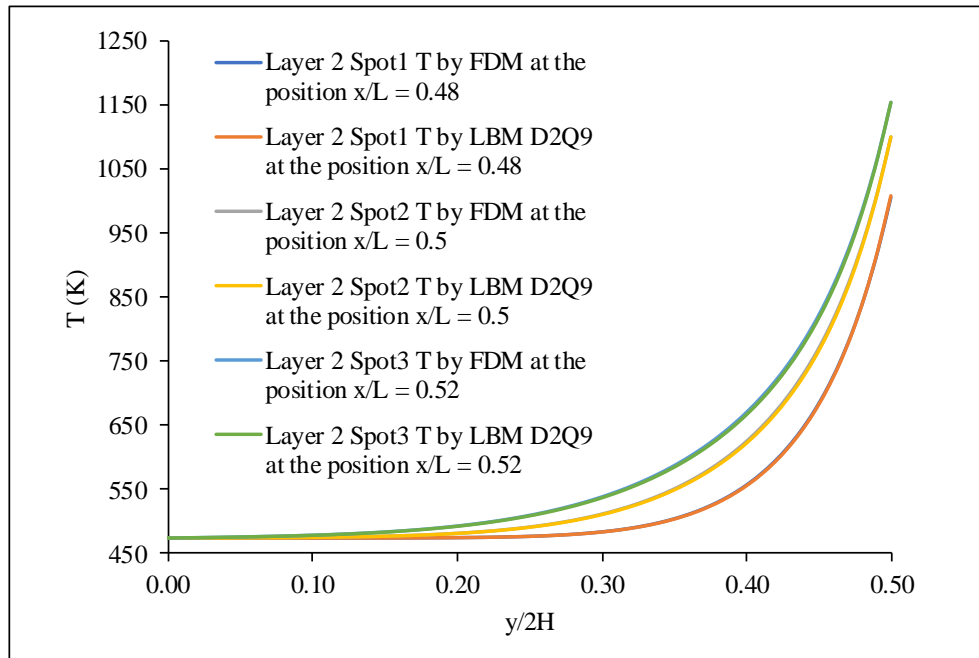


Fig. A2.5 Comparison of temperature values for the three simulated spots in the second layer via FDM and LBM.

Table A2.2 Number of time steps for the FDM and LBM simulations considering a recoating time of 5×10^{-3} s.

Simulation	Method of solution	Commercial software for the computational routine	Number of time steps or iterations
SLM AlSi10Mg	FDM	Matlab	500 *
	LBM		25 000 **
			456 *
			7 528**

*The corresponding value for the laser irradiation time (1×10^{-4} s)

**The corresponding value for the recoating time (5×10^{-3} s)

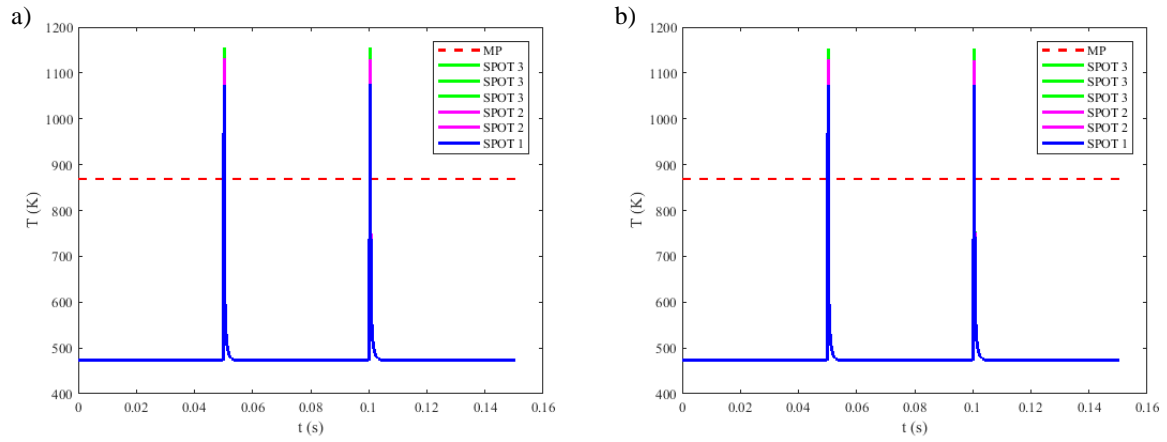


Fig. A2.6 Temperature vs time at the center of each spot during the deposition of SLM AISi10Mg alloy with a recoating time of 5×10^{-2} s, a) FDM and b) LB

APPENDIX 3

SLM AlSi10Mg simulation with laser movement and layer deposition by FDM

```
clear all
clc
%-----START_TIME = CLOCK
tic
%////////////////////////////////////
%2D FDM MODEL FOR SLM AlSi10Mg
%////////////////////////////////////
%-----PARAMETERS FOR MODEL GENERATION
PBL = 1000e-6; %POWDER BED LENGTH (m)
SH = 500e-6; %SUBSTRATE HIGH (m)
LH = 30e-6; %LAYER HIGH (m)
LN = 2; %LAYER NUMBER
D = 80e-6; %BEAM DIAMETER (m)
SIT = 1e-4; %SPOT IRRADIATION TIME (s)
RT = 5e-2; %RECOATING TIME (s)
PD = 20e-6; %PD PHYSICAL (m)
Spots = 3; %NUM. SPOTS
dx2 = 10e-6; %dx PHYSICAL (m)
dy2 = 10e-6; %dy PHYSICAL (m)

PBH = SH + LN*LH; %POWDER BED HIGH (m)
RL = D + (Spots-1)*PD; %RASTER LENGTH (m)
%-----PARAMETERS IN FDM
dt = 0.2e-6; %s
dx = 10e-6; %m
dy = 10e-6; %m
mstep = 500; %TIME STEPS FOR LASER IRRADIATION (SIT)
mcstep = 250000; %TIME STEPS FOR INITIAL CONVECTION (RT)
val1 = 1; %NUM.VALUES FOR PLOTTING CONVECTION
val2 = 1; %NUM.VALUES FOR PLOTTING IRRADIATION

m = int16(PBL/dx);
n = int16(PBH/dx);
RLC = RL/dx; %RASTER LENGTH CELLS
X0 = (m/2+1) - RLC/2; %INITIAL X0 SPOT CELLS
%-----PARAMETERS FOR LASER POSITION
XCS = zeros(1,Spots);
for SN=1:Spots
    XL = X0 + (SN-1)*(PD/dx2);
    XR = X0 + (SN-1)*(PD/dx2) + D/dx2;
    XC = XL + ((XR-XL)/2);
    XCS(1,SN) = XC;
end
%-----PHYSICAL PROPERTIES
alpha = 7.53e-5; %THERMAL DIFUSIVITY (m2/s)
density = 2650; %DENSITY (kg/m3)
Cp = 797; %SPECIFIC HEAT CAPACITY (J/kg K)
TC = 0; %CONVECTION TIME CONTROL
TCS = 0; %CONVECTION TIME STEP
TI = 0; %LASER IRRADIATION TIME CONTROL
PWR = 100; %LASER POWER (W)
LEA = 0.09; %LASER ENERGY ABSORPTIVITY
GC = 0.865; %GAUSSIAN CONSTANT
```

```

Aspot = pi*(D)*(D)/4;           %SPOT AREA (m2)
Aspot2 = 8*D;                   %SPOT AREA (m2)
Heatflux = LEA*GC*PWR/Aspot;    %HEAT FLUX (W/m2)
Volflux = PWR/(Aspot*dy/2);    %VOLUMETRIC HEAT FLUX (W/m3)
tk = 159;                       %THERMAL CONDUCTIVITY (W/m K)
chtc = 20;                      %CONVECTIVE TRANSFER COEFFICIENT (W/m2 K)
ta = 25+273;                   %ROOM TEMPERATURE 25°C
TL = 869;                      %LIQUIDS TEMPERATURE
IT = 200+273;                 %POWDER BED TEMPERATURE 25°C
Twall = 200+273;              %TEMPERATURE AT THE WALLS
TG = 700;                     %TEMPERATURE FOR CONTOURF
%-----VERIFY VALUES
VALUE = ['verify: m = ', num2str(m), ' n = ', num2str(n), ' mstep = ',
num2str(mstep), ' mcstep = ', num2str(mcstep), ' RL = ', num2str(RL), '
RLC = ', num2str(RLC), ' X0 = ', num2str(X0)];
disp(VALUE)
%-----INITIAL CONDITIONS & VARIABLES DEFINITION
fo = zeros(n+1, m+1);
f = zeros(n+1, m+1);
for j=1:n+1
    for i=1:m+1
        fo(j,i) = IT;
        if(i==1)
            fo(j,i) = Twall;
        end
        if(i==m+1)
            fo(j,i) = Twall;
        end
        if(j==n+1)
            fo(j,i) = Twall;
        end
    end
end
end
%////IN CASE OF LN = 0 (NO DEPOSITION)////
%////LN MUST BE EQUAL TO 1
if (LN==0)
    LN=1;
end
%////////////////////////////////////
%//LOOP FOR INITIAL CONVECTION (RT)//
%////////////////////////////////////
%-----FIRTS PARAMETERS FOR CONTROLLING THE MODEL
kk=1;
PBHLD = ((LN-kk)*LH)/dx2+1;
PBHLY = PBH-(LN-kk)*LH;
x0 = 0:dx2:PBL;
y0 = PBHLY:-dy2:0;
[x0, y0]=meshgrid(x0,y0);
fp = zeros(n+2-PBHLd,m+1);
%-----VARIABLES FOR LISTTING RESULTS
fs = zeros(n+1,m+1,LN*Spots); %f FOR EACH SPOT
fCSP = zeros(n+1,Spots,LN); %f OF PBL/2, STARTING AT THE SPOT CENTER
fTT = zeros(Spots*(mstep/val2),Spots,LN); %f OVER TIME (TI)
fTI = zeros((mstep/val2),Spots,LN); %f OF IRRADIATION TIME (SPOT
CENTER)
fTC = zeros((mcstep/val1),Spots,LN+1); %f OF CONVECTION

```

```

MP      = zeros((mcstep/val1)+LN*Spots*(mstep/val2)+LN*(mcstep/val1),1);
%MELTING POINT
TIME    = zeros((mcstep/val1)+LN*Spots*(mstep/val2)+LN*(mcstep/val1),1);
%SIMULATION TIME
fTTS1   = zeros((mcstep/val1)+LN*Spots*(mstep/val2)+LN*(mcstep/val1),1); %f
OF SPOT 1
fTTS2   = zeros((mcstep/val1)+LN*Spots*(mstep/val2)+LN*(mcstep/val1),1); %f
OF SPOT 2
fTTS3   = zeros((mcstep/val1)+LN*Spots*(mstep/val2)+LN*(mcstep/val1),1); %f
OF SPOT 3
%-----LOOP FOR INITIAL CONVECTION
for tcstep=1:mcstep
    for i=2:m
        for j=n:-1:PBHLD+1
            termx = (fo(j+1,i)+fo(j-1,i))/(dx*dx);
            termy = (fo(j,i-1)+fo(j,i+1))/(dy*dy);
            dd = (1/(dx*dx))+1/(dy*dy);
            f(j,i) = fo(j,i) + dt*alpha*(termx+termy-2*fo(j,i)*dd);
        end
    end
%-----BOUNDARY CONDITIONS
%-----Twall AT THE LEFT AND RIGTH SIDES
for j=n+1:-1:PBHLD
    f(j,1) = Twall;
    f(j,m+1) = Twall;
end
%-----TEMPERATURE OF Twall AT THE BUTTOM SIDE
for i=2:m
    f(n+1,i) = Twall;
end
%-----INITIAL CONVECTION, RT (12s)
CTE = (alpha*dt)/(dx*dx);
CTE2 = tk / (tk+(chtc*dy)); %Acc to Kaluza G.
CTE3 = (chtc*dy)/(tk+(chtc*dy)); %Acc to Kaluza G.
for i=m:-1:2
    f(PBHLD,i)=CTE*(fo(PBHLD,i+1)+fo(PBHLD,i-1)+fo(PBHLD+1,i))+(1-
3*CTE)*fo(PBHLD,i)+CTE*(chtc*dy*(ta-fo(PBHLD,i))/tk);
end
%-----UPDATE fo
for j=PBHLD:n+1
    for i=1:m+1
        fo(j,i)=f(j,i);
        fp(j-PBHLD+1,i) = fo(j,i);
    end
end
%-----SAVE INITIAL CONVECTION RESULTS
TC = tcstep*dt;
if (mod(tcstep, val1) == 0)
    %-----fc VS TIME AT THE CENTER OF EACH SPOT
    TCS = tcstep/val1;
    TIME(TCS,1) = TC;
    fTC(TCS,1,kk) = f(PBHLD,XCS(1));
    fTC(TCS,2,kk) = f(PBHLD,XCS(2));
    fTC(TCS,3,kk) = f(PBHLD,XCS(3));
    fTTS1(TCS,1) = f(PBHLD,XCS(1));
    fTTS2(TCS,2) = f(PBHLD,XCS(2));
    fTTS3(TCS,3) = f(PBHLD,XCS(3));
end

```

```

        MP(TCS,1) = TL;
    end
end %END FOR INITIAL CONVECTION LOOP
%%%%%%%%%%%%%%%%%%%%%%%%%%%%%%%%%%%%%%%%%%%%%%%%%%%%%%%%%%%%%%%%%%%%%%%%%%%%%%
%%%%%%%%%%%%%%%%%%%%%%%%%%%%%%%%%%%%%%%%%%%%%%%%%%%%%%%%%%%%%%%%%%%%%%%%%%%%%%/MAIN LOOP%%%%%%%%%%%%%%%%%%%%%%%%%%%%%%%%%%%%%%%%%%%%%%%%%%%%%%%%%%%%%%%%%%%%%%%%%%%%%%
%%%%%%%%%%%%%%%%%%%%%%%%%%%%%%%%%%%%%%%%%%%%%%%%%%%%%%%%%%%%%%%%%%%%%%%%%%%%%%
for kk=1:LN %LOOP FOR LAYERS DEPOSITION FROM "kk" to "LN"
    PBHLD = ((LN-kk)*LH)/dx)+1;
    PBHLY = PBH-(LN-kk)*LH);
    x = 0:dx:PBL;
    y = PBHLY:-dy:0;
    [x, y]=meshgrid(x,y);
    fp = zeros(n+2-PBHLD,m+1);
    %%%%%%%%%%%%%%%%%%%%%%%%%%%%%%%%%%%%%%%%%%%%%%%%%%%%%%%%%%%%%%%%%%%%%%%%%%%%%%%
    %%%%%%%%%%%%%%%%%%%%%%%%%%%%%%%%%%%%%%%%%%%%%%%%%%%%%%%%%%%%%%%%%%%%%%%%%%%%%%%/LOOP FOR SPOTS%%%%%%%%%%%%%%%%%%%%%%%%%%%%%%%%%%%%%%%%%%%%%%%%%%%%%%%%%%%%%%%%%%%%%%%%%%%%%%
    %%%%%%%%%%%%%%%%%%%%%%%%%%%%%%%%%%%%%%%%%%%%%%%%%%%%%%%%%%%%%%%%%%%%%%%%%%%%%%%
    for SN=1:Spots %LOOP FOR SPOTS FROM "SN" to "Spots"
        XL = X0 + (SN-1)*(PD/dx);
        XR = X0 + (SN-1)*(PD/dx) + D/dx;
        XC = XL + ((XR-XL)/2);
        for tstep=1:mstep %LOOP FOR SPOT IRRADIATION TIME
            for i=2:m
                for j=PBHLD+1:n
                    termx = (fo(j+1,i)+fo(j-1,i))/(dx*dx);
                    termy = (fo(j,i-1)+fo(j,i+1))/(dy*dy);
                    dd = (1/(dx*dx))+1/(dy*dy));
                    f(j,i) = fo(j,i) + dt*alpha*(termx+termy-
2*fo(j,i)*dd);
                end
            end
            %-----BOUNDARY CONDITIONS
            %-----TEMPERATURE OF Twall AT THE LEFT AND RIGTH SIDES
            for j=n+1:-1:PBHLD
                f(j,1) = Twall;
                f(j,m+1) = Twall;
            end
            %-----TEMPERATURE OF Twall AT THE BUTTOM SIDE
            for i=2:m
                f(n+1,i) = Twall;
            end
            %-----CONVECTION & LASER IRRADIATION
            for i=m:-1:2
                CTE = (alpha*dt)/(dx*dx);
                CTE2 = tk / (tk+(chtc*dy)); %Acc to Kaluza G.
                CTE3 = (chtc*dy)/(tk+(chtc*dy)); %Acc to Kaluza G.
                if i > XR %FROM m TO XL+1 FOR CONVECTION
                    %Shen, B. OK
                    f(PBHLD,i)=CTE*(fo(PBHLD,i+1)+fo(PBHLD,i-
1)+fo(PBHLD+1,i)))+(1-3*CTE)*fo(PBHLD,i)+CTE*(chtc*dx*(ta-
fo(PBHLD,i))/tk);
                end
                if i <= XR && i >= XL %FROM XL TO XR FOR THE HEAT FLUX
                    %Shen, B. OK
                    f(PBHLD,i)=CTE*(fo(PBHLD,i+1)+fo(PBHLD,i-
1)+fo(PBHLD+1,i)))+(1-3*CTE)*fo(PBHLD,i)+CTE*(Heatflux*dx/tk);
                end
                if i < XL %FROM XR-1 TO 2 FOR CONVECTION

```

```

        %Shen, B. OK
        f(PBHLd,i)=CTE*(fo(PBHLd,i+1)+fo(PBHLd,i-
1)+fo(PBHLd+1,i))+(1-3*CTE)*fo(PBHLd,i)+CTE*(chtc*dx*(ta-
fo(PBHLd,i))/tk);
    end
end
%-----UPDATE fo
for j=PBHLd:n+1
    for i=1:m+1
        fo(j,i) = f(j,i);
        fp(j-PBHLd+1,i) = fo(j,i);
    end
end
%-----SAVE IRRADIATION RESULTS
TI = TC + ((SN-1)*SIT + tstep*dt);
if (mod(tstep, val2) == 0)
    %-----f VS TIME AT THE CENTER OF EACH SPOT
    TIIS = (SN-1)*(mstep/val2) + (tstep/val2);
    TIS = TCS + TIIS;
    TIME(TIS,1) = TI;
    fTT(TIIS,1,kk) = f(PBHLd,XCS(1));
    fTT(TIIS,2,kk) = f(PBHLd,XCS(2));
    fTT(TIIS,3,kk) = f(PBHLd,XCS(3));
    fTTS1(TIS,1) = f(PBHLd,XCS(1));
    fTTS2(TIS,2) = f(PBHLd,XCS(2));
    fTTS3(TIS,3) = f(PBHLd,XCS(3));
    fTI(tstep/val2,SN,kk) = f(PBHLd,XC);
    MP(TIS,1) = TL;
end
end %END OF SPOT IRRADIATION TIME
%-----RESULTS AT THE SPOT CENTER
for j=PBHLd:n+1
    fcSP(j-PBHLd+1,SN,kk) = f(j,XC);
end
%-----f DURING EACH SPOT
if(kk==1)
    for j=PBHLd:n+1
        for i=1:m+1
            fS(j-PBHLd+1,i,kk+(SN-1)) = f(j,i);
        end
    end
end
if(kk==2)
    for j=PBHLd:n+1
        for i=1:m+1
            fS(j-PBHLd+1,i,kk+SN+1) = f(j,i);
        end
    end
end
end %END OF SPOTS
%%%%%%%%%%%%%%%%%%%%%%%%%%%%%%%%%%%%%%%%%%%%%%%%%%%%%%%%%%%%%%%%%%%%%%%%
%//LOOP FOR FINAL CONVECTION (RT)////
%%%%%%%%%%%%%%%%%%%%%%%%%%%%%%%%%%%%%%%%%%%%%%%%%%%%%%%%%%%%%%%%%%%%%%%%
for tcstep=1:mcstep %LOOP FOR FINAL CONVECTION
    for i=2:m
        for j=n:-1:PBHLd+1
            termx = (fo(j+1,i)+fo(j-1,i))/(dx*dx);

```

```

        termy = (fo(j,i-1)+fo(j,i+1))/(dy*dy);
        dd = (1/(dx*dx))+1/(dy*dy);
        f(j,i) = fo(j,i) + dt*alpha*(termx+termy-2*fo(j,i)*dd);
    end
end
%-----BOUNDARY CONDITIONS
%-----Twall AT THE LEFT AND RIGTH SIDES
for j=n+1:-1:PBHLD
    f(j,1) = Twall;
    f(j,m+1) = Twall;
end
%-----TEMPERATURE OF Twall AT THE BUTTOM SIDE
for i=2:m
    f(n+1,i) = Twall;
end
%-----INITIAL CONVECTION, RT (12s)
CTE = (alpha*dt)/(dx*dx);
CTE2 = tk / (tk+(chtc*dy)); %Acc to Kaluza G.
CTE3 = (chtc*dy)/(tk+(chtc*dy)); %Acc to Kaluza G.
for i=m:-1:2
    f(PBHLD,i)=CTE*(fo(PBHLD,i+1)+fo(PBHLD,i-
1)+fo(PBHLD+1,i))+(1-3*CTE)*fo(PBHLD,i)+CTE*(chtc*dy*(ta-
fo(PBHLD,i))/tk);
end
%-----UPDATE fo
for j=PBHLD:n+1
    for i=1:m+1
        fo(j,i)=f(j,i);
        fp(j-PBHLD+1,i) = fo(j,i);
    end
end
%-----SAVE FINAL CONVECTION RESULTS
TC = TI + tcstep*dt;
if (mod(tcstep, vall) == 0)
    %-----fc VS TIME AT THE CENTER OF EACH SPOT
    TCCS = (tcstep/vall);
    TCS = TIS + TCCS;
    TIME(TCS,1) = TC;
    fTC(TCCS,1,kk+1) = f(PBHLD,XCS(1));
    fTC(TCCS,2,kk+1) = f(PBHLD,XCS(2));
    fTC(TCCS,3,kk+1) = f(PBHLD,XCS(3));
    fTTS1(TCS,1) = f(PBHLD,XCS(1));
    fTTS2(TCS,2) = f(PBHLD,XCS(2));
    fTTS3(TCS,3) = f(PBHLD,XCS(3));
    MP(TCS,1) = TL;
end
end %END FOR INITIAL CONVECTION LOOP
end %END OF LAYER DEPOSITION
%-----END_TIME = CLOCK;
toc
disp(TC)
%-----LIST AND CHECK RESULTS AT PBL/2
fmiddle = zeros(n+1,1);
for j=1:n+1
    fmiddle(j,1) = f(j,(m/2)+1);
end
%-----PARAMETERS FOR CHECKING RESULTS

```

```

Tmax = max(fCSP);
kk = 1;
PBHLD = ((LN-kk)*LH)/dx2+1;
PBHLY = PBH-(LN-kk)*LH;
x1 = 0:dx2:PBL;
y1 = PBHLY:-dy2:0;
[x1, y1]=meshgrid(x1,y1);
fL1S1 = zeros(n+2-PBHLD,m+1);
fL1S2 = zeros(n+2-PBHLD,m+1);
fL1S3 = zeros(n+2-PBHLD,m+1);
for j=1:n+2-PBHLD
    for i=1:m+1
        fL1S1(j,i) = fS(j,i,1);
        fL1S2(j,i) = fS(j,i,2);
        fL1S3(j,i) = fS(j,i,3);
    end
end
kk = 2;
PBHLD = ((LN-kk)*LH)/dx2+1;
PBHLY = PBH-(LN-kk)*LH;
x2 = 0:dx2:PBL;
y2 = PBHLY:-dy2:0;
[x2, y2]=meshgrid(x2,y2);
fL2S1 = zeros(n+2-PBHLD,m+1);
fL2S2 = zeros(n+2-PBHLD,m+1);
fL2S3 = zeros(n+2-PBHLD,m+1);
for j=1:n+2-PBHLD
    for i=1:m+1
        fL2S1(j,i) = fS(j,i,4);
        fL2S2(j,i) = fS(j,i,5);
        fL2S3(j,i) = fS(j,i,6);
    end
end
end

```

SLM AlSi10Mg simulation with laser movement and layer deposition by LBM

```

clear all
clc
%-----START_TIME = CLOCK;
tic
%%%%%%%%%%%%%%%%%%%%%%%%%%%%%%%%%%%%%%%%%%%%%%%%%%%%%%%%%%%%%%%%%%%%%%%%
%2D LBM D2Q9 MODEL FOR SLM AlSi10Mg
%%%%%%%%%%%%%%%%%%%%%%%%%%%%%%%%%%%%%%%%%%%%%%%%%%%%%%%%%%%%%%%%%%%%%%%%
%-----PARAMETERS FOR MODEL GENERATION
PBL = 1000e-6; %POWDER BED LENGTH (m)
SH = 500e-6; %SUBSTRATE HIGH (m)
LH = 30e-6; %LAYER HIGH (m)
LN = 2; %LAYER NUMBER
D = 80e-6; %BEAM DIAMETER (m)
SIT = 1e-4; %SPOT IRRADIATION TIME (s)
RT = 5e-2; %RECOATING TIME (s)
PD = 20e-6; %PD PHYSICAL (m)
Spots = 3; %NUM. SPOTS
dx2 = 10e-6; %dx PHYSICAL (m)
dy2 = 10e-6; %dy PHYSICAL (m)

PBH = SH + LN*LH; %POWDER BED HIGH (m)

```

```

RL = D + (Spots-1)*PD;           %RASTER LENGTH (m)
%-----PARAMETERS IN LB
dt = 1;                          %dt in LB
dx = 1;                          %dx in LB
dy = 1;                          %dy in LB
mstep = 456;                     %TIME STEPS FOR LASER IRRADIATION (SIT)
mcstep = 75282;                 %TIME STEPS FOR INITIAL CONVECTION (RT)
vall = 1;                       %NUM.VALUES FOR PLOTTING CONVECTION
val2 = 1;                       %NUM.VALUES FOR PLOTTING IRRADIATION

m = int16(PBL/dx2);
n = int16(PBH/dx2);
RLB = RL/dx2;                   %RASTER LENGTH LATTICE
X0 = (m/2+1) - RLB/2;          %INITIAL X0 SPOT LATTICE
%-----PARAMETERS FOR LASER POSITION
XCS = zeros(1,Spots);
for SN=1:Spots
    XL = X0 + (SN-1)*(PD/dx2);
    XR = X0 + (SN-1)*(PD/dx2) + D/dx2;
    XC = XL + ((XR-XL)/2);
    XCS(1,SN) = XC;
end
%-----PHYSICAL PROPERTIES
alphaP = 7.53e-5;              %THERMAL DIFUSIVITY PHYSICAL (m2/s)
dtc = RT/mcstep;              %dtc (s)
dti = SIT/mstep;              %dti (s)
density = 2650;                %DENSITY (kg/m3)
Cp = 797;                      %SPECIFIC HEAT CAPACITY (J/kg K)
TC = 0;                        %CONVECTION TIME CONTROL
TCS = 0;                      %CONVECTION TIME STEP
TI = 0;                        %LASER IRRADIATION TIME CONTROL
PWR = 100;                    %LASER POWER (W)
PWR2 = 100/1e6;               %LASER POWER (J/us)
LEA = 0.09;                   %LASER ENERGY ABSORPTIVITY
GC = 0.865;                   %GAUSSIAN CONSTANT
Aspot = (pi*D*D)/4;           %SPOT AREA (m2)
Aspot2 = D;                   %SPOT AREA (m2)
Heatflux = LEA*GC*PWR/Aspot;  %HEAT FLUX (W/m2)
Heatflux2 = LEA*GC*PWR2/Aspot; %HEAT FLUX (J/us m2)
Volflux = PWR/(Aspot*dy2/2);  %VOLUMETRIC HEAT FLUX (W/m3)
tk = 159;                     %THERMAL CONDUCTIVITY (W/m K)
chtc = 20;                    %CONVECTIVE TRANSFER COEFFICIENT (W/m2 K)
ta = 25+273;                  %ROOM TEMPERATURE 25°C
TL = 869;                     %LIQUIDS TEMPERATURE
IT = 200+273;                 %POWDER BED TEMPERATURE 25°C
Twall = 200+273;              %TEMPERATURE AT THE WALLS
TG = 700;                     %TEMPERATURE FOR CONTOURF
%-----PARAMETERS FOR LB
alpha1 = 0.165;                %DIFUSIVITY IN LB FOR IRRADIATION TIME
alpha2 = 0.5;                  %DIFUSIVITY IN LB FOR RECOATING TIME
ck = dx/dt; csq = ck*ck;
omega1 = 1/(3.0*alpha1/(dt*csq)+0.5); %Equation 3.10, solving for
omega. Notebook pp.23
Tao1 = 1/omega1;
omega2 = 1/(3.0*alpha2/(dt*csq)+0.5); %Equation 3.10, solving for
omega. Notebook pp.23
Tao2 = 1/omega2;

```

```

%-----VERIFY VALUES
VALUE = ['verify: m = ', num2str(m), ' n = ', num2str(n), ' mstep = ',
num2str(mstep), ' mcstep = ', num2str(mcstep), ' Tao1 = ', num2str(Tao1)
, ' Tao2 = ', num2str(Tao2)];
disp(VALUE)
%-----INITIAL CONDITIONS & VARIABLES DEFINITION
rho = zeros(n+1, m+1);
f = zeros(n+1, m+1, 9);
w = [4/9 1/9 1/9 1/9 1/9 1/36 1/36 1/36 1/36];
PBHL1 = (((LN-1)*LH)/dx2)+1;
for j=n+1:-1:1
    for i=1:m+1
        sum = 0;
        for k=1:9
            f(j,i,k) = w(k)*IT;
            if (i==1)
                f(j,i,k) = w(k)*Twall;
            end
            if (i==m+1)
                f(j,i,k) = w(k)*Twall;
            end
            if (j==n+1)
                f(j,i,k) = w(k)*Twall;
            end
            sum = sum + f(j,i,k);
        end
        rho(j,i) = sum;
    end
end
%////IN CASE OF LN = 0 (NO DEPOSITION)////
%////LN MUST BE EQUAL TO 1
if (LN==0)
    LN=1;
end
%////////////////////////////////////
%//LOOP FOR INITIAL CONVECTION (RT)//
%////////////////////////////////////
%-----FIRTS PARAMETERS FOR CONTROLLING THE MODEL
kk=1;
PBHLD = (((LN-kk)*LH)/dx2)+1;
PBHLY = PBH-((LN-kk)*LH);
x0 = 0:dx2:PBL;
y0 = PBHLY:-dy2:0;
[x0, y0]=meshgrid(x0,y0);
rhop = zeros(n+2-PBHL1,m+1);
%-----VARIABLES FOR LISTTING RESULTS
rhoS = zeros(n+1,m+1,LN*Spots); %rho FOR EACH SPOT
rhoCSP = zeros(n+1,Spots,LN); %rho OF PBL/2, STARTING AT THE SPOT
CENTER
rhoTT = zeros(Spots*(mstep/val2),Spots,LN); %rho OVER TIME (TI)
rhoTI = zeros((mstep/val2),Spots,LN); %rho OF IRRADIATION TIME (SPOT
CENTER)
rhoTC = zeros((mcstep/val1),Spots,LN+1); %rho OF CONVECTION
MP = zeros((mcstep/val1)+LN*Spots*(mstep/val2)+LN*(mcstep/val1),1);
%MELTING POINT
TIME = zeros((mcstep/val1)+LN*Spots*(mstep/val2)+LN*(mcstep/val1),1);
%SIMULATION TIME

```

```

rhoTTS1 = zeros((mcstep/val1)+LN*Spots*(mstep/val2)+LN*(mcstep/val1),1);
%rho OF SPOT 1
rhoTTS2 = zeros((mcstep/val1)+LN*Spots*(mstep/val2)+LN*(mcstep/val1),1);
%rho OF SPOT 2
rhoTTS3 = zeros((mcstep/val1)+LN*Spots*(mstep/val2)+LN*(mcstep/val1),1);
%rho OF SPOT 3
%-----LOOP FOR INITIAL CONVECTION
for tcstep=1:mcstep
    for j=n+1:-1:PBHLD
        for i=1:m+1
            for k=1:9
                feq = w(k)*rho(j,i);
                f(j,i,k) = omega2*feq + (1-omega2)*f(j,i,k);
            end
        end
    end
end
%-----STREAMING FOR F3 AND F7
for j=PBHLD:n
    for i=1:m
        f(j,i,3) = f(j+1,i,3);
        if (i==m)
            f(j,i+1,3) = f(j+1,i+1,3);
        end
        f(j,i,7) = f(j+1,i+1,7);
    end
end
%-----STREAMING FOR F2 AND F6
for j=PBHLD:n
    for i=m+1:-1:2
        f(j,i,2) = f(j,i-1,2);
        if (j==n)
            f(j+1,i,2) = f(j+1,i-1,2);
        end
        f(j,i,6) = f(j+1,i-1,6);
    end
end
%-----STREAMING FOR F5 AND F9
for j=n+1:-1:PBHLD+1
    for i=m+1:-1:2
        f(j,i,5) = f(j-1,i,5);
        if (i==2)
            f(j,i-1,5) = f(j-1,i-1,5);
        end
        f(j,i,9) = f(j-1,i-1,9);
    end
end
%-----STREAMING FOR F4 AND F8
for j=n+1:-1:PBHLD+1
    for i=1:m
        f(j,i,4) = f(j,i+1,4);
        if(j==PBHLD+1)
            f(j-1,i,4) = f(j-1,i+1,4);
        end
        f(j,i,8) = f(j-1,i+1,8);
    end
end
%-----BOUNDARY CONDITIONS

```

```

%-----Twall AT THE LEFT AND RIGTH SIDES
for j=n+1:-1:PBHLD
    f(j,1,2) = w(2)*Twall + w(4)*Twall - f(j,1,4);
    f(j,1,6) = w(6)*Twall + w(8)*Twall - f(j,1,8);
    f(j,1,9) = w(9)*Twall + w(7)*Twall - f(j,1,7);
    f(j,m+1,4) = w(4)*Twall + w(2)*Twall - f(j,m+1,2);
    f(j,m+1,8) = w(8)*Twall + w(6)*Twall - f(j,m+1,6);
    f(j,m+1,7) = w(7)*Twall + w(9)*Twall - f(j,m+1,9);
end
%-----TEMPERATURE OF Twall AT THE BUTTOM SIDE
for i=1:m+1
    f(n+1,i,3) = w(3)*Twall + w(5)*Twall - f(n+1,i,5);
    f(n+1,i,7) = w(7)*Twall + w(9)*Twall - f(n+1,i,9);
    f(n+1,i,6) = w(6)*Twall + w(8)*Twall - f(n+1,i,8);
end
%-----INITIAL CONVECTION, RT (12s)
for i=m:-1:2
    CTE = (alpha2*dt)/(dx*dx);
    CTE2 = tk / (tk+(chtc*dy2)); %Acc to Kaluza, G.
    CTE3 = (chtc*dy2)/(tk+(chtc*dy2)); %Acc to Kaluza, G.
    f(PBHLD,i,5)=CTE*(f(PBHLD+1,i,3)+f(PBHLD+1,i,5))+(1-
CTE)*(f(PBHLD,i,3)+f(PBHLD,i,5))-
f(PBHLD,i,3)+CTE*(chtc*dx2*((w(3)+w(5))*ta-f(PBHLD,i,3)-
f(PBHLD,i,5))/tk);
end
%-----UPDATE f and rho
for j=n+1:-1:PBHLD
    for i=1:m+1
        sum = 0;
        for k=1:9
            sum = sum + f(j,i,k);
        end
        rho(j,i) = sum;
        rhop(j-PBHLD+1,i) = rho(j,i);
    end
end
%-----SAVE INITIAL CONVECTION RESULTS
TC = tcstep*dtc;
if (mod(tcstep, vall) == 0)
    %-----rhoc VS TIME AT THE CENTER OF EACH SPOT
    TCS = tcstep/vall;
    TIME(TCS,1) = TC;
    rhoTC(TCS,1,kk) = rho(PBHLD,XCS(1));
    rhoTC(TCS,2,kk) = rho(PBHLD,XCS(2));
    rhoTC(TCS,3,kk) = rho(PBHLD,XCS(3));
    rhoTTS1(TCS,1) = rho(PBHLD,XCS(1));
    rhoTTS2(TCS,2) = rho(PBHLD,XCS(2));
    rhoTTS3(TCS,3) = rho(PBHLD,XCS(3));
    MP(TCS,1) = TL;
end
end %END FOR INITIAL CONVECTION LOOP
%////////////////////////////////////
%////////////////////////////////////MAIN LOOP////////////////////////////////////
%////////////////////////////////////
for kk=1:LN %LOOP FOR LAYERS DEPOSITION FROM "kk" to "LN"
    PBHLD = (((LN-kk)*LH)/dx2)+1;
    PBHLY = PBH-(LN-kk)*LH);

```

```

x = 0:dx2:PBL;
y = PBHLY:-dy2:0;
[x, y]=meshgrid(x,y);
rhop = zeros(n+2-PBHLd,m+1);
%%%%%%%%%%%%%%%%%%%%%%%%%%%%%%%%%%%%%%%%%%%%%%%%%%%%%%%%%%%%%%%%%%%%%%%%
%%%%%%%%%%%%%%%%%%%%%%%%%%%%%%%%%%%%%%%%%%%%%%%%%%%%%%%%%%%%%%%%%%%%%%%%
%%%%%%%%%%%%%%%%%%%%%%%%%%%%%%%%%%%%%%%%%%%%%%%%%%%%%%%%%%%%%%%%%%%%%%%%
for SN=1:Spots %LOOP FOR SPOTS FROM "SN" to "Spots"
    XL = X0 + (SN-1)*(PD/dx2);
    XR = X0 + (SN-1)*(PD/dx2) + D/dx2;
    XC = XL + ((XR-XL)/2);
    for tstep=1:mstep %LOOP FOR SPOT IRRADIATION TIME
        for j=n+1:-1:PBHLd
            for i=1:m+1
                for k=1:9
                    feq = w(k)*rho(j,i);
                    f(j,i,k) = omegal*feq + (1-omegal)*f(j,i,k);
                end
            end
        end
        %-----STREAMING FOR F3 AND F7
        for j=PBHLd:n
            for i=1:m
                f(j,i,3) = f(j+1,i,3);
                if (i==m)
                    f(j,i+1,3) = f(j+1,i+1,3);
                end
                f(j,i,7) = f(j+1,i+1,7);
            end
        end
        %-----STREAMING FOR F2 AND F6
        for j=PBHLd:n
            for i=m+1:-1:2
                f(j,i,2) = f(j,i-1,2);
                if (j==n)
                    f(j+1,i,2) = f(j+1,i-1,2);
                end
                f(j,i,6) = f(j+1,i-1,6);
            end
        end
        %-----STREAMING FOR F5 AND F9
        for j=n+1:-1:PBHLd+1
            for i=m+1:-1:2
                f(j,i,5) = f(j-1,i,5);
                if (i==2)
                    f(j,i-1,5) = f(j-1,i-1,5);
                end
                f(j,i,9) = f(j-1,i-1,9);
            end
        end
        %-----STREAMING FOR F4 AND F8
        for j=n+1:-1:PBHLd+1
            for i=1:m
                f(j,i,4) = f(j,i+1,4);
                if (j==PBHLd+1)
                    f(j-1,i,4) = f(j-1,i+1,4);
                end
            end
        end
    end
end

```

```

        f(j,i,8) = f(j-1,i+1,8);
    end
end
%-----BOUNDARY CONDITIONS
%-----TEMPERATURE OF Twall AT THE LEFT AND RIGTH SIDES
for j=n+1:-1:PBHLD
    f(j,1,2) = w(2)*Twall + w(4)*Twall - f(j,1,4);
    f(j,1,6) = w(6)*Twall + w(8)*Twall - f(j,1,8);
    f(j,1,9) = w(9)*Twall + w(7)*Twall - f(j,1,7);
    f(j,m+1,4) = w(4)*Twall + w(2)*Twall - f(j,m+1,2);
    f(j,m+1,8) = w(8)*Twall + w(6)*Twall - f(j,m+1,6);
    f(j,m+1,7) = w(7)*Twall + w(9)*Twall - f(j,m+1,9);
end
%-----TEMPERATURE OF Twall AT THE BUTTOM SIDE
for i=1:m+1
    f(n+1,i,3) = w(3)*Twall + w(5)*Twall - f(n+1,i,5);
    f(n+1,i,7) = w(7)*Twall + w(9)*Twall - f(n+1,i,9);
    f(n+1,i,6) = w(6)*Twall + w(8)*Twall - f(n+1,i,8);
end
%-----CONVECTION & LASER IRRADIATION
for i=m:-1:2
    CTE = (alpha1*dt)/(dx*dx);
    CTE2 = tk / (tk+(chtc*dy2)); %Acc to Kaluza,
G.
    CTE3 = (chtc*dy2)/(tk+(chtc*dy2)); %Acc to Kaluza,
G.
    if i > XR %FROM m TO XR+1 FOR CONVECTION
        f(PBHLD,i,5)=CTE*(f(PBHLD+1,i,3)+f(PBHLD+1,i,5))+(1-
CTE)*(f(PBHLD,i,3)+f(PBHLD,i,5))-
f(PBHLD,i,3)+CTE*(chtc*dx2*((w(3)+w(5))*ta-f(PBHLD,i,3)-
f(PBHLD,i,5))/tk);
    end
    if i <= XR && i >= XL %FROM XR TO XL FOR THE HEAT FLUX
        f(PBHLD,i,5)=CTE*f(PBHLD+1,i,5)+(1-
CTE)*f(PBHLD,i,5)+CTE*(Heatflux*dx2/tk);
    end
    if i < XL %FROM XR-1 TO 2 FOR CONVECTION
        f(PBHLD,i,5)=CTE*(f(PBHLD+1,i,3)+f(PBHLD+1,i,5))+(1-
CTE)*(f(PBHLD,i,3)+f(PBHLD,i,5))-
f(PBHLD,i,3)+CTE*(chtc*dx2*((w(3)+w(5))*ta-f(PBHLD,i,3)-
f(PBHLD,i,5))/tk);
    end
end
end
%-----UPDATE f and rho
for j=n+1:-1:PBHLD
    for i=1:m+1
        sum = 0;
        for k=1:9
            sum = sum + f(j,i,k);
        end
        rho(j,i) = sum;
        rhop(j-PBHLD+1,i) = rho(j,i);
    end
end
end
%-----SAVE IRRADIATION RESULTS
TI = TC + ((SN-1)*SIT + tstep*dti);
if (mod(tstep, val2) == 0)

```

```

%-----rho VS TIME AT THE CENTER OF EACH SPOT
TIIS = (SN-1)*(mstep/val2) + (tstep/val2);
TIS = TCS + TIIS;
TIME(TIS,1) = TI;
rhoTT(TIIS,1,kk) = rho(PBHL,D,XCS(1));
rhoTT(TIIS,2,kk) = rho(PBHL,D,XCS(2));
rhoTT(TIIS,3,kk) = rho(PBHL,D,XCS(3));
rhoTTS1(TIS,1) = rho(PBHL,D,XCS(1));
rhoTTS2(TIS,2) = rho(PBHL,D,XCS(2));
rhoTTS3(TIS,3) = rho(PBHL,D,XCS(3));
rhoTI(tstep/val2,SN,kk) = rho(PBHL,D,XC);
MP(TIS,1) = TL;
end
end %END OF SPOT IRRADIATION TIME
%-----RESULTS AT THE SPOT CENTER
for j=PBHL,D:n+1
    rhoCSP(j-PBHL,D+1,SN,kk) = rho(j,XC);
end
%-----rho DURING EACH SPOT
if(kk==1)
    for j=PBHL,D:n+1
        for i=1:m+1
            rhoS(j-PBHL,D+1,i,kk+(SN-1)) = rho(j,i);
        end
    end
end
if(kk==2)
    for j=PBHL,D:n+1
        for i=1:m+1
            rhoS(j-PBHL,D+1,i,kk+SN+1) = rho(j,i);
        end
    end
end
end %END OF SPOTS
%////////////////////////////////////
%//LOOP FOR FINAL CONVECTION (RT)//
%////////////////////////////////////
for tcstep=1:mcstep %LOOP FOR FINAL CONVECTION
    for j=n+1:-1:PBHL,D
        for i=1:m+1
            for k=1:9
                feq = w(k)*rho(j,i);
                f(j,i,k) = omega2*feq + (1-omega2)*f(j,i,k);
            end
        end
    end
end
%-----STREAMING FOR F3 AND F7
for j=PBHL,D:n
    for i=1:m
        f(j,i,3) = f(j+1,i,3);
        if (i==m)
            f(j,i+1,3) = f(j+1,i+1,3);
        end
        f(j,i,7) = f(j+1,i+1,7);
    end
end
%-----STREAMING FOR F2 AND F6

```

```

for j=PBHLD:n
  for i=m+1:-1:2
    f(j,i,2) = f(j,i-1,2);
    if (j==n)
      f(j+1,i,2) = f(j+1,i-1,2);
    end
    f(j,i,6) = f(j+1,i-1,6);
  end
end
%-----STREAMING FOR F5 AND F9
for j=n+1:-1:PBHLD+1
  for i=m+1:-1:2
    f(j,i,5) = f(j-1,i,5);
    if (i==2)
      f(j,i-1,5) = f(j-1,i-1,5);
    end
    f(j,i,9) = f(j-1,i-1,9);
  end
end
%-----STREAMING FOR F4 AND F8
for j=n+1:-1:PBHLD+1
  for i=1:m
    f(j,i,4) = f(j,i+1,4);
    if (j==PBHLD+1)
      f(j-1,i,4) = f(j-1,i+1,4);
    end
    f(j,i,8) = f(j-1,i+1,8);
  end
end
%-----BOUNDARY CONDITIONS
%-----Twall AT THE LEFT AND RIGTH SIDES
for j=n+1:-1:PBHLD
  f(j,1,2) = w(2)*Twall + w(4)*Twall - f(j,1,4);
  f(j,1,6) = w(6)*Twall + w(8)*Twall - f(j,1,8);
  f(j,1,9) = w(9)*Twall + w(7)*Twall - f(j,1,7);
  f(j,m+1,4) = w(4)*Twall + w(2)*Twall - f(j,m+1,2);
  f(j,m+1,8) = w(8)*Twall + w(6)*Twall - f(j,m+1,6);
  f(j,m+1,7) = w(7)*Twall + w(9)*Twall - f(j,m+1,9);
end
%-----TEMPERATURE OF Twall AT THE BUTTOM SIDE
for i=1:m+1
  f(n+1,i,3) = w(3)*Twall + w(5)*Twall - f(n+1,i,5);
  f(n+1,i,7) = w(7)*Twall + w(9)*Twall - f(n+1,i,9);
  f(n+1,i,6) = w(6)*Twall + w(8)*Twall - f(n+1,i,8);
end
%-----INITIAL CONVECTION, RT (12s)
for i=m:-1:2
  CTE = (alpha2*dt)/(dx*dx);
  CTE2 = tk/(tk+(chtc*dy2)); %Acc to Kaluza, G.
  CTE3 = (chtc*dy2)/(tk+(chtc*dy2)); %Acc to Kaluza, G.
  f(PBHLD,i,5)=CTE*(f(PBHLD+1,i,3)+f(PBHLD+1,i,5))+(1-
CTE)*(f(PBHLD,i,3)+f(PBHLD,i,5))-
f(PBHLD,i,3)+CTE*(chtc*dx2*((w(3)+w(5))*ta-f(PBHLD,i,3)-
f(PBHLD,i,5))/tk);
end
%-----UPDATE f and rho
for j=n+1:-1:PBHLD

```

```

        for i=1:m+1
            sum = 0;
            for k=1:9
                sum = sum + f(j,i,k);
            end
            rho(j,i) = sum;
            rhop(j-PBHLd+1,i) = rho(j,i);
        end
    end
end
%-----SAVE FINAL CONVECTION RESULTS
TC = TI + tcstep*dtc;
if (mod(tcstep, vall) == 0)
    %-----rhoc VS TIME AT THE CENTER OF EACH SPOT
    TCCS = (tcstep/vall);
    TCS = TIS + TCCS;
    TIME(TCS,1) = TC;
    rhoTC(TCCS,1,kk+1) = rho(PBHLd,XCS(1));
    rhoTC(TCCS,2,kk+1) = rho(PBHLd,XCS(2));
    rhoTC(TCCS,3,kk+1) = rho(PBHLd,XCS(3));
    rhoTTS1(TCS,1) = rho(PBHLd,XCS(1));
    rhoTTS2(TCS,2) = rho(PBHLd,XCS(2));
    rhoTTS3(TCS,3) = rho(PBHLd,XCS(3));
    MP(TCS,1) = TL;
end
end %END FOR FINAL CONVECTION LOOP
end %END OF LAYER DEPOSITION
%-----END_TIME = CLOCK;
toc
disp(TC)
%-----LIST AND CHECK RESULTS AT PBL/2
rhomiddle = zeros(n+1,1);
for j=1:n+1
    rhomiddle(j,1) = rho(j,(m/2)+1);
end
%-----PARAMETERS FOR CHECKING RESULTS
Tmax = max(rhoCSP);
kk = 1;
PBHLd = (((LN-kk)*LH)/dx2)+1;
PBHLY = PBH-((LN-kk)*LH);
x1 = 0:dx2:PBL;
y1 = PBHLY:-dy2:0;
[x1, y1]=meshgrid(x1,y1);
rhoL1S1 = zeros(n+2-PBHLd,m+1);
rhoL1S2 = zeros(n+2-PBHLd,m+1);
rhoL1S3 = zeros(n+2-PBHLd,m+1);
for j=1:n+2-PBHLd
    for i=1:m+1
        rhoL1S1(j,i) = rhoS(j,i,1);
        rhoL1S2(j,i) = rhoS(j,i,2);
        rhoL1S3(j,i) = rhoS(j,i,3);
    end
end
end
kk = 2;
PBHLd = (((LN-kk)*LH)/dx2)+1;
PBHLY = PBH-((LN-kk)*LH);
x2 = 0:dx2:PBL;
y2 = PBHLY:-dy2:0;

```

```
[x2, y2]=meshgrid(x2,y2);
rhoL2S1 = zeros (n+2-PBHL D,m+1);
rhoL2S2 = zeros (n+2-PBHL D,m+1);
rhoL2S3 = zeros (n+2-PBHL D,m+1);
for j=1:n+2-PBHL D
    for i=1:m+1
        rhoL2S1(j,i) = rhoS(j,i,4);
        rhoL2S2(j,i) = rhoS(j,i,5);
        rhoL2S3(j,i) = rhoS(j,i,6);
    end
end
end
```

APPENDIX 4

- R. Guzmán-Nogales, E. Estupiñan-López, C. Gaona-Tiburcio, O.E. López-Botello, J.G. Ramírez-Rodríguez, P.C. Zambrano-Robledo, Corrosion Resistance Measurement of 316L Stainless Steel Manufactured by Selective Laser Melting, *Materials* 2021, 14, 4509. doi.org/10.3390/ma14164509.
- R. Guzmán, V. Lince, O. López, P.C. Zambrano, Microstructure prediction of a SS316L alloy manufactured by Selective Laser Melting, *XXVII International Materials Research Congress* 2018.

APPENDIX 5

Elapsed time for the SLM AlSi10Mg simulation by FEM

Job:SLMA1Si10Mg at:Wed Jun 02 15:53:17 2021 Number of cores used: 1 Degrees of Freedom: 15301 DOF Constraints: 401 Elements: 5000 Assembled: 5000 Implicit: 0 Nodes: 15301 Number of Load Cases: 1 TOTAL PCG SOLVER SOLUTION CP TIME = 0.31 secs TOTAL PCG SOLVER SOLUTION ELAPSED TIME = 0.16 secs		
Wed Jun 02 15:53:18	LS: 1 SS: 2 EqIter: 1	Total PCG Iters: 38
Wed Jun 02 15:53:18	LS: 1 SS: 3 EqIter: 1	Total PCG Iters: 39
Wed Jun 02 15:53:18	LS: 1 SS: 4 EqIter: 1	Total PCG Iters: 50
Wed Jun 02 15:53:19	LS: 1 SS: 5 EqIter: 1	Total PCG Iters: 50
Wed Jun 02 15:53:19	LS: 1 SS: 6 EqIter: 1	Total PCG Iters: 50
Wed Jun 02 15:53:20	LS: 1 SS: 7 EqIter: 1	Total PCG Iters: 50
Wed Jun 02 15:53:20	LS: 1 SS: 8 EqIter: 1	Total PCG Iters: 50
Wed Jun 02 15:53:20	LS: 1 SS: 9 EqIter: 1	Total PCG Iters: 50
Wed Jun 02 15:53:21	LS: 1 SS: 10 EqIter: 1	Total PCG Iters: 50
Wed Jun 02 15:53:21	LS: 1 SS: 11 EqIter: 1	Total PCG Iters: 50
Wed Jun 02 15:53:22	LS: 1 SS: 12 EqIter: 1	Total PCG Iters: 50
Wed Jun 02 15:53:22	LS: 1 SS: 13 EqIter: 1	Total PCG Iters: 50
Wed Jun 02 15:53:22	LS: 1 SS: 14 EqIter: 1	Total PCG Iters: 50
Wed Jun 02 15:53:23	LS: 1 SS: 15 EqIter: 1	Total PCG Iters: 50
Wed Jun 02 15:53:23	LS: 1 SS: 16 EqIter: 1	Total PCG Iters: 50
Wed Jun 02 15:53:24	LS: 1 SS: 17 EqIter: 1	Total PCG Iters: 50
Wed Jun 02 15:53:24	LS: 1 SS: 18 EqIter: 1	Total PCG Iters: 50
Wed Jun 02 15:53:25	LS: 1 SS: 19 EqIter: 1	Total PCG Iters: 50
Wed Jun 02 15:53:25	LS: 1 SS: 20 EqIter: 1	Total PCG Iters: 50
Wed Jun 02 15:53:26	LS: 1 SS: 21 EqIter: 1	Total PCG Iters: 50
Wed Jun 02 15:53:26	LS: 1 SS: 22 EqIter: 1	Total PCG Iters: 50
Wed Jun 02 15:53:26	LS: 1 SS: 23 EqIter: 1	Total PCG Iters: 50
Wed Jun 02 15:53:27	LS: 1 SS: 24 EqIter: 1	Total PCG Iters: 50
Wed Jun 02 15:53:27	LS: 1 SS: 25 EqIter: 1	Total PCG Iters: 50
Wed Jun 02 15:53:28	LS: 1 SS: 26 EqIter: 1	Total PCG Iters: 50

Wed Jun 02 15:53:45	LS: 1 SS: 70 EqIter: 1	Total PCG Iters: 50
Wed Jun 02 15:53:46	LS: 1 SS: 71 EqIter: 1	Total PCG Iters: 50
Wed Jun 02 15:53:46	LS: 1 SS: 72 EqIter: 1	Total PCG Iters: 50
Wed Jun 02 15:53:47	LS: 1 SS: 73 EqIter: 1	Total PCG Iters: 50
Wed Jun 02 15:53:47	LS: 1 SS: 74 EqIter: 1	Total PCG Iters: 50
Wed Jun 02 15:53:48	LS: 1 SS: 75 EqIter: 1	Total PCG Iters: 50
Wed Jun 02 15:53:48	LS: 1 SS: 76 EqIter: 1	Total PCG Iters: 50
Wed Jun 02 15:53:48	LS: 1 SS: 77 EqIter: 1	Total PCG Iters: 50
Wed Jun 02 15:53:49	LS: 1 SS: 78 EqIter: 1	Total PCG Iters: 50
Wed Jun 02 15:53:49	LS: 1 SS: 79 EqIter: 1	Total PCG Iters: 50
Wed Jun 02 15:53:49	LS: 1 SS: 80 EqIter: 1	Total PCG Iters: 50
Wed Jun 02 15:53:50	LS: 1 SS: 81 EqIter: 1	Total PCG Iters: 46
Wed Jun 02 15:53:50	LS: 1 SS: 82 EqIter: 1	Total PCG Iters: 46

Elapsed time for the SLM 316L SS simulation by FEM

Job:SLM316LSS at:Wed Jun 01 14:07:07 2021 Number of cores used: 1 Degrees of Freedom: 15301 DOF Constraints: 401 Elements: 5000 Assembled: 5000 Implicit: 0 Nodes: 15301 Number of Load Cases: 1 TOTAL PCG SOLVER SOLUTION CP TIME = 0.34 secs TOTAL PCG SOLVER SOLUTION ELAPSED TIME = 0.17 secs		
Wed Jun 02 14:07:07	LS: 1 SS: 2 EqIter: 1	Total PCG Iters: 26
Wed Jun 02 14:07:08	LS: 1 SS: 3 EqIter: 1	Total PCG Iters: 26
Wed Jun 02 14:07:08	LS: 1 SS: 4 EqIter: 1	Total PCG Iters: 27
Wed Jun 02 14:07:09	LS: 1 SS: 5 EqIter: 1	Total PCG Iters: 27
Wed Jun 02 14:07:09	LS: 1 SS: 6 EqIter: 1	Total PCG Iters: 27
Wed Jun 02 14:07:10	LS: 1 SS: 7 EqIter: 1	Total PCG Iters: 27
Wed Jun 02 14:07:10	LS: 1 SS: 8 EqIter: 1	Total PCG Iters: 27
Wed Jun 02 14:07:11	LS: 1 SS: 9 EqIter: 1	Total PCG Iters: 27
Wed Jun 02 14:07:11	LS: 1 SS: 10 EqIter: 1	Total PCG Iters: 27
Wed Jun 02 14:07:11	LS: 1 SS: 11 EqIter: 1	Total PCG Iters: 27
Wed Jun 02 14:07:12	LS: 1 SS: 12 EqIter: 1	Total PCG Iters: 27
Wed Jun 02 14:07:12	LS: 1 SS: 13 EqIter: 1	Total PCG Iters: 27

Wed Jun 02 14:07:30	LS: 1 SS: 57 EqIter: 1	Total PCG Iters: 28
Wed Jun 02 14:07:30	LS: 1 SS: 58 EqIter: 1	Total PCG Iters: 28
Wed Jun 02 14:07:30	LS: 1 SS: 59 EqIter: 1	Total PCG Iters: 28
Wed Jun 02 14:07:31	LS: 1 SS: 60 EqIter: 1	Total PCG Iters: 28
Wed Jun 02 14:07:31	LS: 1 SS: 61 EqIter: 1	Total PCG Iters: 28
Wed Jun 02 14:07:32	LS: 1 SS: 62 EqIter: 1	Total PCG Iters: 28
Wed Jun 02 14:07:32	LS: 1 SS: 63 EqIter: 1	Total PCG Iters: 28
Wed Jun 02 14:07:32	LS: 1 SS: 64 EqIter: 1	Total PCG Iters: 28
Wed Jun 02 14:07:33	LS: 1 SS: 65 EqIter: 1	Total PCG Iters: 27

AUTOBIOGRAPHY

My name is Rigoberto Guzmán Nogales, I was born on December 7, 1988 in Jalapa Hidalgo. My parents are Domitilo Guzmán Hernández and Hortensia Iginia Nogales Jimenez. My father has had to settle down in the USA since I was 15 years old. From that age, I only have lived with my mother and my two sisters, Alejandra and Linda Marisol. Over the years, I achieved to finish high and technical school. Later, I never imagined that I studied Mechanical Engineering, and in 2007 I was introduced to the Instituto Tecnológico de Pachuca (ITP) for studying this amazing profession. Here started the most important part of my life since I didn't know if this career was the best for me, but little by little the mechanical topics attracted me so much that in 2012 I started to study the master's in Mechanical Engineering. During this time, the interest in solving scientific challenges as well as engineering problems grew up on me, and this was the key to be a researcher. Therefore, finishing the master's degree, life gives me the opportunity to work at the Instituto Tecnológico de Estudios Superiores de Monterrey (ITESM), in Monterrey city. I knew that something interesting came since I remembered that in technical school, I liked to know via google about Monterrey city. Now I believe that things we do in daily life can mean something real through time since I took the best decision, travel to Mexico Norwest. Also, I remembered that the idea of studying Aeronautics came to my mind, and this would result real after some years more. So, after two working years in the Tec de Monterrey, in 2017 it presents to me the opportunity for studying the Doctorate of Science in Aeronautics Engineering at the Universidad Autónoma de Nuevo León (UANL). Here began another incredible part of my life and meant what I am today, a Doctorate student. I am grateful for this great opportunity and for the people I met who helped me to raffle the obstacles. The challenges were more difficult, but I enjoyed each one. In 2018, I participated in an important International Materials Research Congress at Cancun city. This was my first oral presentation made in English, but it didn't result so well as I thought. I was so nervous. Now, in 2021, a publication in an open access journal was obtained. My first article after some difficulties was possible. I also joined in other important participations like the Workshop Coloquio Industria 4.0, COMEA, and I2T2. The topic of each investigation and participation I had was Additive Manufacturing. At the beginning, I didn't know anything about this new technology, but day by day the articles, thesis, and books I read fascinated me so much. Besides, in 2017 I had the opportunity to operate one of the first 3D printing metal machines in the country. In summary, this has been something of the most representative in my life, waiting that this research work can culminate satisfactorily, and new challenges and histories can be written for the future.